

https://dspace.org/

The relationship between the metal dusting mechanism and the synthesis of carbon nanofilaments using toluene and a nickel based alloy

Ramalall, Dawlall Shahil

2016

http://hdl.handle.net/10539/21729

Ramalall, Dawlall Shahil (2016) The relationship between the metal dusting mechanism and the synthesis of carbon nanofilaments using toluene and a nickel based alloy, University of Witwatersrand, Johannesburg, <http://wiredspace.wits.ac.za/handle/10539/21729>

Downloaded from a DSpace repository. https://dspace.org/

The Relationship between the Metal Dusting Mechanism and the Synthesis of Carbon Nanofilaments using Toluene and a Nickel Based Alloy

By

Dawlall Shahil Ramalall

Student Number: 310397



WITS
UNIVERSITY

Supervisor: Assoc. Prof. Shane H. Durbach

University of the Witwatersrand, June 2016

A Dissertation submitted to the Faculty of Science, University of the Witwatersrand, Johannesburg, in fulfilment of the requirements for the degree of Master of Science.

DECLARATION

I declare that this Dissertation is my own, unaided work. It is being submitted for the Degree of Master of Science at the University of the Witwatersrand, Johannesburg. It has not been submitted before for any degree or examination at any other University.



WITS
UNIVERSITY

Dawlall Shahil Ramalall

On this 20th day of June 2016

DEDICATION

To my parents & sister:

Tony, Mona & Ashvitha Ramalall

ACKNOWLEDGEMENTS

I would like to convey my sincere gratitude to my supervisor, Assoc. Prof. Shane Durbach, for his guidance, support and understanding during this project.

I would like to thank the Department of Science Technology – National Research Foundation (DST-NRF) Centre of Excellence in Strong Materials (CoE-SM) for funding me and this project.

I am grateful to the Microscopy and Microanalysis Unit (MMU), especially Prof. Alexandra Ziegler and Dr. Deran Reddy, for providing the training, the use of the microscopes and for their excellent advice and support.

Special thanks to Dr. Rudolph Erasmus for assisting with laser Raman spectroscopy measurements and providing his expertise in this topic.

A great thank you to Dr. Josias van der Merwe and his MSc student: Ms. Yonela Mgwebi, (School of Metallurgical & Chemical Engineering – University of the Witwatersrand) for their expertise in the field of Metallurgy as well as their technical assistance.

Thank you to Prof. Dave Billing and Dr. Daniel Wamwangi for the use of the XRD unit.

To Catommat for great friendship bonds that can never be broken.

Special thanks to Mr. Basil Chaussoulas for his invaluable experience in the field of chemical engineering and also for his technical assistance.

Finally and above all, I am grateful to God who has led me to complete this Master's degree and guiding my path during difficult and pleasant situations.

PRESENTATIONS

D.S. Ramalall and S.H. Durbach, *DUSTING AWAY CARBON NANOFILAMENTS: The synthesis of Carbon Nanofilaments via the Metal Dusting Mechanism on a Polished versus an Unpolished Nickel Based Alloy*, Department of Science & Technology – National Research Foundation (DST-NRF) Centre of Excellence in Strong Materials (CoE-SM) annual presentations – Johannesburg (South Africa), May 2016 (poster presentation).

D.S. Ramalall and S.H. Durbach, *Metal Dusting – A Consequence of Liquid Hydrocarbons*, Microscopy Society of South Africa (MSSA) – Pretoria (South Africa), December 2015 (poster presentation).

D.S. Ramalall and S.H. Durbach, *The Relationship between the Metal Dusting Mechanism & the Synthesis of Carbon Nanomaterials using Ni-based Alloys & Vaporised Hydrocarbons*, Department of Science & Technology – National Research Foundation (DST-NRF) Centre of Excellence in Strong Materials (CoE-SM) annual presentations – Johannesburg (South Africa), May 2015 (poster presentation).

PUBLICATIONS

1. **D.S. Ramalall** and S.H. Durbach, Metal Dusting – A Consequence of Liquid Hydrocarbons, Microscopy Society of Southern Africa 2015 *(Conference Proceedings)*, **Volume 45**, pg. 67.

TABLE OF CONTENTS

1. Introduction

1.1. General Introduction . . . . . 1 – 4

1.2. General Aim of the Project 4

1.2.1. Project Objectives . . . . . 4 – 5

1.3. Hypothesis and Research Questions 5

1.3.1. Hypothesis Question 5

1.3.2. Research Questions 5

1.4. Outline of dissertation 6

1.5. References . . . . . 7 – 8

2. Literature Review

2.1. Alloys and Hastelloys 9

2.2. Constituents of Petroleum . . . . . 9 – 11

2.3. Carbon Nanomaterials . . . . . 11 – 13

2.4. Metal Dusting . . . . . 14 – 23

2.4.1. What is Metal Dusting? . . . . . 14 – 15

2.4.2. Gas Phase Reactions in Metal Dusting . . . . . 15 – 17

2.4.3. Mechanisms of Metal Dusting . . . . . 17 – 18

2.4.3.1. Dusting of Iron . . . . . 18 – 19

2.4.3.2. Dusting of Nickel . . . . . 20 – 21

2.4.3.3. Dusting of Fe-Ni alloys . . . . . 21 – 22

2.4.4. Metal Dusting and the Effect of Surface Oxides . . . . 22 – 23

2.5. References . . . . . 24 – 25

3. Experimental & Characterisation Methods

3.1. Experimental Methods . . . . . 26 – 29

3.1.1. Hastelloy C276 . . . . . 26 – 27

3.1.1.1. Constituents of Hastelloy C276 . . . . . 26 – 27

3.1.1.2. Preparation of Hastelloy C276 27

3.1.2. Experimental Setup – Chemical Vapour Deposition (CVD) . . . . . 28 – 29
3.2. Methods of Characterisation 30
3.2.1. Optical Microscopy (OM) . . . . . 30 – 31
3.2.2. Scanning Electron Microscopy (SEM) . . . . . 31 – 33
3.2.3. Electron Probe Microanalysis (EPMA) . . . . . 33 – 35
3.2.4. Transmission Electron Microscopy (TEM) . . . . . 35 – 37
3.2.5. Powder X-ray Diffraction (PXRD) . . . . . 37 – 40
3.2.6. Laser Raman Spectroscopy . . . . . 40 – 42
3.3. References 43

4. Does metal dusting occur on Hastelloy C276 when toluene is used as hydrocarbon source?

4.1. Introduction . . . . . 44 – 45
4.2. Experimental Procedures 46
4.3. Results & Discussion . . . . . 47 – 73
4.3.1. Evidence of metal dusting (MD) on polished Hastelloy C276 blocks using toluene as a hydrocarbon source . . . . . 47 – 73
4.3.1.1. Polished untreated Hastelloy blocks exposed to gaseous helium at 800 °C . . . . . 47 – 55
4.3.1.1.1. Optical Microscopy (OM) . . . . . 47 – 48
4.3.1.1.2. Scanning Electron Microscopy (SEM) . . . . . 48 – 49
4.3.1.1.3. Electron Probe Microanalysis (EPMA) . . . . . 49 – 54
4.3.1.1.4. Powder X-ray Diffraction (PXRD) . . . . . 54 – 55
4.3.1.2. Polished Untreated Hastelloy blocks exposed to laboratory air at 800 °C . . . . . 55 – 60
4.3.1.2.1. Optical Microscopy (OM) . . . . . 55 – 56
4.3.1.2.2. Scanning Electron Microscopy (SEM) . . . . . 56 – 57

4.3.1.2.3. Electron Probe Microanalysis (EPMA) . . . . . 57 – 59
4.3.1.2.4. Powder X-ray Diffraction (PXRD) . . . 60
4.3.1.3. Polished untreated Hastelloy blocks exposed to toluene – Metal Dusting (MD) . . . . . 61 – 68
4.3.1.3.1. Optical Microscopy 61
4.3.1.3.2. Laser Raman Spectroscopy . . . . . 62 – 63
4.3.1.3.3. Scanning Electron Microscopy (SEM) 63
4.3.1.3.4. Electron Probe Microanalysis (EPMA) . . . . . 63 – 67
4.3.1.3.5. Powder X-ray Diffraction (PXRD) . . . . . 67 – 68
4.3.1.4. Removal of the carbonaceous material from Hastelloy C276 using laboratory air at 800 °C to determine the effects of metal dusting (MD) using vaporized toluene . . . . . 68 – 73
4.3.1.4.1. Optical Microscopy (OM) . . . . . 68 – 69
4.3.1.4.2. Scanning Electron Microscopy (SEM) . . . . . 69 – 70
4.3.1.4.3. Electron Probe Microanalysis (EPMA) . . . . . 70 – 73
4.3.1.4.3. Powder X-ray Diffraction (PXRD) . . . 73
4.4. Conclusions . . . . . 74 – 75
4.5. References . . . . . 76 – 77

5. Synthesis and characterisation of carbon nanofilaments via the metal dusting (MD) mechanism

5.1. Introduction . . . . . 78 – 79
5.2. Experimental Procedures . . . . . 80 – 81
5.3. Results & Discussion . . . . . 82 – 119
5.3.1. Temperature Study . . . . . 82 – 84

5.3.2. Flow rate and reaction time study . . . . . 84 – 90
5.3.3. TEM analyses of the Carbon Nanofilaments synthesized . . . . . 90 – 93
5.3.4. Reaction Kinetics . . . . . 93 – 97
5.3.5. Activation Energy (E_a) . . . . . 98 – 101
5.3.6. Powder X-ray Diffraction (PXRD) . . . . . 101 – 109
5.3.6.1. Carbon Crystallisation via MD . . . . . 108 - 109
5.3.7. Laser Raman Spectroscopy . . . . . 109 – 114
5.3.8. MD mechanism and Carbon Nanofilament Formation Relationship . . . . . 114 – 117
5.3.9. Additional Carbon Nanomaterials (CNMs) . . . . . 117 – 119
5.4. Conclusions . . . . . 120 – 122
5.5. References . . . . . 123 – 124

6. General Conclusions & Recommendations

6.2. General Conclusions . . . . . 125 – 126
6.3. Recommendations . . . . . 126 – 128

Appendices

Appendix 1 129
Appendix 2 130
Appendix 3 131
Appendix 4 132
Appendix 5 . . . . . 133 – 140
Appendix 6 141
Appendix 7 142
Appendix 8 . . . . . 143 – 145

ABSTRACT

Metal dusting (MD) is a severe type of corrosion that occurs mainly in petrochemical industries. The occurrence of MD is mainly due to syngas attacking Fe-, Ni- and Co-based alloys at elevated temperatures. More recently, literature has shown that apart from syngas, liquid hydrocarbon sources have been causing problems on platformer units in refineries. In the first part of this study a highly corrosion resistant Ni-based alloy (Hastelloy C276), in its polished form, was subjected to MD conditions at 800 °C using a liquid hydrocarbon (toluene) and helium (carrier gas) for 1 h. Exposure to these conditions revealed the formation of carbon nanofilaments and graphite layers which were confirmed by laser Raman spectroscopy, scanning electron microscopy (SEM) and electron probe microanalysis (EPMA). Burning off the carbon nanofilaments and the graphite layers in laboratory air for 1 h at 800 °C revealed that pits were formed on the Hastelloy C276. These same pits were not evident when Hastelloy C276 was exposed to either the carrier gas (helium) or laboratory air alone.

Besides MD being a continuous problem in industry, this mechanism has been shown to be beneficial in the synthesis of carbon nanofilaments viz., carbon nanofibers (CNTs) and nanotubes (CNFs). In the second part of this study, unpolished Hastelloy C276 blocks (as opposed to polished blocks) were used to synthesize carbon nanofilaments. This was done as prior studies had shown that carbon nanofilaments were produced with better quality and greater yields this way. Here the flow rate (80, 160 and 240 mL/min) and reaction duration (10, 15, 30, 45, 60, 120 and 240 min) were studied using toluene (a liquid hydrocarbon). Scanning electron microscopy (SEM) and transmission electron microscopy (TEM) were used to assess the quality and quantity of the carbon nanofilaments synthesized. Besides the formation of carbon nanofilaments, a less important material known as graphite particle structures (GPSs) were also synthesized. These studies collectively showed that MD had taken place on the surface of Hastelloy C276 when exposed to toluene at 800 °C.

LIST OF FIGURES

Figure 1.1. Examples of MD showing: **(a)** A wall segment thinned from both sides in a heat exchanger for synthesis gas **[8]**, **(b)** A heater tube of a direct reduction plant**[8]**, **(c)** A piece of steel with unusual pitting in a direct reduction furnace**[8]**, **(d)** Part of a corroded tube in a heat exchanger of an ammonia plant**[8]** and **(e)** The inner surface of a platforming unit tube **[9]**. 2

Figure 2.1. A diagram of a few nanocarbon structures **[6]**. 12
Figure 2.2. Structures representing: **(a)** Carbon which is sp^3 hybridised and **(b)** Carbon which is sp^2 hybridised **[7]**. 13
Figure 2.3. The rolling and stacking of graphene sheets for the formation of CNTs and CNFs **[12]**. 13
Figure 2.4. An example of surface pitting on a piece of steel **[25]**. 14
Figure 2.5. The processes of MD on an atomic scale **[14]**. 16
Figure 2.6. Development of Fe dusting **[27]**. 18
Figure 2.7. Five main steps in the process of MD in Fe **[26]**.. 19
Figure 2.8. Volume expansion on a Ni surface due to the growth of graphite **[27]**. 20
Figure 2.9. Four main steps of the process of MD in Ni **[26]**. 21
Figure 2.10. Processes showing the depletion of a protective oxide scale on high alloy materials (0.45 – 0.75 weight % carbon) which lead to the growth of MD pits **[14]**.. 23

Figure 3.1. CVD experimental setup. 28
Figure 3.2. Olympus BX 63 Optical Microscope. 31
Figure 3.3. A simple schematic of how SEM works **[1]**. 32
Figure 3.4. FEI Nova Nanolab 600 FEG-SEM/FIB. 33
Figure 3.5. A simplified illustration of an electron probe microanalyzer **[2]**. . . 34
Figure 3.6. CAMECA SX5-FE EPMA 35
Figure 3.7. A simple schematic of how TEM works **[7]**. 36

Figure 3.8. FEI Tecnai T12 TEM. 37
Figure 3.9. A typical setup of a diffractometer **[9]**. 38
Figure 3.10. Bruker D2 Phaser. 39
Figure 3.11. Bruker D8 Discover. 40
Figure 3.12. Motions of carbon showing the: **(a)** E_{2g} stretching mode (G) and **(b)** A_{1g} breathing mode (D) **[13]**. 41
Figure 3.13. Horiba Jobin-Yvon Raman Spectrometer (T64000). 42

Figure 4.1. OM images of a polished Hastelloy C276: **(a)** After having been heat treated at 800 °C in helium gas only and **(b)** In its unreacted form. 47
Figure 4.2. SEM micrographs showing: **(a)** The effect of temperature (800 °C) and helium gas on a polished Hastelloy C276 block, **(b)** A magnified section of (**a**) and **(c)** A polished, untreated Hastelloy C276 block. 48
Figure 4.3. Elemental Maps of a polished untreated Hastelloy C276 surface showing: **(a)** A SEM micrograph of the mapped area, **(b)** Ni K_α, **(c)** Cr K_α, **(d)** Mo L_α,**(e)** Fe K_α and **(f)** O K_α. 50
Figure 4.4. Elemental maps of the Hastelloy C276 surface that was heat treated at 800 °C in helium gas for 1 h showing: **(a)** A SEM micrograph of the mapped area, **(b)** Ni K_α, **(c)** Cr K_α, **(d)** Mo L_α,**(e)** Fe K_α and **(f)** O K_α. 51
Figure 4.5. Elemental map of the Hastelloy C276 surface that was heat treated at 800 °C in helium gas for 1 h showing: **(a)** C K_α, **(b)** C K_α which was overlaid onto Cr K_α and **(c)** A magnification of (**b**) where C K_α and Cr K_α were overlaid onto each other. 53
Figure 4.6. PXRD patterns showing Hastelloy C276: **(a)** After exposure to helium at 800 ^oC (black pattern) and **(b)** Untreated i.e. in its pristine polished form (red pattern). 54
Figure 4.7. OM image of a polished Hastelloy C276 block after having been heat treated in laboratory air at 800 °C. 56
Figure 4.8. A SEM micrograph showing the effect of laboratory air at 800 °C on a polished Hastelloy C276 block. 57
Figure 4.9. The elemental maps of the surface of a Hastelloy C276 block that was heat treated at 800 °C in laboratory air for 1 h showing: **(a)** A SEM micrograph of

the mapped area, **(b)** Ni K_α, **(c)** Cr K_α, **(d)** Mo L_α,**(e)** Fe K_α and **(f)** O K_α. 58

Figure 4.10. PXRD pattern showing Hastelloy C276: **(a)** Exposed to laboratory air at 800 °C and **(b)** Untreated (i.e. in its pristine polished form). 60

Figure 4.11. An OM image of a polished Hastelloy C276 after having been subjected to vaporized toluene and gaseous helium (80 mL/min) at 800 °C for 1 h. 61

Figure 4.12. A laser Raman spectrum of a small sample of the black soot-like products which had formed on the surface of the Hastelloy block that had been subjected to vaporized toluene and gaseous helium (80 mL/min) at 800 °C for 1 h. 62

Figure 4.13. A SEM micrograph showing the carbonaceous products formed on the surface of Hastelloy C276 due to reaction with vaporized toluene at 800 °C. 63

Figure 4.14. Elemental maps of a polished Hastelloy C276 surface exposed to the above-mentioned reaction conditions showing: **(a)** A SEM micrograph of the mapped area, **(b)** Ni K_α, **(c)** Cr K_α, **(d)** Mo L_α, **(e)** Fe K_α and **(f)** C K_α. 64

Figure 4.15. Elemental map of a polished Hastelloy C276 surface exposed to the above-mentioned reaction conditions showing the distribution of O K_α. 66

Figure 4.16. PXRD pattern showing the formation of oxides when vaporized toluene and helium gas at 80 mL/min was passed over an untreated polished Hastelloy C276 block at 800 °C. 67

Figure 4.17. An OM image of a Hastelloy C276 block which had been heat treated at 800 °C for 1 h in laboratory air after having being carburized in vaporized toluene with helium as the carrier gas at 800 °C. 69

Figure 4.18. SEM micrographs showing: **(a)** A MD pit which had formed on the surface of a polished Hastelloy C276 block due to toluene after the carbonaceous products had been burnt off, **(b)** A magnified section of (**a**). 70

Figure 4.19. Elemental maps of a carburised Hastelloy C276 surface, after the carbonaceous products had been burnt off, showing: **(a)** a SEM micrograph of the mapped area, **(b)** Ni K_α **(c)** Cr K_α, **(d)** Mo L_α, and **(e)** Fe K_α. 71

Figure 4.20. Elemental Maps of a polished Hastelloy C276 surface exposed to MD conditions after carbon had been burnt off, showing: **(a)** A SEM micrograph of the mapped area and **(b)** O K_{α}. 72
Figure 4.21. PXRD pattern showing Hastelloy C276: **(a)** Exposed to vaporised toluene and gaseous helium at 800 °C and then burnt in laboratory air at 800 °C to remove carbonaceous materials and **(b)** Untreated (i.e. in its pristine polished form). 73

Figure 5.1. SEM image of an unpolished Hastelloy C276 block which showed a pit (left hand arrow with outline) with surface roughness (right hand arrow). . . 80
Figure 5.2. SEM micrographs of carbon nanofilaments synthesized on Hastelloy C276 at: **(a)** 700 °C, **(b)** 800 °C and **(c)** 900 °C at 80 mL/min for 4 h. 82
Figure 5.3. A plot of effect of the reaction temperature on the carbon yield on Hastelloy C276 at 80 mL/min during a 240 min reaction. 83
Figure 5.4. Carbon nanofilaments synthesized at 80 mL/min with varying durations of reaction times: **(a)** 10 min, **(b)** 15 min, **(c)** 30 min, **(d)** 45 min, **(e)** 60 min, **(f)** 120 min and **(g)** 240 min. 85
Figure 5.5. Carbon nanofilaments synthesized at 160 mL/min with varying durations of reaction times: **(a)** 10 min, **(b)** 15 min, **(c)** 30 min, **(d)** 45 min, **(e)** 60 min, **(f)** 120 min and **(g)** 240 min. 86
Figure 5.6. Carbon nanofilaments synthesized at 240 mL/min with varying durations of reaction times: **(a)** 10 min, **(b)** 15 min, **(c)** 30 min, **(d)** 45 min, **(e)** 60 min, **(f)** 120 min and **(g)** 240 min. 87
Figure 5.7. A plot of the effects of flow rate and reaction duration on the average diameter of carbon nanofilaments that were synthesized at 800 °C. 90
Figure 5.8. TEM micrographs of nanofilamentous materials formed under various reaction conditions showing a: **(a)** CNF, **(b)** CNT, **(c)** CNT showing rolled graphene sheets, **(d)** CNF with a herringbone morphology, **(e)** CNF with a metal particle at its tip and **(f)** CNF with a metal particle in the middle. 91
Figure 5.9. A plot of the effect of reaction duration at various flow rates on the mass of carbon gained per area on Hastelloy C276 at 800 °C. 93

Figure 5.10. A plot of the effect of flow rate on the carburisation rate on Hastelloy C276 at 800 °C. 95
Figure 5.11. A plot of the natural logarithm of the carburisation rate versus the duration of reaction. 96
Figure 5.12. A plot of the inverse of the carburisation rate versus the duration of reaction. 97
Figure 5.13. PXRD patterns of Hastelloy C276 exposed to MD conditions at 80 mL/min of different durations of reaction. 102
Figure 5.14. PXRD patterns of Hastelloy C276 exposed to MD conditions at 160 mL/min of different durations of reaction. 102
Figure 5.15. PXRD patterns of Hastelloy C276 exposed to MD conditions at 240 mL/min at different durations of reaction. 103
Figure 5.16. The **g**razing angle XRD pattern of the surface of Hastelloy C276 exposed to MD. 105
Figure 5.17. Schematic representation of the formation of the (002) graphite plane after precipitation of carbon from a metal particle**[24]**. 106
Figure 5.18. Magnification of PXRD patterns of the nickel chromium or nickel (111) plane of Hastelloy C276 at 80 mL/min ***(from Figure 5.13)***. 107
Figure 5.19. Process of carbon crystallisation via the assistance of Ni **[6]**. . . . 108
Figure 5.20. Raman spectra representing the D and G Bands of carbon nanofilaments synthesized at 80 mL/min. 110
Figure 5.21. Raman spectra representing the D and G Bands of carbon nanofilaments synthesized at 160 mL/min. 110
Figure 5.22. Raman spectra pattern representing the D and G Bands of carbon nanofilaments synthesized at 80 mL/min. 111
Figure 5.23. P63/mmc structure of graphite **[23]**. 112
Figure 5.24. Issues which influence of the shape of the laser Raman spectra **[31]**. 113
Figure 5.25. A plot of the effect of flow rate on the I_G/I_D ratio as the duration of reaction increased. 114
Figure 5.26. VLS model showing: **(a)** Tip growth and **(b)** Root growth mechanism **[5]**. 115

Figure 5.27. SEM micrographs of: **(a)** Graphite particle structures (GPSs) on the surface of unpolished Hastelloy C276 and **(b)** The site where graphite particle structures (GPSs) were formed on Hastelloy C276. 118
Figure 5.28. OM image showing exuberant carbon deposition in the pits of Hastelloy C276. 119
Figure 5.29. Elemental map of carbon nanofilaments and agglomeration of GPSs showing: **(a)** SEM micrograph of mapped area and **(b)** C K_{α} 119

Figure 7.1. Elemental maps of a polished Hastelloy C276 surface exposed to MD conditions at higher magnification showing: **(a)** SEM image of the mapped area, **(b)** Cr K_{α} and **(c)** C K_{α}. 129
Figure 7.2. Extension of elemental maps of a polished Hastelloy C276 surface exposed to MD conditions after carbon had been burnt off from *Figure 4.13*, showing: **(a)** Ni K_{α}, **(b)** Cr K_{α}, **(c)** Mo L_{α} and **(d)** Fe K_{α}. 130
Figure 7.3. SEM image showing: **(a)** A rough Hastelloy C276 surface and **(b)** A high yield of carbon nanofilaments that formed when synthesized on a rough surface of Hastelloy C276 and exposed to reaction conditions. 131
Figure 7.4. TEM images showing carbon nanofilaments that were poorly formed. 132
Figure 7.5. TEM-EDS for metal particle between carbon nanofilaments in *Figure 5.8*. 141
Figure 7.6. PXRD patterns of Hastelloy C276 exposed to MD conditions at 80 mL/min of reaction times ranging from 10 – 240 minutes. 143
Figure 7.7. PXRD patterns of Hastelloy C276 exposed to MD conditions at 160 mL/min of reaction times ranging from 10 – 240 minutes. 144
Figure 7.8. PXRD patterns of Hastelloy C276 exposed to MD conditions at 240 mL/min of reaction times ranging from 10 – 240 minutes. 145

LIST OF TABLES

Table 2.1. Hydrocarbon Composition of Crude Oil 10
Table 2.2. Elemental Composition of Crude Oil 10

Table 3.1. Elemental Composition of Hastelloy C276 26
Table 3.2. Summary of Materials Used 27

Table 5.1. Average filament diameter at different flow rates 88
Table 5.2. The determination of E_a at different temperature ranges 100

Table 7.1. E_a at different temperature ranges (700 – 900 °C) 142

LIST OF ABBREVIATIONS

MD	Metal dusting
CNFs	Carbon nanofilaments
CNTs	Carbon nanotubes
CNMs	Carbon nanomaterials
XRF	X-ray fluorescence
CVD	Chemical vapour deposition
OM	Optical microscopy
SEM	Scanning electron microscopy
EPMA	Electron probe microanalysis
TEM	Transmission electron microscopy
XRD	X-ray diffraction
PXRD	Powder X-ray diffraction
IGA	Intergranular attack
IGC	Intergranular corrosion
E_a	Activation energy
GPSs	Graphite particle structures
h	Hours
min	Minutes
α	Alpha value
He	Helium
Ni	Nickel
Cr	Chromium
Mo	Molybdenum

Fe	Iron
Mn	Manganese
C	Carbon
O	Oxygen
W	Tungsten

1 INTRODUCTION

1.1. General Introduction

The petroleum industry, though its many refineries, is a global contributor to the supply of energy and the production of raw materials for many chemicals ranging from: carbon black to ammonia, alcohols and glycols to synthetic rubber and plastics, etc. [1]. Raw crude oil entering a refinery contains several forms of sulfur, water, salts, organics, nitrogen and organic acids which split, combine or convert into numerous corrosive combinations, which may act in different areas of the plant [2]. In particular, metal dusting (MD) is one type of corrosion that poses many challenges to the petroleum industry. For example, pit growth of stainless steels due to MD has been known to reach at least 1 mm/month, and has caused a widespread problem in cracker furnaces as well as reforming units [2, 3]. Various other chemical reactor processes which involve organic compounds, such as: hydrodealkation, butane dehydrogenation, pyridine production and acetic acid cracking have also faced the problem of MD. Besides the petroleum industry, ammonia plants, energy production plants and the heat-treating industry have also been subject to MD [2, 4].

There are different ways in which corrosion may be defined. Most commonly, corrosion is the unsatisfactory deterioration of a material due to its reaction with the environment. Corrosion reactions may be described as either ‘wet’ or ‘dry’ [3]. Wet corrosion occurs in the presence of aqueous solutions (electrolytes) e.g. galvanic corrosion, pitting corrosion, erosion corrosion, etc. Dry corrosion, on the other hand, arises when no liquid is present or the temperature is above the dew point of the environment e.g. oxidation, sulphidation, carburization, etc. Corrosion due to MD is preceded by carburization, a process whereby carbon is absorbed into a material at elevated temperatures while in contact with a carbonaceous material or carburising environment [2]; and results in accelerated localised

pitting that currently poses a challenging and costly threat to the syngas and petrochemical industry [5]. One immediate challenge is the cost associated with plant downtime when metal dusted components need to be replaced [6, 7].

In 2003, Grabke *et al*. [8] reported five cases where MD had occurred in industry, namely in:

1. A heat exchanger for synthesis gas (Figure 1.1 (a.))
2. The gas heaters of a direct reduction plant (Figure 1.1 (b.))
3. A direct reduction furnace (Figure 1.1 (c.))
4. A heat exchanger of an ammonia plant (Figure 1.1 (d.)); and
5. A refinery furnace where a platformer unit had failed (Figure 1.1 (e.)).

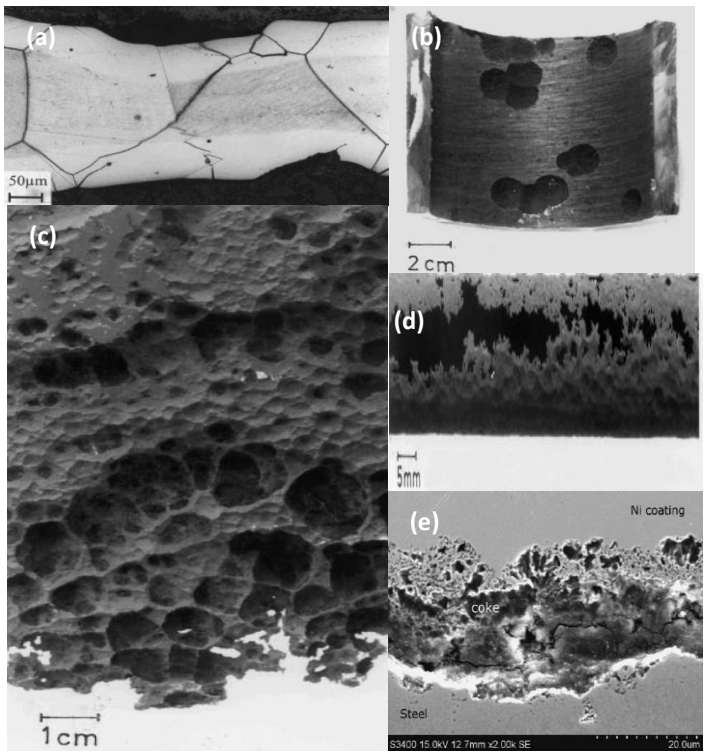


Figure 1.1. Examples of MD showing: **(a)** A wall segment thinned from both sides in a heat exchanger for synthesis gas **[8]**, **(b)** A heater tube of a direct reduction plant**[8]**, **(c)** A piece of steel with unusual pitting in a direct reduction furnace **[8]**, **(d)** Part of a corroded tube in a heat exchanger of an ammonia plant **[8]** and **(e)** The inner surface of a platforming unit tube **[9]**.

In the first four cases mentioned above, MD had occurred mainly due to the carburization of an alloy via syngas mixtures pertinent to chemicals and petrochemicals. Syngas predominantly consists of carbon monoxide, hydrogen and occasionally carbon dioxide. The fifth case, however, was not due to the occurrence of syngas, but rather due to a liquid mixture of hydrocarbons known as naphtha, which was similar to the case investigated in the research presented here.

In 2009, Dampc *et al*. [9] and more recently in 2016, Szkodo *et al.* [10] reported that the charge heater tubes within catalytic reformers, where a mixture of liquid hydrocarbons or naphtha was being reformed into alkenes or aromatics, were susceptible to MD when they were operated at high carbon activities and elevated temperatures. This served as the basis of my studies, where a liquid hydrocarbon i.e. toluene (C_7H_8) was chosen to investigate the conditions under which MD might be brought about with a selected Ni-based alloy i.e. Hastelloy C276, that was known to be highly corrosion resistant.

MD and carbonaceous material growth are two phenomena that are closely related to one another, but are usually studied independently [5, 11]. Simultaneously, where MD is a relentless problem, carbon nanomaterial formation is a potentially beneficial outcome of this type of corrosion. MD research has mainly focused on the mechanism of carburization and the protection of alloys against carburization; limited consideration has been taken into account between the interconnectedness of carbonaceous material formation and MD. However, Schmid *et al*. [12] reported that the outgrowth of carbonaceous material from a metal surface is an initial characteristic of MD. These carbonaceous materials are known collectively as carbon nanofilaments and comprise: carbon nanofibers (CNFs) and carbon nanotubes (CNTs) [5, 11].

CNTs/CNFs are allotropes of carbon. They are cylindrical in shape and possess extraordinary mechanical, electrical, thermal, optical and chemical properties that make them potentially viable in a wide variety of applications in material science and nanotechnology [13, 14]. CNTs/CNFs will be discussed further in *Sections*

2.3 and *5.1*. Besides the occurrence of MD in connection with undesirable corrosion, the synthesis of carbon nanotubes (CNTs), though enhancing the MD mechanism, has been growing vastly [15-18].

1.2. General Aim of the Project

The principal aims of this project was to: (1) Assess MD corrosion taking place on a Ni-based alloy known as Hastelloy C276 due to a liquid hydrocarbon (toluene) and (2) Assess the types and quantities of carbon nanomaterials formed due to the MD mechanism.

1.2.1. Project Objectives

The project objectives were to:

1. Utilise toluene i.e. a constituent of petroleum in its vaporised form to bring about MD.
2. Study the processes by which MD occurs with respect to Hastelloy C276 by the use of toluene.
3. Synthesize carbon nanomaterials (in particular carbon nanofilaments) as a consequence of MD on the surface of Hastelloy C276 (catalyst) using toluene as opposed to syngas.
4. Characterise these carbon nanomaterials (especially the carbon nanofilaments) formed by MD and assess the corrosion occurring on the surface of the alloys using scanning electron microscopy (SEM), transmission electron microscopy (TEM), laser Raman spectroscopy, powder X-ray diffraction (PXRD) and electron probe microanalysis (EPMA).
5. Determine the rate of formation of carbon nanomaterials (especially carbon nanofilaments) and hence the activation energy (E_a) of toluene to form these materials on Hastelloy C276.

6. Acquire the optimum temperature and flow rate at which the % carburisation and hence carbon nanofilament growth is the highest.

1.3. Hypothesis and Research Questions

1.3.1. Hypothesis Statement

An elucidation of the processes by which MD occurs on Hastelloy C276, using toluene as a carbon source, will provide a technique for the synthesis of carbon nanofilaments.

1.3.2. Research Questions

1. Does MD occur on Hastelloy C276 using a liquid hydrocarbon like toluene?
2. Will the use of toluene on Hastelloy C276 yield a variety of shaped carbon nanomaterials or just carbon nanofilaments (e.g. CNTs/CNFs) using the MD process?
3. Is the formation of these shaped carbon nanomaterials reproducible?
4. What are the optimum conditions to synthesize these carbon nanomaterials?
5. Can the activation energy (E_a) of toluene to form carbon nanofilaments by MD on Hastelloy C276 be determined?

1.4. Outline of dissertation

Chapter 1: Gives a general introduction, research hypothesis, aim and objectives of this study.

Chapter 2: Gives a descriptive review on what carbon nanomaterials (including CNTs and CNFs) are, as well as the mechanisms of MD.

Chapter 3: Provides experimental and characterization procedures used in the examination of MD corrosion and the synthesis of carbon nanofilaments by MD over Hastelloy C276.

Chapter 4: Reports on the results obtained from the effect of MD on Hastelloy C276 using toluene instead of syngas. The Hastelloy C276 samples were polished to examine the differences of the surface before and after MD experiments which were carried out at 800 °C for the purposes of Chapter 5.

Chapter 5: Reports on the synthesis and characterisation of carbon nanofilaments synthesized via the MD mechanism on Hastelloy C276 using toluene. As opposed to Chapter 4, unpolished Hastelloy C276 samples were used since they provided better growth of carbon nanofilaments as compared to a polished surface. The synthesis of carbon nanofilaments reactions were carried out at 800 °C since preliminary studies had shown the best results at this temperature.

Chapter 6: Provides conclusions of this study and recommendations for future research.

1.5. References

1. Z. Foroulis, *Corrosion and corrosion inhibition in the petroleum industry.* Materials and corrosion, 1982. **33**(3): pp. 121-131.
2. G.A. Slabbert, *The effect of carbide-forming elements on the metal dusting rate in hydrocarbon environments*, 2013, Faculty of Engineering, University of the Witwatersrand, Johannesburg.
3. G.A. Slabbert, F.M.L Mulaudzi, L.A. Cornish, M.J Papo, V. Morudu and J. Zhang, *The effect of the matrix structure on the metal dusting rate in hydrocarbon environments.* Journal of the Southern African Institute of Mining and Metallurgy, 2013. **113**(2): pp. 81-90.
4. J. Klöwer, H.J. Grabke, and E.M. Müller-Lorenz, *Metal dusting of nickel-base alloys.* Materials and corrosion, 1998. **49**(5): pp. 328-329.
5. Z. Zeng, and K. Natesan, *Relationship between the growth of carbon nanofilaments and metal dusting corrosion.* Chemistry of materials, 2005. **17**(14): pp. 3794-3801.
6. F.M.L. Mulaudzi, L.A. Cornish, G.A. Slabbert and M.J. Papo, *Metal dusting on Alloys 602CA and 800.* Journal of the Southern African Institute of Mining and Metallurgy, 2012. **112**: pp. 589-600.
7. A. Agüero, M. Gutiérrea, L. Korcakova, T. Nguyen, B. Hinnemann and S. Saadi, *Metal dusting protective coatings. a literature review.* Oxidation of metals, 2011. **76**(1-2): pp. 23-42.
8. H.J. Grabke and M. Spiegel, *Occurrence of metal dusting–referring to failure cases.* Materials and corrosion, 2003. **54**(10): pp. 799-804.
9. J. Dampc, Z. Grzesik, and J. Hucińska, *Metal dusting in CCR platforming unit.* Materials and corrosion, 2009. **60**(3): pp. 211-217.
10. M. Szkodo and G. Gajowiec, *Studies of the mechanism of metal dusting of 10CrMo9-10 steel after 10 years of operation in the semi-regenerative catalytic reformer.* Corrosion Science, 2016. **102**: pp. 279-290.
11. Z. Zeng and K. Natesan, *Relationship of carbon crystallization to the metal-dusting mechanism of nickel.* Chemistry of materials, 2003. **15**(4): pp. 872-878.
12. B. Schmid, Ø. Grong, and R. Ødegård, *Coke formation in metal dusting experiments.* Materials and corrosion, 1999. **50**(11): pp. 647-653.
13. *What are carbon nanotubes?* 2014 [cited 2016 23 February]; Available from: http://www.nanocomptech.com/what-are-carbon-nanotubes.
14. *Carbon nanotubes*. 2015 [cited 2016 23 February]; Available from: https://www.sciencedaily.com/terms/carbon_nanotube.htm.
15. J.K. Chang, H.Y. Tsai, and W.T. Tsai, *Effects of post-treatments on microstructure and hydrogen storage performance of the carbon nano-tubes prepared via a metal dusting process.* Journal of Power Sources, 2008. **182**(1): pp. 317-322.
16. H. Ghorbani, A. Rashidi, S. Rastegari, S. Mirdamadi and M. Alaei, *Mass production of multi-wall carbon nanotubes by metal dusting process with high yield.* Materials Research Bulletin, 2011. **46**(5): pp. 716-721.
17. M. Hashempour, A. Vicenzo, F. Zhao and M. Bestetti, *Direct growth of MWCNTs on 316 stainless steel by chemical vapor deposition: Effect of surface nano-features on CNT growth and structure.* Carbon, 2013. **63**: pp. 330-347.

18. S.W. Pattinson, B. Viswanath, D.N. Zakharov, J. Li, E.A. Stach and A.J. Hart, *Mechanism and Enhanced Yield of Carbon Nanotube Growth on Stainless Steel by Oxygen-Induced Surface Reconstruction.* Chemistry of materials, 2015. **27**(3): pp. 932-937.

2 LITERATURE REVIEW

2.1. Alloys and Hastelloys

Alloys are metals made by combining two or more metallic elements with a small, but significant percentage of specific non-metals to give greater strength and resistance to corrosion [1].

The term ‘Hastelloy’ on the other hand is a registered trademark name of Haynes International, Inc [2]. The prefix ‘Hastel’ is utilised for a range of different highly corrosion resistant metal alloys which are generally categorised as ‘superalloys’ or ‘high performance alloys’. The principal element constituent of most Hastelloys is nickel [2, 3]. Other constituents include: molybdenum, chromium, iron, cobalt, manganese, copper, aluminium, titanium, zirconium, tungsten and carbon in varying percentages [2]. High temperatures and stress in corrosive environments are the fundamental uses of these Hastelloys, where more universal and less expensive iron-based alloys would deteriorate more easily [2]. The Hastelloy that was used in this project, amongst different variants, was Hastelloy C276 which was composed of nickel, chromium, molybdenum, iron, tungsten, cobalt, manganese, silicon and carbon [3].

2.2. Constituents of Petroleum

Petroleum is a combination of various different hydrocarbons including: alkanes, cycloalkanes and aromatics (Table 2.1) [4].

Table 2.1. Hydrocarbon Composition of Crude Oil [4].

Hydrocarbon Type	Percentage (%)
Alkanes	15-60
Cycloalkanes	30-60
Aromatics	3-30

Alkanes (linear/branched), cycloalkanes, aromatic hydrocarbons and asphaltenes (large molecules consisting primarily of carbon and hydrogen with 1 to 3 nitrogen, sulphur or oxygen atoms per molecule) are the most common hydrocarbons found in crude oil (Table 2.2), where each petroleum diversification has an exclusive mix of molecules that are characterised according to their geological origin (Table 2.2) [4].

Table 2.2. Elemental Composition of Crude Oil [4].

Element	Percentage (%)
Carbon	93-97
Hydrogen	10-14
Nitrogen	0.1-2
Oxygen	0.1-1.5
Sulphur	0.5-6

The alkanes (paraffins) are saturated hydrocarbons and have the general formula C_nH_{2n+2}. In terms of petroleum, the alkanes generally consist of 5 to 40 carbon atoms per molecule with the exception of very small quantities of either shorter or longer molecules that are also found therein [4].

Petrol is refined from alkanes consisting of pentane (C_5H_{12}) to octane (C_8H_{18}), whereas diesel fuel and kerosene are refined from nonane (C_9H_{20}) to hexadecane ($C_{16}H_{34}$) [4]. Alkanes greater than hexadecane are refined into fuel oil and

lubricating paraffin wax (approximately 25 carbons) and asphalt (≥35 carbons)[4]. Cycloalkanes (naphathenes) on the other hand are also saturated hydrocarbons and have the formula (C_nH_{2n}) which have similar properties to alkanes, but have higher boiling points [4, 5]. Aromatic hydrocarbons are unsaturated hydrocarbons and are generally found in petroleum as benzene rings (C_6H_6) which include variations of benzene such as toluene, ethyl-benzene, xylene, etc. [4, 5].

2.3. Carbon Nanomaterials

The effect of carburisation and hence MD on alloys at high temperatures with exposure to hydrocarbons has potential for the synthesis of nanocarbons. The term nanocarbon is becoming an increasingly common one, which is used to illustrate the broad range of carbon materials that have specific nano-scale dimensions and functional properties [6]. Nanocarbon structures include: single-walled carbon nanotubes (SWCNTs), multi-walled carbon nanotubes (MWCNTs), fullerenes, graphene, nano-cones, nano-diamonds, etc. (Figure 2.1) [6, 7]. Each specific shape of carbon nanomaterials has its own specific properties and hence applications [7]. Nanocarbons possess electrical and thermal conductivity, as well as mechanical strength and lightness that conventional materials cannot contest, hence the field of applications of nanocarbon materials is vast, going from photonics and optoelectronics to biotech and nano-medicine, including advanced electrodes and polymer composites [6, 8-11].

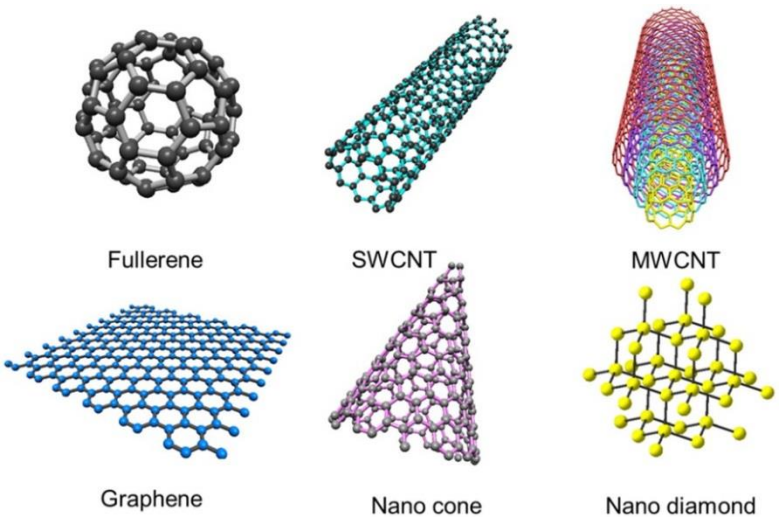


Figure 2.1. A diagram of a few nanocarbon structures **[6]**.

2.3.1. CNFs and CNTs

According to valence theory, carbon contains four valence electrons that are used to form four bonds with other atoms including itself. The occurrence of single bonds between carbon atoms (i.e. C-C) yield diamond-like structures though sp^3 hybridisation as shown in Figure 2.2. (a) [7]. The formation of double bonds between carbon atoms (i.e. C=C) gives rise to structures known as graphene structures though sp^2 hybridisation (Figure 2.2. (b)) [7]. Graphene sheets can be rolled or stacked into a variety of shapes known as carbon nanomaterials such as: CNTs, CNFs, carbon spheres (CSs) and fullerenes [12, 13].

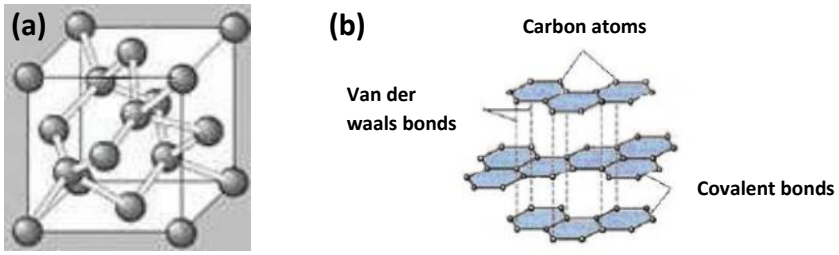


Figure 2.2. Structures representing: **(a)** Carbon which is sp^3 hybridised and **(b)** Carbon which is sp^2 hybridised **[7]**.

More specifically, in the case of CNTs, graphene sheets are rolled up in a cylindrical formation in a distinct axis to form single, double or multi-walled nanotubes depending on the number of graphene sheets that are rolled up[12, 13] as shown in Figure 2.3. In the case of CNFs, graphene sheets are stacked upon each other to form plate-like, herringbone or tubular structures [12, 13].

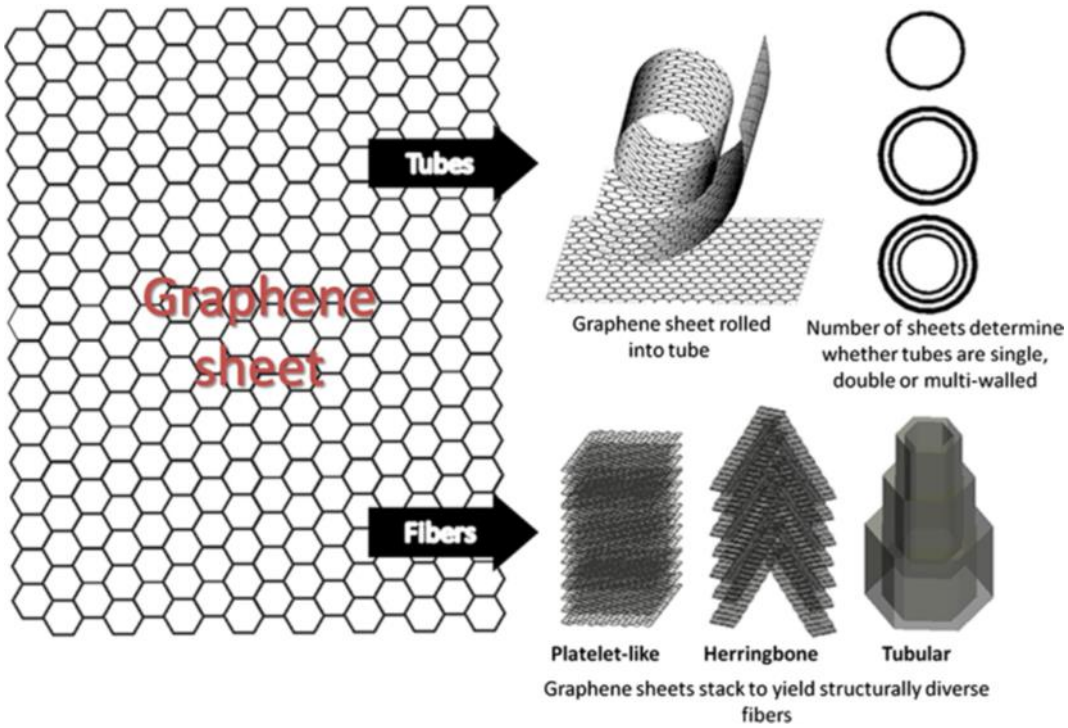


Figure 2.3. The rolling and stacking of graphene sheets for the formation of CNTs and CNFs **[12]**.

2.4. Metal Dusting (MD)

2.4.1. What is Metal Dusting?

Metal dusting (MD) is a phenomenon whereby severe corrosion of metal alloys containing Fe, Ni and Co takes place in highly reducing and carburising gas environments [14]. The process of MD occurs at temperatures between 400 °C and 900 °C according to different authors with research conducted on various alloys [14-23]. MD is preceded by carburization, a process whereby a metal alloy absorbs carbonaceous gas in a heat treatment process from a carbon containing material [24]. The surface of the metal alloy then disintegrates into smaller corrosion particles (carbon and metallic constituents of the alloy) if the activity of the carbon is more than one in a strongly carburizing atmosphere [16, 18]. These smaller loose corrosion particles can then be easily removed by flowing gas atmospheres, leaving pits on the surface of the metal alloy (Figure. 2.4).

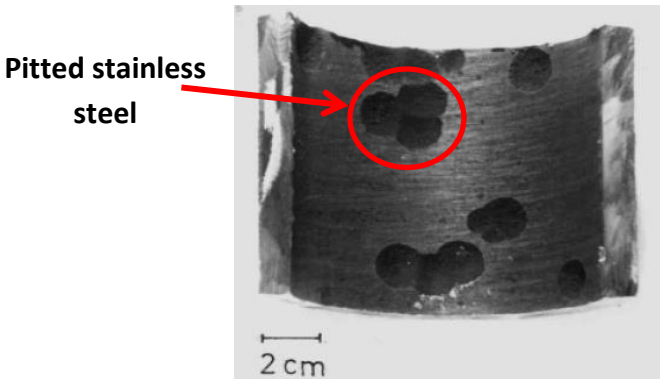


Figure 2.4. An example of surface pitting on a piece of steel **[25]**.

In order for carburisation to take place, thee fundamental principles must be present [24]:

1. A susceptible material
2. A carburising environment
3. Diffusion of carbon into the material at one of the temperatures in the range previously specified.

2.4.2. Gas-Phase Reactions in MD

As previously stated, MD only takes place when the gaseous atmosphere in proximity to the metal alloy is supersaturated with respect to carbon i.e. $a_c > 1$. In these cases carbon can be produced by thee common gas-phase reactions [14, 15, 24, 26, 27]:

Synthesis Gas Reaction: $CO + H_2 \rightleftharpoons H_2O + C$ (1)

The Boudouard Reaction: $2CO \rightleftharpoons C + CO_2$ (2)

Hydrocarbon Cracking: $CH_4 \rightleftharpoons C + 2H_2$ (3)

Carbon deposition can also be understood on an atomic level, which is facilitated by electron-orbital interactions between the active metal or metal alloy (depending on its composition) and the carbon containing species [14]. For example, in carbon monoxide (CO) a ‘push-pull’ interaction may be employed (Figure 2.5) [14].

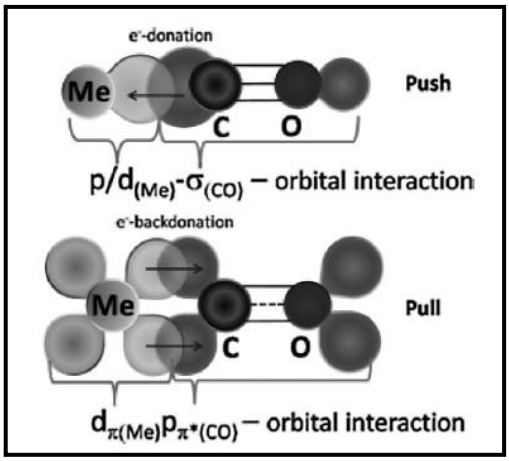


Figure 2.5. The processes of MD on an atomic scale**[14]**.

Here the filled σ-molecular orbital of the CO, located at the C-atom, pushes electron density towards the empty p or d orbital of the active metal or metal alloy which reaches a higher state of electron density [14]. The partially-filled dπ orbitals are able to redirect electron density to anti-bonding pπ orbital of the carbon monoxide molecule [14]. Due to this interaction, the C-O triple bond distance is increased and the bond strength is reduced causing the dissociation energy to be reduced [14]. This results in both carbon and oxygen being adsorbed onto the surface of the metal or metal alloy (equation 4).

$$CO \rightleftharpoons C_{ads} + O_{ads} \qquad (4)$$

Later on the adsorbed oxygen, when in the presence of hydrogen, can be removed from the metal or metal alloy's surface (represented by M) by the formation water (equation 5).

$$CO + H_2 + (M) \rightleftharpoons C(M) + H_2O \qquad (5)$$

As previously shown, depending on the alloy composition, MD reactions may either result in the formation of surface metal carbides or not [14]. Two common metal alloys associated with such MD reactions are iron and nickel based alloys:

1. Iron-based alloys

During carburisation of an iron-based alloy, supersaturation of a solid solution on its surface occurs resulting in the precipitation of cementite (Fe_3C) or iron carbide [14-16, 18, 28-31]. Cementite is stabilised in ferritic alloys by high carbon activity (equation 6) [14-16, 18, 29, 31]:

$$C + 3Fe \rightleftharpoons Fe_3C \quad (6)$$

In such cases as soon as cementite covers the metallic surface then graphite deposits on the cementite layer [14].

2. Nickel-based alloys

During carburisation of nickel alloys, due to the instability of the nickel carbide, graphitic carbon forms immediately (equation 7) [14, 18, 31, 32]:

$$C + Ni \rightleftharpoons C(gr) + Ni \quad (7)$$

Of direct interest, in this study, the solid-gas interaction for both iron and nickel-based alloys, the Ni or Fe catalyses the formation of carbon nanomaterials.

2.4.3. Mechanisms of MD

The exact mechanism of MD is still not well understood, but several models have been proposed [14, 26]. The following reaction steps have been suggested by the most common theory for MD on Fe-based alloys [14, 26]:

1. Rapid transfer of carbonaceous gas onto the iron, followed by the growth of a surface cementite layer which is suggested to be an obstacle for further carbon transfer.

2. Graphite nucleation and deposition (which is suggested to lower the carbon activity when a Fe_3C/graphite interface is formed).
3. Precipitation of iron particles into the interface layer, where they are believed to act as catalysts for further graphite deposition.

In the case of Ni-based alloys, a similar mechanism is proposed but without the formation of the intermediate Fe_3C as described previously [14, 18, 31]. Here, nickel atoms are believed to diffuse via graphite intercalation and hence catalyse further carbon deposition [14].

2.4.3.1. Dusting of Iron

As mentioned previously, cementite (Fe_3C) grows on the surface of iron-based alloys during carburization. The thickness (X) of the Fe_3C in which the inward diffusion of carbon takes place, pushing though the cementite scale, is shown in Figure 2.6 [27].

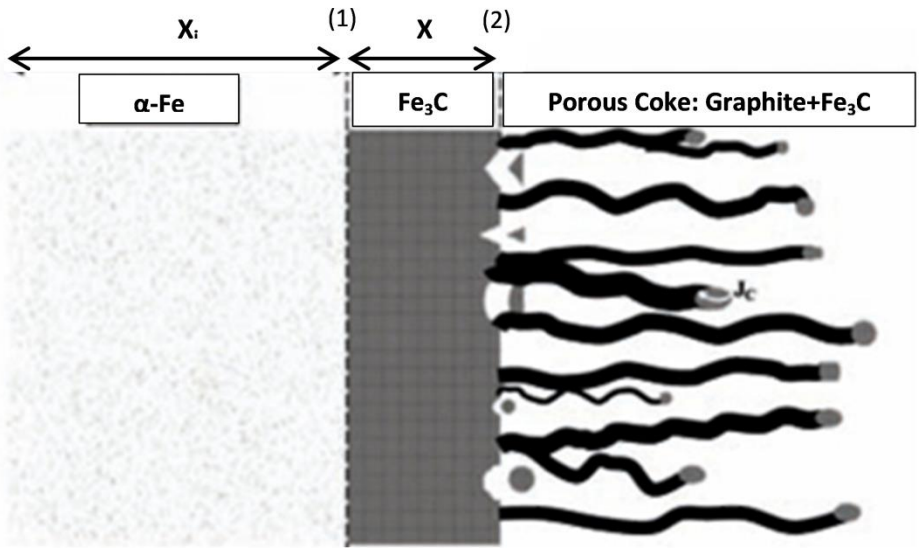


Figure 2.6. Development of Fe dusting **[27]**.

Here, the rate at which carbon diffuses is controlled by the cementite layer [27, 29]. This is followed by an increase in the mass of carbon in the form of porous coke, which settles above the Fe_3C layer [23, 27]. This coke deposit is mostly composed of graphitic nanofilaments (i.e. carbon nanotubes or nanofibers) which have Fe_3C nanoparticles at their tips [27, 28]. These nanoparticles arise when the outer surface layers of Fe_3C disintegrate, forming exposed facets onto which the graphite nanofilaments elongate leaving the nanoparticles to come off the metal surface making what is known as 'the dust' [27, 29, 33, 34]. These cementite nanoparticles are generally found in the (001) planes of iron and are conformed parallel to the attached carbon nanotube axis [14]. The growth of the graphitic coke is then sustained by the continued diffusion of carbonaceous gas though the Fe_3C layer [27].

Ideally, there are five main steps in the process of MD and the growth of carbon nanofilaments in terms of iron, which are represented schematically in Figure 2.7 [26]:

1. Deposition of carbon on the surface of iron
2. Dissolution of carbon in iron and the formation of Fe_3C (nanoparticles), where many defects are created
3. Diffusion of carbon though Fe_3C which precipitates at defects
4. Penetration of gas into cracked areas and deposition of carbon
5. Continuous carbon precipitation under Fe_3C particles which grow into carbon nanofilaments.

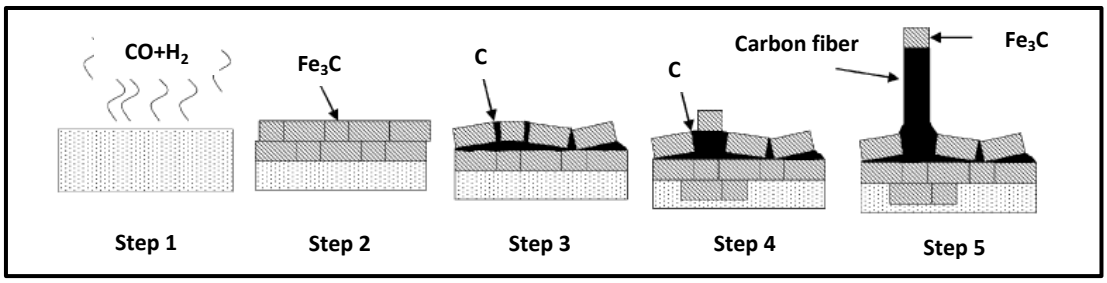


Figure 2.7. Five main steps in the process of MD in Fe **[26]**.

2.4.3.2. Dusting of Nickel

MD of nickel differs from that of iron in that cementite is not formed, as the corresponding carbide of nickel (i.e. nickel carbide) is unstable [14]. In comparison with the dusting of iron, the dusting rate of nickel is much slower. For nickel dusting, carbon deposits directly onto the metal and grows into it. The favoured contact location of the metal-graphite interface is at the $(001)_{graphite}//(111)_{Ni}$ crystallographic planes [14, 27]. Young *et al*. [14] have reported in their study of Ni dusting that little or no carbon deposition occurred on the nickel (001) plane, complete coverage occurred on the nickel (111) plane and restricted deposition occurred on nickel (101) plane; these corresponded to: slow, fast and intermediate deposition rates respectively. Graphite nucleation within the carbon supersaturated metal is due to the advancement of the energetically favoured interface. Hence volume expansion of the metal is due to the growth of graphite into is interior (Figure 2.8), where the bottom layer of graphite planes are affiliated directly with the nickel (111) plane [27]. The disruption of the metal structure is caused by graphite growing parallel to the nickel (111) plane. This disruption causes disintegration of the metal, which creates nickel nanoparticles i.e. 'the dust'. Exposure to the carbonaceous gas source then causes these nickel nanoparticles to be released. These deposit carbon at the specified crystallographic sites, to grow nanofilaments of carbon. Of significance here is that where no notable graphite is deposited i.e. at the nickel (001) planes, no disintegration or 'dust' is formed.

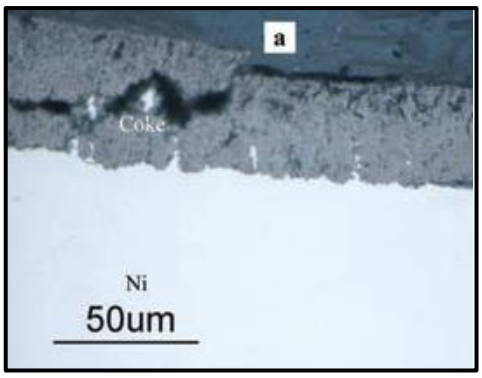


Figure 2.8. Volume expansion on a Ni surface due to the growth of graphite**[27]**.

A progressive supply of carbon by diffusion via the nickel substrate allows for the continued growth of graphite in the metal [14, 31, 35]. The products of the dusting reaction are a two-phase mixture of nickel and graphite [14, 31, 35]. At uniform nickel and high carbon activities, the carbonaceous gas is considered to be permeable in the two-phase reaction product [14, 22]. Due to the increasing quantity of graphite, the nickel particles are then displaced outwards instead of being transported by diffusion.

Similar to the 5-step MD process and the carbon nanofilament formation for iron, nickel has a 4-step process (Figure 2.9) [26]:

1. Deposition of carbon on the surface of nickel
2. Dissolution of carbon and diffusion though nickel which precipitates at the defects
3. Penetration of carbonaceous gas into cracked areas and deposition of carbon
4. Continuous carbon precipitation under nickel particles which grow into carbon nanofilaments.

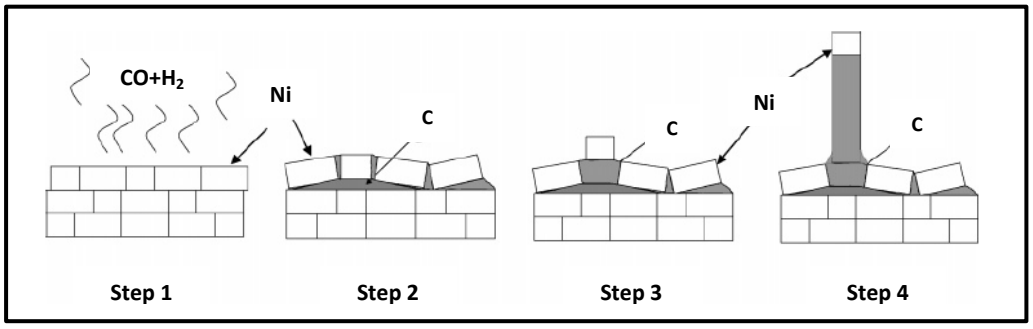


Figure 2.9. Four main steps of the process of MD in Ni **[26]**.

2.4.3.3. Dusting of Fe-Ni alloys

Different mechanisms are followed for the MD and carbon nanofilament for iron and nickel alloys despite the fact that they both involve [14]:

1. Adsorption of carbonaceous gas
2. Dissolution of carbon
3. Supersaturation of the near surface metal

One of the fundamental differences, as previously mentioned, is that pure iron forms cementite, whereas nickel does not. Although pure nickel does not form a cementite-like phase, low nickel content alloys e.g. Fe-5Ni and Fe-10Ni do have the tendency to form cementite due to the presence of iron [14]. It has however been observed that when the nickel content of the alloy is 20% or more by weight, no cementite was formed unless the carbon content of the alloy was above 0.4% [14, 34]. It was suggested that the formation of $(Fe,Ni)_3C$ was not thermodynamically hampered due to the high nickel content, but by the slow effect of carburisation on these alloys; hence the nickel dusting mechanism was more highly favoured [14] .

2.4.4. MD and the Effect of Surface Oxides

MD to some extent is prevented by an oxide scale due to the presence of oxides, especially Cr_2O_3 and Al_2O_3 [14, 24, 34], act as a diffusion obstruction against carbon access owing to the negligible solubility of carbon in these metal oxides [14, 24, 34]. Nevertheless, the infiltration of carbon can develop at physical defects in the oxide scale. In addition, the weakening of this scale may be initiated at the beginning by the incorporation of graphite into the oxide [14, 24]. Consumption of the protective oxide scale composing elements by internal corrosion processes and re-healing of damaged protective scales has been shown to weaken the capability of the alloy to preserve this protective scale[14, 24]. The process whereby a protective oxide scale can be depleted, leading to the growth of a metal dust pit is shown in Figure 2.10 [14, 24]. This process is represented by four stages:

1. An intact oxide scale on the surface of the alloy
2. This scale undergoes intrinsic oxide growth stresses (e.g. internal corrosion or damage) which leads to the formation of cracks
3. Graphite precipitates in these cracks, widening them, causing further cracking
4. Pits form as a consequence of the local scale cracking processes by graphite formation

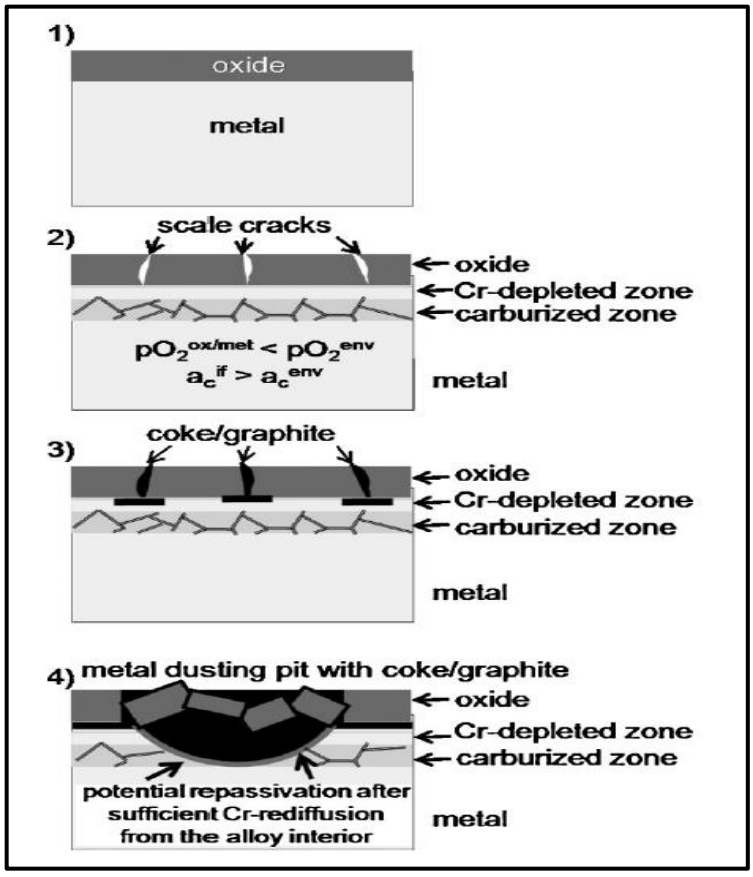


Figure 2.10. Processes showing the depletion of a protective oxide scale on high alloy materials (0.45 – 0.75 weight % carbon) which lead to the growth of MD pits **[14]**.

2.5. References

1. *Dictionary.com*. 2016 [cited 2016 7 April]; Available from: http://www.dictionary.com/browse/alloy.
2. *Corrosion-Resistant Alloys*. [cited 2014 22 April]; Available from: http://www.haynesintl.com/CRAlloys.htm.
3. *HASTELLOY® C-276 alloy Information**. 2001 [cited 2016 8 March]; Available from: http://www.haynesintl.com/HASTELLOYC276Alloy/HASTELLOYC276AlloyPF.htm.
4. *petroleum.co.uk*. [cited 2014 22 April]; Available from: http://www.petroleum.co.uk/.
5. T.L. Brown, *Chemistry: the central science*2009: Pearson Education.
6. D.S. Su, S. Perathoner, and G. Centi, *Nanocarbons for the development of advanced catalysts.* Chemical reviews, 2013. **113**(8): pp. 5782-5816.
7. N.J. Coville, S.D. Mhlanga, E.N. Nxumalo and A. Shaikjee, *A review of shaped carbon nanomaterials.* South African Journal of Science, 2011. **107**(3-4): pp. 01-15.
8. M. Endo, T. Hayashi, Y.A. Kim, M. Terrones and M.S. Dresselhaus, *Applications of carbon nanotubes in the twenty–first century.* Philosophical Transactions of the Royal Society of London A: Mathematical, Physical and Engineering Sciences, 2004. **362**(1823): pp. 2223-2238.
9. J.K. Chang, H.Y. Tsai, and W.T. Tsai, *Effects of post-treatments on microstructure and hydrogen storage performance of the carbon nano-tubes prepared via a metal dusting process.* Journal of Power Sources, 2008. **182**(1): pp. 317-322.
10. F. D'Souza and O. Ito, *Photosensitized electron transfer processes of nanocarbons applicable to solar cells.* Chemical Society Reviews, 2012. **41**(1): pp. 86-96.
11. A. Rahman, I. Ali, S.M Al Zahani and R.H. Eleithy, *A review of the applications of nanocarbon polymer composites.* Nano, 2011. **6**(03): pp. 185-203.
12. A. Shaikjee and N.J. Coville, *The synthesis, properties and uses of carbon materials with helical morphology.* Journal of Advanced Research, 2012. **3**(3): pp. 195-223.
13. A. Shaikjee and N.J. Coville, *The role of the hydrocarbon source on the growth of carbon materials.* Carbon, 2012. **50**(10): p. 3376-3398.
14. D.J. Young, J. Zhang, C. Geers and M.Schütze, *Recent advances in understanding metal dusting: A review.* Materials and corrosion, 2011. **62**(1): pp. 7-28.
15. H.J. Grabke, *Thermodynamics, mechanisms and kinetics of metal dusting.* Materials and corrosion, 1998. **49**(5): pp. 303-308.
16. H.J. Grabke, R. Krajak, and J.N. Paz, *On the mechanism of catastrophic carburization:'metal dusting'.* Corrosion Science, 1993. **35**(5): pp. 1141-1150.
17. C.Y. Lin, and W.T. Tsai, *Nano-sized carbon filament formation during metal dusting of stainless steel.* Materials chemistry and physics, 2003. **82**(3): pp. 929-936.
18. J.N. Paz and H.J. Grabke, *Metal dusting.* Oxidation of metals, 1993. **39**(5-6): pp. 437-456.
19. B. Schmid, Ø. Grong, and R. Ødegård, *Coke formation in metal dusting experiments.* Materials and corrosion, 1999. **50**(11): pp. 647-653.

20. G.A. Slabbert, F.M.L. Mulaudzi, L.A, Cornish, M.J. Papo, V. Morudu and J. ZHang, *The effect of the matrix structure on the metal dusting rate in hydrocarbon environments.* Journal of the Southern African Institute of Mining and Metallurgy, 2013. **113**(2): pp. 81-90.
21. S. Strauss and H.J. Grabke, *Role of alloying elements in steels on metal dusting.* Materials and corrosion, 1998. **49**(5): pp. 321-327.
22. Z. Zeng and K. Natesan, *Relationship of carbon crystallization to the metal-dusting mechanism of nickel.* Chemistry of materials, 2003. **15**(4): pp. 872-878.
23. J. Zhang, D. Cole, and D. Young, *Alloying with copper to reduce metal dusting of nickel.* Materials and corrosion, 2005. **56**(11): pp. 756-764.
24. G.A. Slabbert, *The effect of carbide-forming elements on the metal dusting rate in hydrocarbon environments*, 2013, Faculty of Engineering, University of the Witwatersrand, Johannesburg.
25. H.J. Grabke and M. Spiegel, *Occurrence of metal dusting–referring to failure cases.* Materials and corrosion, 2003. **54**(10): pp. 799-804.
26. Z. Zeng and K. Natesan, *Relationship between the growth of carbon nanofilaments and metal dusting corrosion.* Chemistry of materials, 2005. **17**(14): pp. 3794-3801.
27. D.J. Young and J. Zhang, *Carbon corrosion of alloys at high temperature.* Journal of the Southern African Institute of Mining and Metallurgy, 2013. **113**(2): pp. 149-154.
28. C. Toh, P. Munroe, and D. Young, *Metal dusting of Fe–Cr and Fe–Ni–Cr alloys under cyclic conditions.* Oxidation of Metals, 2002. **58**(1-2): pp. 1-21.
29. J. Zhang, A. Schneider, and G. Inden, *Initiation and growth of iron metal dusting in CO–H 2–H 2 O gas mixtures.* Corrosion science, 2008. **50**(4): pp. 1020-1034.
30. E. Müller-Lorenz and H.J. Grabke, *Coking by metal dusting of steels.* Materials and Corrosion, 1999. **50**(11): pp. 614-621.
31. H.J. Grabke, *Nickel-based alloys in carbonaceous gases.* Corrosion, 2000. **56**(8): pp. 801-808.
32. P.Szakálos , *Mechanisms of metal dusting,* Department of Material Science and Engineering, Swedish Institute for Metals Research, Stockholm, 2004.
33. J. Zhang and D.J. Young, *Kinetics and mechanisms of nickel metal dusting I. Kinetics and morphology.* Corrosion Science, 2007. **49**(3): pp. 1496-1512.
34. D.J. Young and J. Zhang, *Metal dusting: Catastrophic corrosion by carbon.* JOM, 2012. **64**(12): pp. 1461-1469.
35. H.J. Grabke, *Corrosion by carbonaceous gases, carburization and metal dusting, and methods of prevention.* Materials at high temperatures, 2000. **17**(4): pp. 483-487.

3 EXPERIMENTAL & CHARACTERISATION METHODS

3.1. Experimental Methods

3.1.1. Hastelloy C276

3.1.1.1. Constituents of Hastelloy C276

Hastelloys are Ni-based alloys which include other elements as described in Chapter 2. Amongst these elements: chromium, molybdenum, iron and tungsten constitute the alloy trademarked as Hastelloy C276. The percentages of each of these elements are shown in Table 3.1, which were analysed via X-ray fluorescence (XRF) spectroscopy by the suppliers.

Table 3.1. Elemental Composition of Hastelloy C276

Elemental (%)	Cr	Mo	Fe	W	Ni
Hastelloy C276	16.1	15.2	5.4	3.9	58.3

The materials in conjunction with their suppliers and their impurities used in the following sections are summarised in Table 3.2.

Table 3.2. Summary of Materials Used

Material	Supplier	Purity & Impurities (as per supplier specifications)
Hastelloy C276	Haynes International, Inc. (via Mintek)	*See* Table 3.1
Acetone	Associated Chemical Enterprises (ACE)	Gold Line (CP): Assay (GC) 99% Acidity 0.002% Residue on evaporation 0.0001%
Toluene	Merck	Purity (GC) ≥ 99.9% Evaporation Residue ≤ 2 mg/l Water ≤ 0.05% Acidity ≤ 0.0002 meq/g Alkalinity ≤ 0.0006 meq/g
Helium	AFROX	Baseline 5.0: Purity > 99.999% Moisture ≤ 3 ppm Oxygen ≤ 2 ppm Nitrogen ≤ 5 ppm THC as CH_4 ≤ 0.5 ppm

3.1.1.2 Preparation of Hastelloy C276

Hastelloy C276 was cut into 9 x 9 x 1.5 mm blocks using a manually operated guillotine. These Hastelloy blocks were washed using acetone to remove any dust and dirt that may have accumulated on their surface, before being subjected to any chemical reactions. Once the Hastelloy blocks were washed, they were further manipulated with tweezers to prevent contamination.

3.1.2. Experimental Setup – Chemical Vapour Deposition (CVD)

A CVD system was employed to perform investigations regarding metal dusting (MD) and the synthesis of carbon nanomaterials (CNMs). An elaborate diagram representing the CVD setup is shown in Figure 3.1.

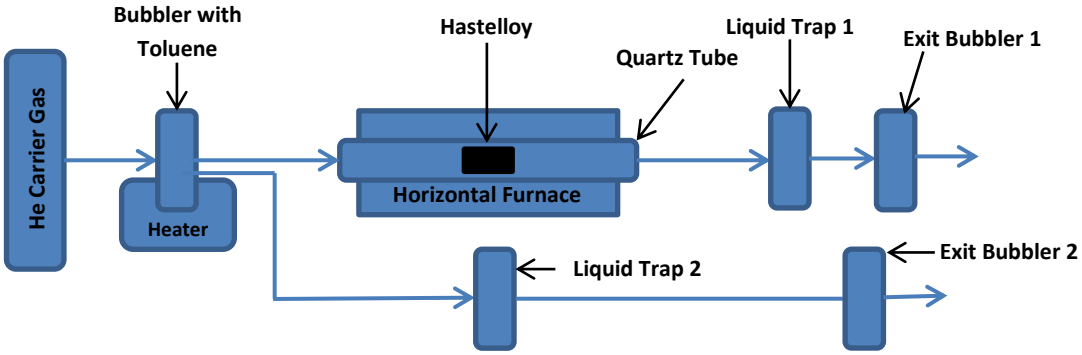


Figure 3.1. CVD experimental setup.

A single, weighed Hastelloy C276 block was placed into the mid-point of a quartz tube for each experimental run. This was then placed into a horizontal temperature controlled furnace. A bubbler containing toluene was connected to the inlet of the quartz tube which provided toluene that flowed over the Hastelloy. The toluene within the bubbler was heated with the aid of a paraffin oil-bath to 65±3 °C, for increased vaporisation, for the duration of the reaction concerned. Liquid trap 1 (as shown in Figure 3.1) was used to trap any toluene whilst being heated to ± 65 °C to relieve vapour pressure within the bubbler. This bubbler contained a by-pass mechanism which was used until the furnace reached the exact reaction temperature, which was varied between 700-900 °C for the different studies. A thermocouple was placed in the central zone of the furnace in conjunction with the Hastelloy to ensure constant temperature. The furnace was heated at a rate of 10 °C/min. Once the reaction temperature had been obtained, the by-pass was

switched over to the quartz tube so that the vaporised toluene could be supplied for the reaction to occur. Liquid trap 2 (as shown in Figure 3.1) was used to trap toluene that had not reacted with the Hastelloy. Each of the liquid traps was immersed in liquid nitrogen throughout the by-pass and reaction stages to allow for the efficient trapping of unreacted toluene.

Two exit bubblers (labelled bubbler 1 and 2 in Figure 3.1), which contained paraffin oil were connected to the outlet of the liquid traps 1 and 2. The purpose of this was to monitor the flow of helium and toluene vapour though the system. An exhaust outlet to the atmosphere was employed for both exit bubbler systems.

Gaseous helium was used as the carrier gas for the toluene, as well as to purge the system due to its inertness. The system was purged between 60-90 min before each reaction was initiated at a specified temperature. The flow rate of the helium carrier gas was varied between 80-240 mL/min for individual experimental runs, for purposes of a flow rate study. After the reaction was run at a specific temperature, duration and flow rate, the bubbler containing toluene was switched to by-pass mode, terminating the toluene feed. Thereafter, the furnace was allowed to cool to room temperature with the inert environment of helium at the specific flow rate of the experimental study. The purpose of cooling the furnace with the flow of helium gas was to ensure that the carbonaceous material which may have formed did not burn off. All experimental studies were repeated (at least in triplicate) to ensure consistency in the experimental results.

3.2. Methods of Characterisation

Diverse methods of characterisation were used to assess the effect of corrosion and the synthesis of CNMs which had occurred due to the MD phenomena. The most initial and apparent was noting the masses of the Hastelloy blocks before and after exposure to CVD conditions in order to determine the mass changes once products had been formed. Thereafter, they were characterised by: optical microscopy (OM), scanning electron microscopy (SEM), transmission electron microscopy (TEM) and electron probe microanalysis (EPMA), to assess the products which had been synthesised and the effects that corrosion had on the Hastelloy. Powder X-ray diffraction (PXRD) was also used to identify the phases and crystal structures of the Hastelloy blocks before and after they were exposed to toluene (i.e. before and after carburisation). The graphitic nature of the products that were formed was assessed using laser Raman spectroscopy. The details of each of these characterisation techniques are supplied below.

3.2.1. Optical Microscopy (OM)

An **Olympus BX63** optical microscope equipped with an Olympus DP 80 camera (Figure 3.2), operated under bright-field reflected (BF-RF) conditions (where light was reflected off the sample to produce a dark image with a white background), was used to assess the overall visual condition of the Hastelloy blocks before and after they were exposed to toluene under CVD conditions. Here no sample preparation was required for characterisation. Each sample (i.e. exposed or unexposed Hastelloy block) was placed on a glass slide, which was then placed under an appropriate objective (4 or 10x). Further examination of the surfaces and sub-surfaces of the Hastelloy blocks was performed by using the **FEI Nova Nanolab 600 FEG-SEM**.



Figure 3.2. Olympus BX 63 Optical Microscope.

3.2.2. Scanning Electron Microscopy (SEM)

SEM is generally used to examine the microstructure and chemistry of materials. Electrons are produced at an electron source situated at the top of the column of the microscope as shown in Figure 3.3 [1]. The electrons are accelerated downwards via a sequence of lenses and apertures which creates a beam of focused electrons. Scan coils positioned above the objective lens control the electron beam to be positioned onto the surface of the sample. The scanning of the electron beam allows imaging of a defined area on the sample to be retrieved. A collection of signals are formed as a consequence of the electron-sample interaction. The signals are then detected.

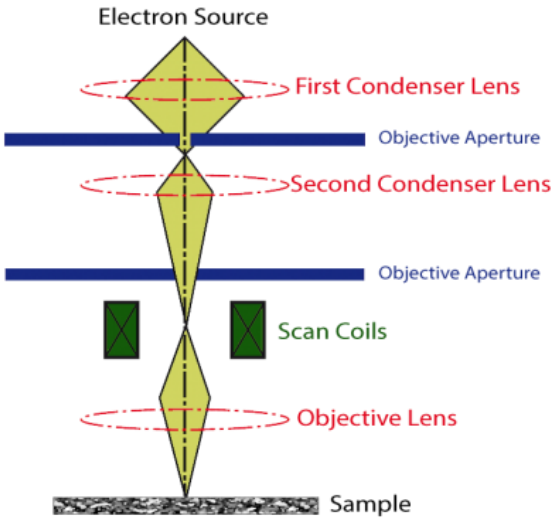


Figure 3.3. A simple schematic of how SEM works**[1]**.

Images of the surfaces of the Hastelloy C276 (both before and after exposure to toluene under CVD conditions), were taken by a **FEI Nova Nanolab 600 FEG-SEM** (Figure 3.4) that was operated at 30 kV with a spot size of 0.63 nA, to examine the formation of carbonaceous products as well as the effect of corrosion caused by MD. In each case, no sample preparation was required. However, the Hastelloy samples were mounted on an aluminium stub with the aid of carbon tape. Images were taken using the secondary electron (SE) mode.

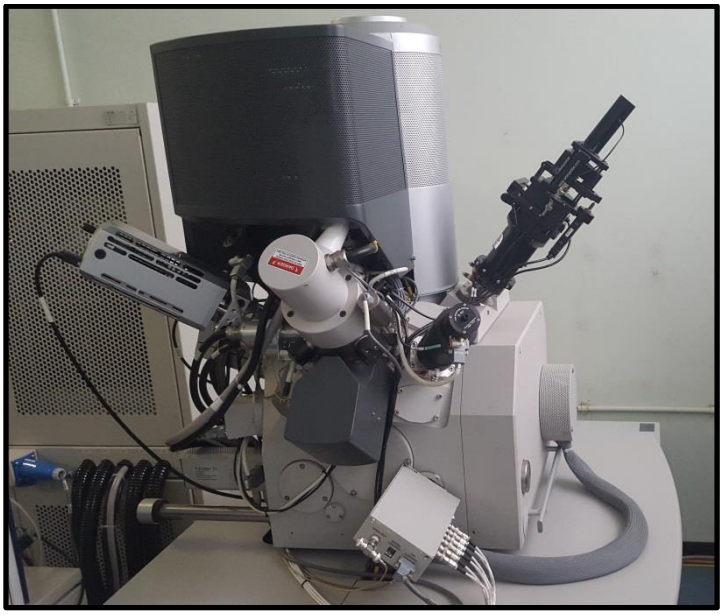


Figure 3.4. FEI Nova Nanolab 600 FEG-SEM/FIB.

3.2.3. Electron Probe Microanalysis (EPMA)

An electron probe microanalyzer is an analytical tool for the non-destructive analysis of the chemical composition of a sample [2, 3]. The sample is bombarded with a focused electron beam in the same way as SEM. The electron interacts with the sample to give an array of four different types of electrons such as back-scattered electrons (BSE), secondary electrons (SE), characteristic X-rays and cathode luminescence light [2]. A wavelength dispersive X-ray spectrometer (WDS) uses crystals which allows for the specific X-ray wavelength or energies for chemical composition [3]. Inelastic collisions of the beam electrons with the electrons in the inner shells of atoms of the sample are generated to produce X-rays and an electron is ejected leaving a vacancy [2]. A higher shell electron fills this vacancy which sheds energy in the form of X-rays [2]. A simple illustration of an electron-probe microanalyzer is shown in Figure 3.5.

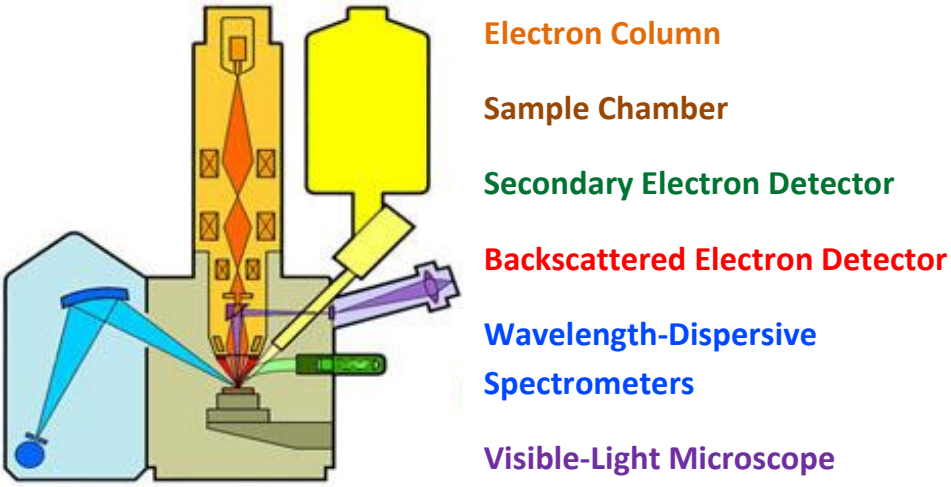


Figure 3.5. A simplified illustration of an electron probe microanalyzer **[2]**.

The elemental compositions of the surfaces of the Hastelloy C276 (both before and after exposure to toluene under CVD conditions), were studied by EPMA. For this purpose a **CAMECA SX5-FE EPMA** (Figure 3.6), equipped with 5 wavelength dispersive X-ray spectroscopy (WDS) detectors and 12 crystals to select X-ray wavelengths for specific elemental compositions was used. Here the distribution/migration of carbon (C-Kα), nickel (Ni-Kα), chromium (Cr-Kα), molybdenum (Mo-Lα), iron (Fe-Kα) and oxygen (O-Kα) were mapped during the MD process. Elemental mapping was executed using a FEG-SEM (CAMECA), a component of the EPMA. The FEG-SEM was operated at 15 kV. No sample preparation was required for each analysis. The variables of the instrument such as sampling depth and interaction volume were kept constant.

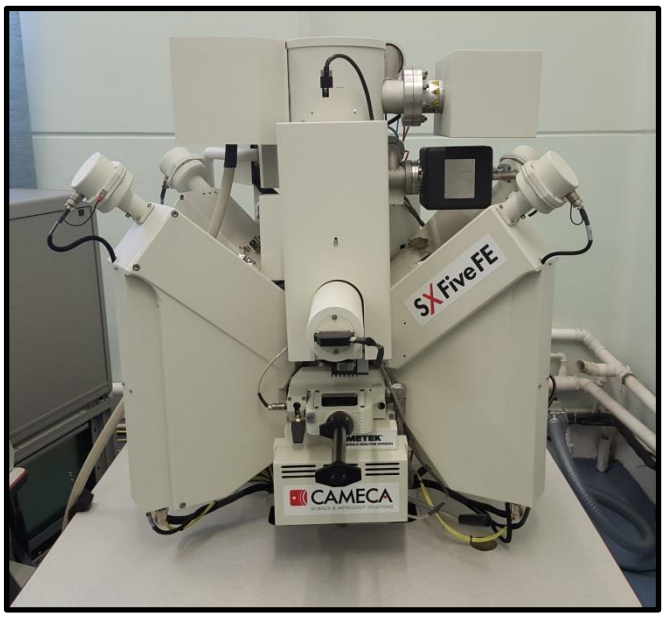


Figure 3.6. CAMECA SX5-FE EPMA.

EPMA has not been widely used in research regarding MD. C.Y. Lin *et al*. [4] have briefly reported line scans of carbon and the constituents of the alloy (Fe, Cr and Ni) investigated.

3.2.4. Transmission Electron Microscopy (TEM)

Unlike SEM where images are produced by detecting secondary electrons from the surface due to the excitation by the primary electron beam, TEM allows electrons from the primary beam to be transmitted though the sample [5]. Similar to SEM, TEM uses electrons supplied from an electron source situated at the top of the microscope. The emitted electrons travel though the column of the microscope which are then focused into a very thin beam by electromagnetic lenses which pass though the sample as seen in Figure 3.7 [6]. Unscattered electrons, depending on the density of the sample, hits a fluorescence screen situated at the base of the microscope which gives rise to a virtual image of the specimen. Depending on the density of the sample, the darkness of the image is varied [6]. Images are generally taken with a camera attached to the microscope.

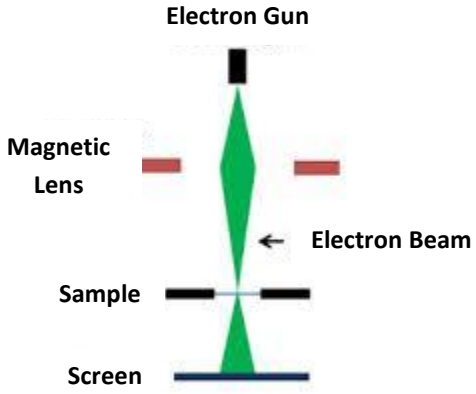


Figure 3.7. A simple schematic of how TEM works **[7]**.

After exposure of the various Hastelloy blocks to toluene under CVD conditions, the products that were formed on their surfaces were removed by suspending these blocks in methanol and sonicating them for 1 h. Thereafter, the resultant suspensions were dispersed onto copper grids, dried and analysed by a **FEI Tecnai T12 TEM** (Figure 3.8) which was operated at 120 kV. The products were analysed for their morphologies as well as for the presence of embedded metal nanoparticles in these carbon nanofilaments indicated the MD phenomena.



Figure 3.8. FEI Tecnai T12 TEM.

3.2.5. Powder X-ray Diffraction (PXRD)

PXRD is an analytical technique that is used for phase identification of crystalline materials [8]. A typical setup of a diffractometer is shown in Figure 3.9 [9]. An X-ray beam is emitted from an X-ray tube and is focused on a sample at an angle Ɵ. The intensity of the X-ray is received at an angle 2Ɵ away from the X-ray source path by an X-ray detector. Over time the incident angle (Ɵ) is increased and the detector angle remains at 2Ɵ above the source path.

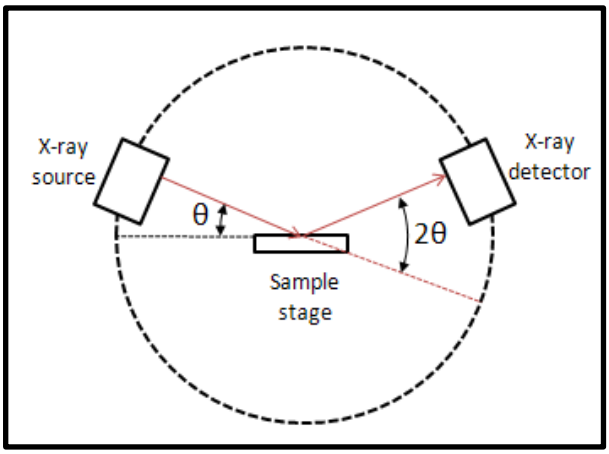


Figure 3.9. A typical setup of a diffractometer **[9]**.

PXRD was used to analyse the bulk composition of the various Hastelloy blocks (both before and after exposure to toluene under CVD conditions) using **a Bruker D2 phaser** (Figure 3.10) equipped with a LynxEye detector. The X-ray tube voltage was operated at 30 kV with a current of 30 mA. Co-K_α radiation was used. The scan ranged between $10° \leq 2\theta \leq 140°$ with a total measurement time of 17 minutes. No sample preparation was required in each case. Each Hastelloy block was mounted on a holder with the aid of plasticine. The plasticine did not interfere with results. The crystallographic planes and phases of the materials were identified using EVA software.

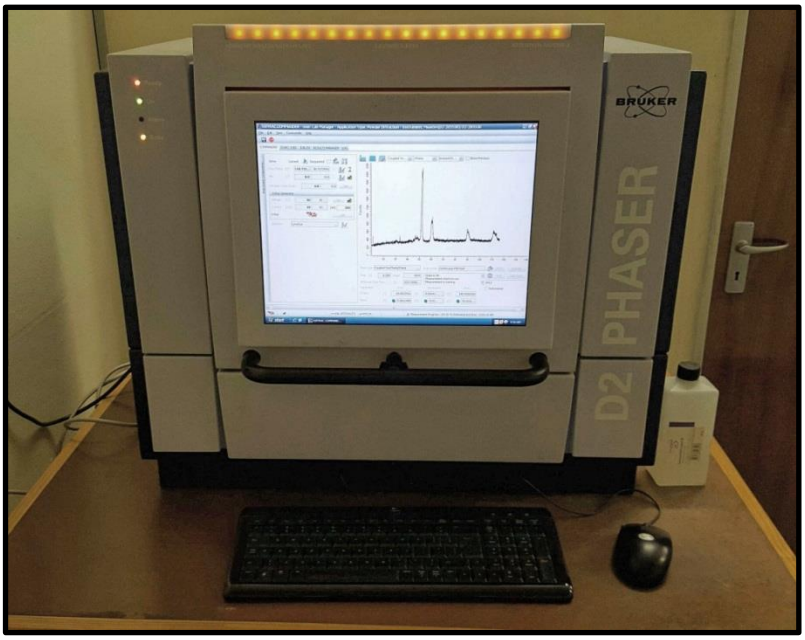


Figure 3.10. Bruker D2 Phaser.

Another XRD instrument **(Bruker D8 Discover)** was used to conduct grazing angle XRD (Figure 3.11). Grazing angle XRD analysis was used to analyse the carbon nanomaterial formed on the surface of Hastelloy as opposed to the bulk of the Hastelloy described above using the **Bruker D2 phaser**. In this case the operation principles were the same as shown in Figure 3.9 above, except the surface was analysed according to a specific grazing incidence of the X-ray beam related to the surface. The **Bruker D8 Discover** was equipped with a LynxEye detector and the X-ray tube voltage was operated at 30 kV with a current of 40 mA. As opposed to Co-K_α radiation used by the **Bruker D2 phaser**, the **Bruker D8 Discover** used Cu-K_α radiation. The scan ranged between $10° \leq 2\theta \leq 90°$ with a total measurement time of 4 hours. The crystallographic planes and phases of the materials were also identified using EVA software.



Figure 3.11. Bruker D8 Discover.

3.2.6. Laser Raman Spectroscopy

Raman spectroscopy is a technique used to observe vibrational, rotational and other low frequency modes in a sample [10]. Raman spectroscopy is based on inelastic scattering of monochromatic light generally from a laser source [11]. When monochromatic light reaches the sample, it is either reflected, absorbed or scattered [12]. The elastic scattered radiation is filtered out at the wavelength corresponding to the laser line (Rayleigh scattering) [12]. The remainder of the light is accumulated and distributed over the detector which records a signal.

Raman bandwidths at 1355 and 1581 cm^{-1} have been reported by Ferrari *et al.* [13] which are respectively related to the crystalline (G) and defect (D) structure of carbon. The G band of graphite originates from E_{2g} symmetry which involves the in-plane bond-stretching motion of pairs of carbon sp^2 atoms as shown in

Figure 3.12(a) [13, 14]. The D peak originates from A_{1g} symmetry which is known to be a breathing mode (Figure 3.12(b)) [13, 14]. This mode is non-existent in high quality graphite and will only be active when disorder is present [13].

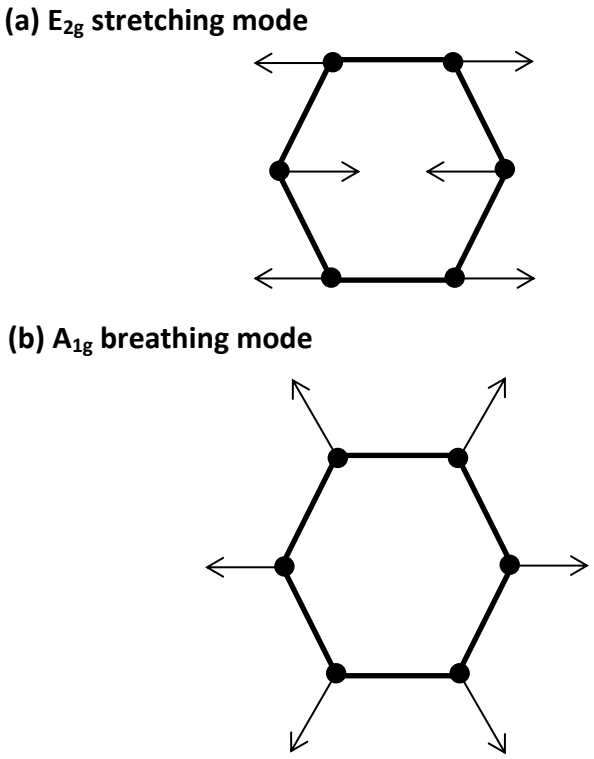


Figure 3.12. Motions of carbon showing the: **(a)** E_{2g} stretching mode (G) and **(b)** A_{1g} breathing mode (D)**[13].**

Laser Raman spectroscopy analyses were performed on the various Hastelloy blocks using a **Horiba Jobin-Yvon Raman Spectrometer (T64000)** (Figure 3.13).

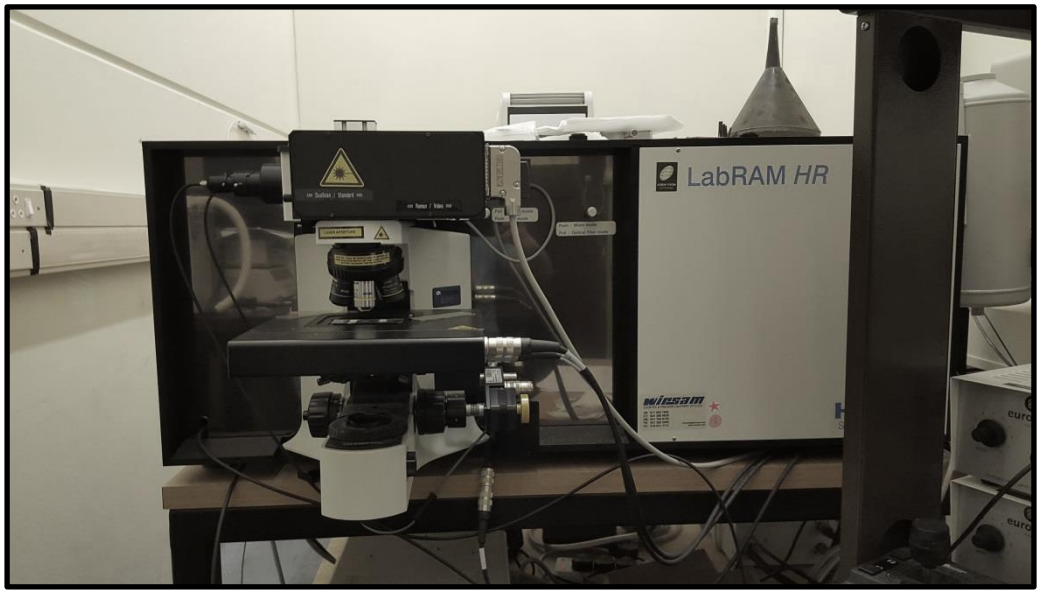


Figure 3.13. Horiba Jobin-Yvon Raman Spectrometer (T64000).

To determine the crystallinity of the carbon, the intensity of the G and D peak, i.e. I_G and I_D, respectively, of the Raman spectrum is measured. The ratio of these peaks gives an indication regarding the crystallinity of the carbon material synthesized. Here, the intensity ratio, I_G/I_D, of the carbonaceous materials that were formed via MD was studied. In each case no sample preparation was required and the measurements were taken directly from the black-coloured carbonaceous deposits that had formed on the surfaces on the various Hastelloy blocks. The spot size used on each block analysed was approximately 1.5 μm in diameter. A wavelength of 514.5 nm from a He-Ar ion laser was used. The detector utilised was a temperature-controlled charged couple device operating at -150 °C. A spectral range of 400-2200 cm^{-1} was recorded.

3.3. References

1. *How an SEM Works*. 2016 [cited 2016 13 April]; Available from: http://www.nanoscience.com/products/sem/technology-overview/how-sem-works/.
2. *Electron probe micro-analyzer (EPMA)*. 2012 [cited 2016 13 April]; Available from: http://serc.carleton.edu/research_education/geochemsheets/techniques/EPMA.html.
3. *Electron Probe Micro-Analysis*. 2010-2012 [cited 2016 13 April]; Available from: http://www.cameca.com/instruments-for-research/epma.aspx.
4. C.Y. Lin and W.T. Tsai, *Nano-sized carbon filament formation during metal dusting of stainless steel.* Materials chemistry and physics, 2003. **82**(3): pp. 929-936.
5. *What is Electron Microscopy?* [cited 2016 13 April 2016]; Available from: https://www.jic.ac.uk/microscopy/intro_EM.html.
6. *The Transmission Electron Microscope*. 2016 [cited 2016 13 April]; Available from: http://www.nobelprize.org/educational/physics/microscopes/tem/.
7. *What is an Electron Microscope? - Definition, Types & Uses*. [cited 2016 13 April]; Available from: http://study.com/academy/lesson/what-is-an-electron-microscope-definition-types-uses.html.
8. *X-ray Powder Diffraction (XRD)*. 2016 [cited 2016 13 April]; Available from: http://serc.carleton.edu/research_education/geochemsheets/techniques/XRD.html.
9. *Powder X-ray Diffraction*. [cited 2016 13 April]; Available from: http://chemwiki.ucdavis.edu/Core/Analytical_Chemistry/Instrumental_Analysis/Diffraction/Powder_X-ray_Diffraction.
10. D.J. Gardiner, *Introduction to Raman scattering*, in *Practical Raman Spectroscopy*1989, Springer. pp. 1-12.
11. *Raman Spectroscopy Instruments*. [cited 2016 14 April]; Available from: http://web.pdx.edu/~larosaa/Applied_Optics_464-564/Projects_Optics/Raman_Spectrocopy/Raman_Spectroscopy_Basics_PRINCETON-INSTRUMENTS.pdf.
12. *The Theory of Raman Spectroscopy*. 1996-2016 [cited 2016 14 April]; Available from: http://www.horiba.com/us/en/scientific/products/raman-spectroscopy/raman-academy/raman-tutorial/the-theory-of-raman-spectroscopy/.
13. A.C. Ferrari and J. Robertson, *Interpretation of Raman spectra of disordered and amorphous carbon.* Physical review B, 2000. **61**(20): pp. 14095.
14. M.S. Dresselhaus, G. Dresselhaus, R. Saito and A. Jorio, *Raman spectroscopy of carbon nanotubes.* Physics reports, 2005. **409**(2): pp. 47-99.

4 DOES METAL DUSTING OCCUR ON HASTELLOY C276 WHEN TOLUENE IS USED AS A HYDROCARBON SOURCE?

4.1. Introduction

As briefly mentioned in Chapter 1, metal dusting (MD) had occurred, in one of the many instances, in charge heater tubes within catalytic reformers due to a mixture of liquid hydrocarbons or naphtha [1, 2]. This type of MD has been studied sparsely and only a few publications have been reported regarding the occurrence of MD due to liquid hydrocarbons. Almost entirely, the literature covering this area has focused on MD and its mechanisms regarding syngas mixtures [3-11]. This focus on syngas has not been misplaced as MD has most prevalently been observed in cracker furnaces and reforming units where CO and H_2 were stored.

MD mechanisms regarding syngas on a variety of alloys, including pure metals such as Fe and Ni, have been incessantly studied [8, 9, 12-18]. In the case of liquid hydrocarbons Dampc *et al.* [1] have reported that the mechanism of MD in charge heater tubes, within catalytic reforming units, has not been fully explained.

Dampc *et al.* [1] have reported that in relation to MD by liquid hydrocarbons, thee simple conditions either influenced or impeded this phenomenon: (1) Alloy composition, (2) Sulphur content and (3) Temperature. Here the three steel alloy compositions that were examined included: 2.25Cr-1Mo, 5Cr-0.5Mo and 9Cr-1Mo. The sulphur content in the catalytic reformer feed was found to have played a positive role in the prevention of MD [1]. Conversely, increased sulphur content adversely affected the activity of the catalyst required for the reformation of the naphtha [1]. Failure cases were reported when: (1) 5% Cr was replaced with 9%

Cr steel, (2) The sulphur content was reduced and (3) The temperature was increased [1].

More recently, Szkodo *et al.* [2]have also reported on the MD of a 10CrMo9-10 steel after 10 years of operation in a semi-regenerative catalytic reformer which contained naphtha (a liquid hydrocarbon mixture). Here, they reported that the inner surfaces of the reformer pipe had formed a thin layer of coke which contained: graphite, Fe and alloy carbides [2].

The purpose of the research in this chapter was to establish whether MD would occur on Hastelloy C276 (a 'highly corrosion resistant alloy') due to the vaporisation of a liquid hydrocarbon, as in the case of Dampc and Szkodo *et al.* [1, 2]. Hence an investigation was undertaken, where toluene was used as the hydrocarbon source and Hastelloy C276 as the metal substrate. Here reactions were conducted at a fixed temperature of 800 °C (as determined from data obtained from my prior Honour's project) and then the products fully characterised.

4.2. Experimental Procedures

In order to assess the full effects that the reaction conditions would have on Hastelloy C276, only polished blocks (i.e. 9 x 9 x 1.5 mm) were used thoughout this study. A CVD reactor shown in Chapter 3 (Figure 3.1) was used to conduct the experiments. However, two modifications were made to this setup in order to first investigate the effects of helium gas (since it was used as a carrier gas) and to then investigate the effects of oxidation on the unreacted/reacted Hastelloy blocks in a lab air environment.

In order to modify the setup to study the effects of helium gas on Hastelloy C276, the carbon source i.e. toluene, was removed from the feed and helium gas was connected directly to the quartz tube. Consequently, the liquid traps were also removed. In terms of the oxidation of the unreacted/reacted Hastelloy blocks, all extensions to the quartz tube were removed to allow for the exposure of these blocks to lab air. In the case of the reacted Hastelloy blocks, lab air oxidation was conducted in order to remove any carbonaceous products which may have been formed thereon to examine the resultant surfaces of the Hastelloy blocks. These investigations (i.e. heat treating in a helium gas environment, oxidation of the unreacted as well as reacted Hastelloy blocks) were all conducted at 800 °C to ensure consistency.

OM and SEM were used to assess the effects of these conditions on the surfaces of the Hastelloy C276 blocks. Likewise the distributions of elements on the surfaces of the Hastelloy C276 blocks under these conditions were mapped using EPMA to understand and justify the migration of metal constituents during MD. PXRD was utilised to confirm the formation of metal oxides. On blocks where black soot-like products were formed, laser Raman spectroscopy was used in order to determine if these products were carbonaceous.

4.3. Results & Discussion

4.3.1. Evidence of metal dusting (MD) on polished Hastelloy C276 blocks using toluene as a hydrocarbon source

4.3.1.1. Polished untreated Hastelloy blocks exposed to gaseous helium at 800 °C

4.3.1.1.1. Optical Microscopy (OM)

Experiments were performed to establish if MD would occur under different conditions with polished Hastelloy C276 blocks. Firstly, polished Hastelloy C276 blocks were subjected to reaction conditions (800 °C for 1 h) with helium gas only (i.e. in the absence of the hydrocarbon source - toluene). An OM image of one of these blocks (Figure 4.1 (a)) and an unreacted polished block for comparison (Figure 4.1 (b)) revealed that under such conditions the surface had changed colour from a shiny silver to a dull mixture of grey black and brown.

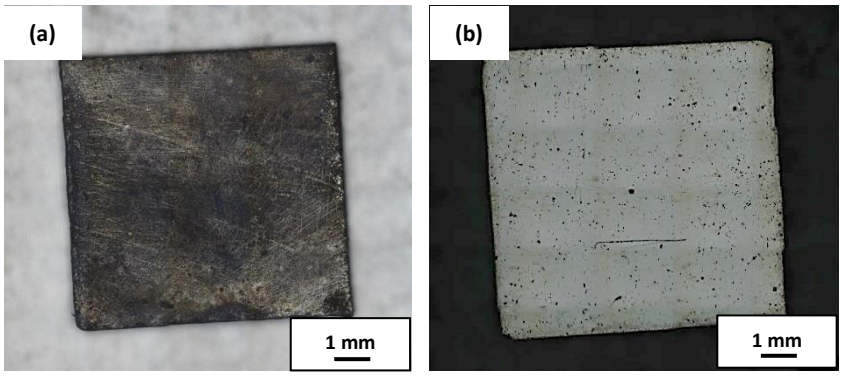


Figure 4.1. OM images of a polished Hastelloy C276: **(a)** After having been heat treated at 800 °C in helium gas only and **(b)** In its unreacted form.

Moreover, the surface after exposure to helium appeared rough when compared to the smooth polished surface. The black background in Figure 4.1 (b.) compared to the grey background in Figure 4.2 (a.) and later Figures 4.7, 4.11 and 4.17 was due to the image taken in dark-field (DF) mode compared to the reflected bright field mode (RF-BF) *(see Section 3.2.1)*, so the light beam was not reflected away from the block due to the shiny polished surface.

4.3.1.1.2. Scanning Electron Microscopy (SEM)

Further analyses of the polished and unpolished blocks shown in Figure 4.1(a) and (b) were done using SEM to observe more noticeable features.

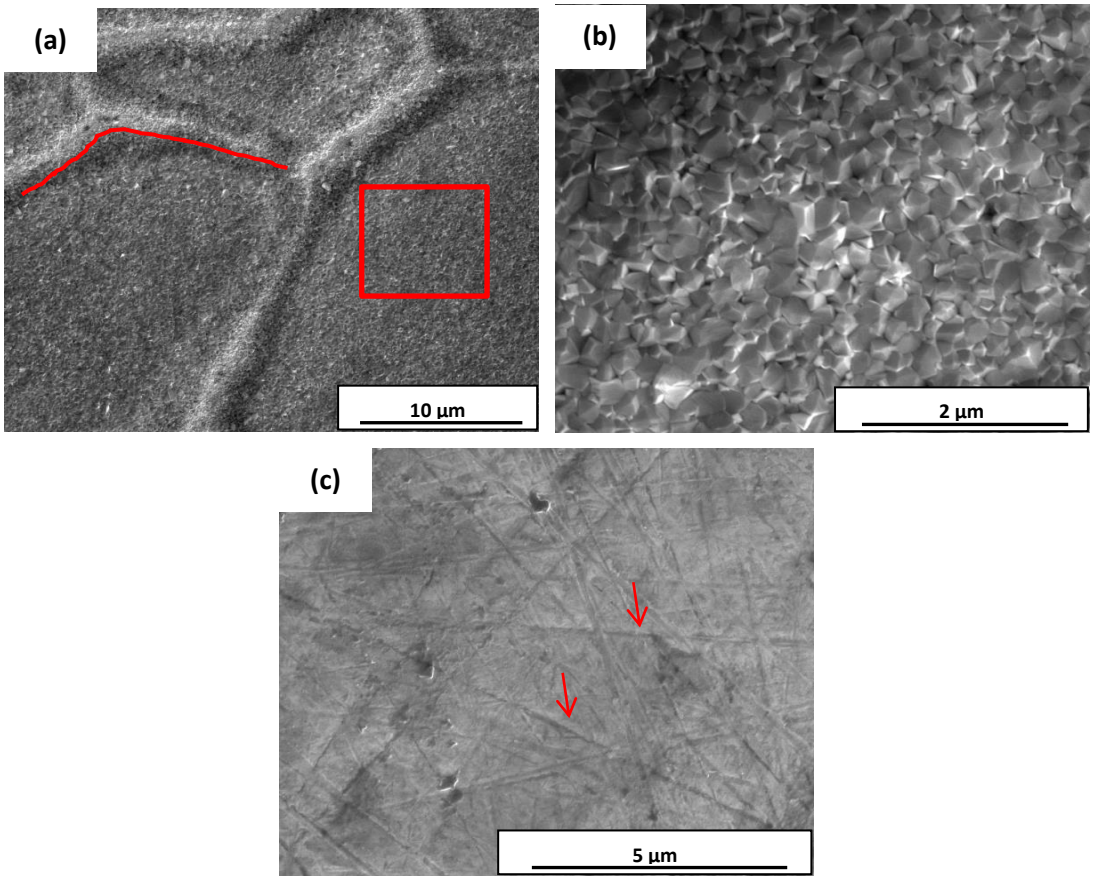


Figure 4.2. SEM micrographs showing: **(a)** The effect of temperature (800 °C) and helium gas on a polished Hastelloy C276 block, **(b)** A magnified section of (**a**), and **(c)** A polished, untreated Hastelloy C276 block.

It was evidently seen under SEM that grain boundaries were formed on the surface of Hastelloy when exposed to helium for 1 h (Figure 4.2(a.) - see red line which traces one boundary). Further investigation of the area marked off in red in Figure 4.2(a.) also revealed the disintegration of surface crystallites (Figure 4.2(b.)). None of these features were seen on an unreacted Hastelloy block under SEM (Figure 4.2(c.), where only polish marks were observed (see arrows). However, the visibility of the grain boundaries, as was seen here, might be as a consequence of intergranular corrosion that occurs when metal samples have been exposed to heat treatment [19]. Intergranular corrosion will be further explained in *Section 4.3.1.1.3*.

4.3.1.1.3. Electron Probe Microanalysis (EPMA)

In addition to SEM, EPMA were performed, in order to map the distribution of elements when an untreated blank Hastelloy block was subjected to helium at 800 °C. For comparison purposes, a polished untreated Hastelloy block was initially mapped under EPMA (Figure 4.3). The SEM micrograph of the polished untreated Hastelloy C276 block on which the elements were mapped is shown in Figure 4.3(a). Ni, the element with the highest abundance in Hastelloy C276 unpredictably had lower counts on the surface, whereas Cr had higher counts, as shown in Figures 4.3(b) and (c) respectively. This observation suggested that the Cr content had become more concentrated on the surface of Hastelloy C276 compared to the bulk, since Cr is known to be a highly corrosive resistant element. Mo with a slightly lower composition than Cr (Table 3.1 - *Section 3.1.1.1*) had much lower counts than Cr as indicated in Figure 4.3(d). This suggested that the Mo concentration was relatively low on the surface and implied that most of the Mo was situated in the bulk of Hastelloy C276. The Fe content was evenly distributed over the surface as shown in Figure 4.3(e). The oxygen (O) content was also mapped to determine if passive oxidation had taken place. Here it was noted that the overall O content was very small with only a few scattered areas where there was a very small amount of O on the surface (see arrows in Figure 4.3(f)). Overall, mapping the constitutional elements (Ni, Cr, Mo and Fe)

of a polished Hastelloy C276 block, which had undergone no treatments, revealed that they were fairly evenly distributed over the surface relative to their different abundances in the alloy.

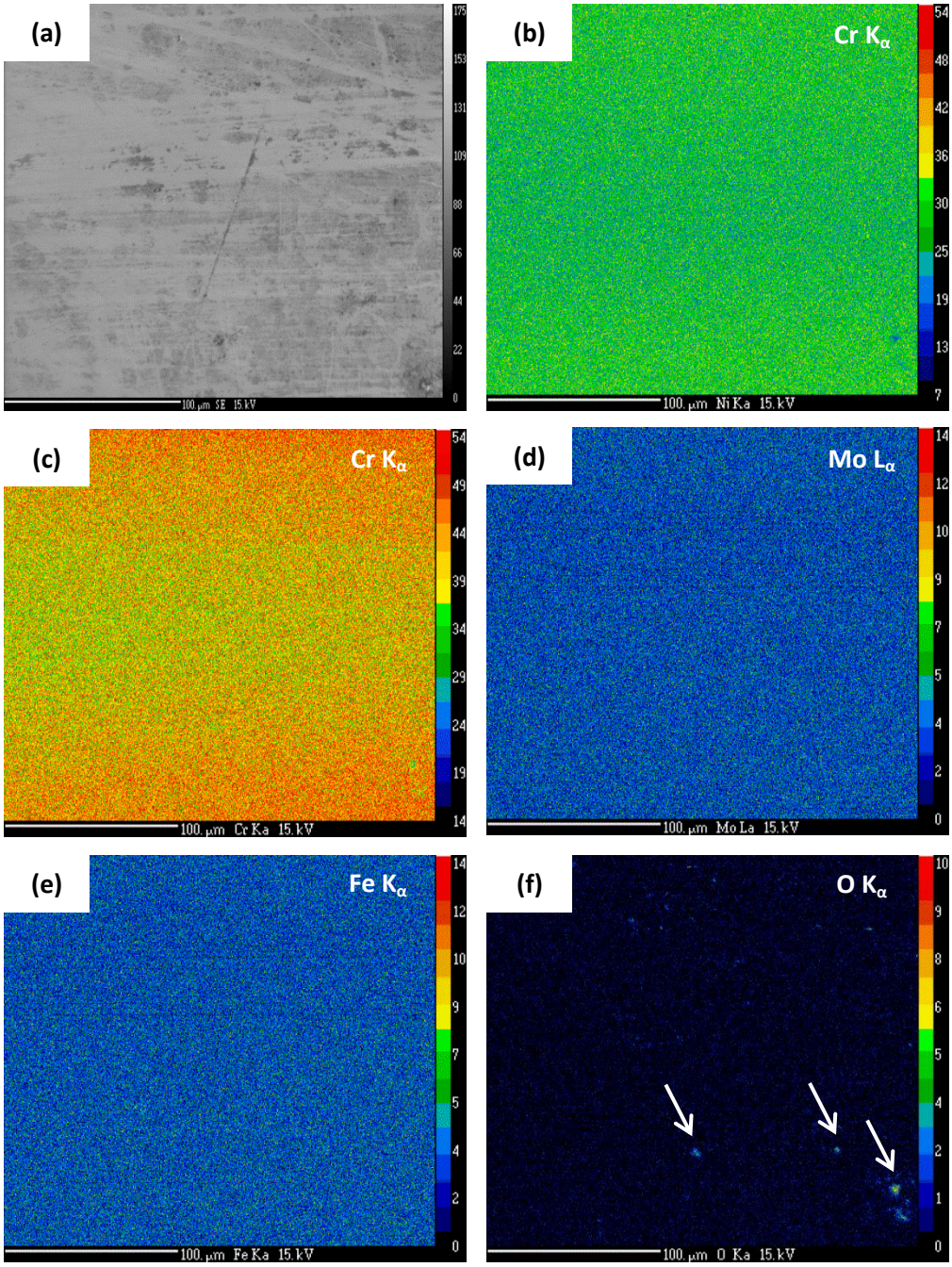


Figure 4.3. Elemental maps of a polished untreated Hastelloy C276 surface showing: **(a)** A SEM micrograph of the mapped area, **(b)** Ni K_α, **(c)** Cr K_α, **(d)** Mo L_α,**(e)** Fe K_α and **(f)** O K_α.

Elemental mapping of the Hastelloy block that was exposed to helium at 800 °C is shown in Figure 4.4. Elemental mapping was done on the area shown in Figure 4.4(a) which was similar to Figure 4.2(a) that was taken on a high resolution SEM (**FEI Nova Nanolab 600 FEG-SEM**).

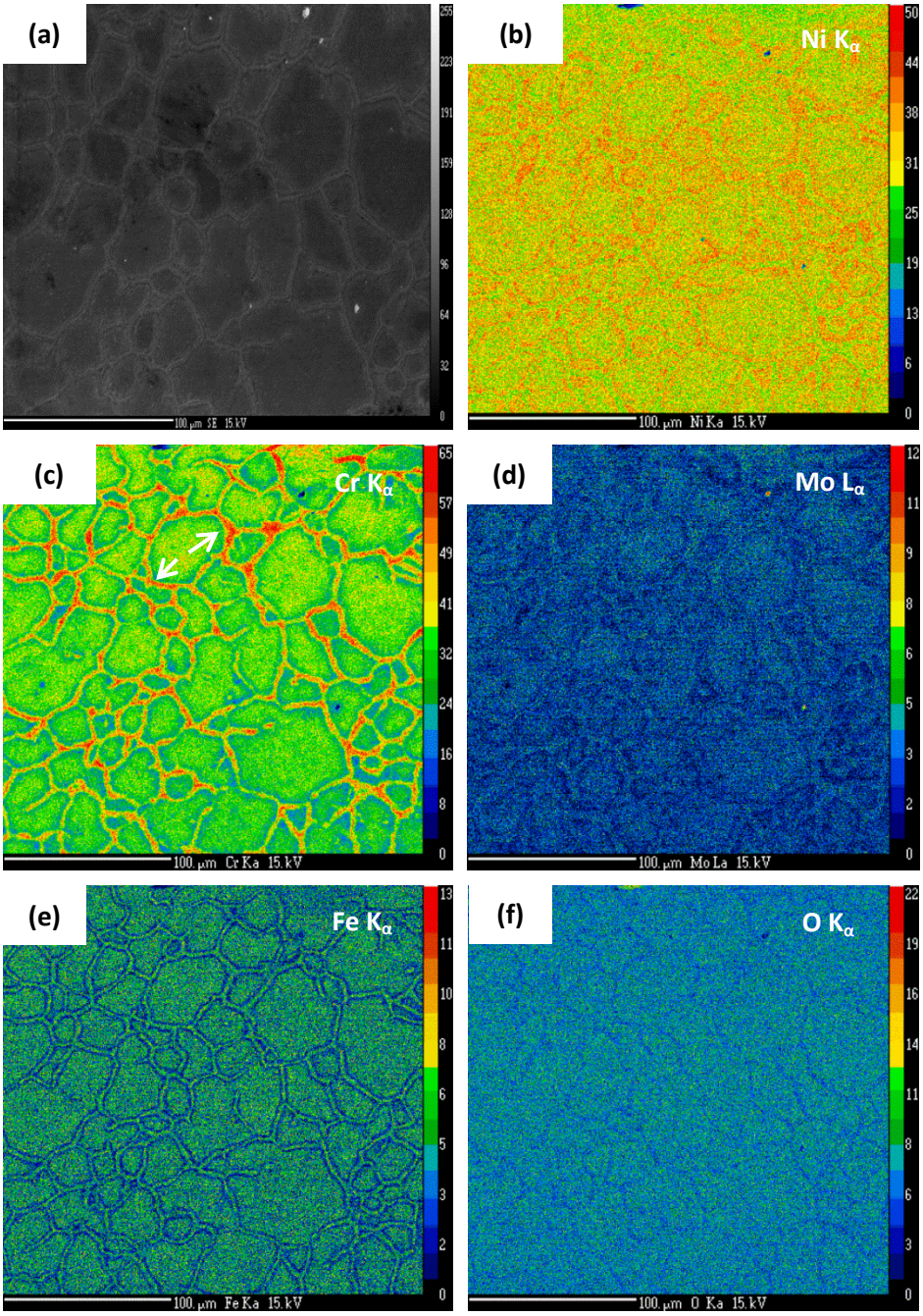


Figure 4.4. Elemental maps of the Hastelloy C276 surface that was heat treated at 800 °C in helium gas for 1 h showing: **(a)** A SEM micrograph of the mapped area, **(b)** Ni K_α, **(c)** Cr K_α, **(d)** Mo L_α,**(e)** Fe K_α and **(f)** O K_α.

Compared with the untreated Hastelloy block, Ni was seen to be evenly distributed on the surface except at the borders of the grain boundaries, where the Ni content was slightly higher (Figure 4.5(b)). However, the distribution of Cr was significantly different to that of Ni as shown in Figure 4.4(c). Here Cr precipitates appeared to be highly nucleated in the grain boundaries (see arrows in Figure 4.4(c)), while the areas adjacent to these boundaries (represented in blue) showed a depletion of Cr precipitates, followed by an increase towards the centre (yellow – green). The depletion of Cr adjacent to the grain boundaries may have led to a corrosion known as intergranular corrosion. Intergranular corrosion has been known to occur under favourable heat treatment conditions and has been attributed to the depletion of Cr from areas adjacent to grain boundaries in which Cr carbides were precipitated [19-21]. This process has been termed: sensitization [19, 21]. Although the carbon weight percentage was not reported in Table 3.1 (*see Section 3.1.1.1*) due to its low amount, which was likely below the detection limit of the X-ray fluorescence spectrometer that was used to analyse it by the suppliers, the manufacturer's specifications of Hastelloy C276 stipulated that it contained a maximum weight percent of 0.01% [22]. In investigations by Tedmon *et al.* [19] regarding the intergranular corrosion of austenitic stainless steel, they found that the carbon content therein varied between 0.003 – 0.11 weight percent, which was in range with Hastelloy C276 and consistent with these observations. Similarly Yin *et al.* [20] have described the emergence of Cr-rich carbides which drew Cr from the grain boundaries and the adjacent matrix, having left a Cr depleted zone adjacent to the grain boundary. When the Cr in the depleted zone was lower than a critical level, the alloy was then susceptible to environmental corrosion which advanced to intergranular attack or intergranular stress corrosion cracking [20].

An investigation was conducted to establish if Cr rich carbides were indeed precipitated in this study. Once again the carbon content was mapped using the SEM micrograph shown in Figure 4.4(a.). The C K_α map is shown in Figure 4.5(a.), which was then overlaid onto the Cr K_α map that is shown in Figure 4.5(b.). A portion of this map was then cropped for further inspection (Figure 4.5

(c)). Here the Cr K_α map was represented in shades of red for uniformity. In this instance, as explained previously, bright red represented a high number of counts of Cr which were observed to be accumulated in the grain boundaries (see arrow 1 in Figure 4.5 (c)). On the other hand the dark red to black colours represented low counts of Cr. These were observed to be adjacent to the grain boundaries (see arrow 2 in Figure 4.5 (c)). Although the C content was seen to be generally randomly distributed, in most areas the highest C content was found to be close to the grain boundary regions. This confirmed the observation that intergranular corrosion had taken place.

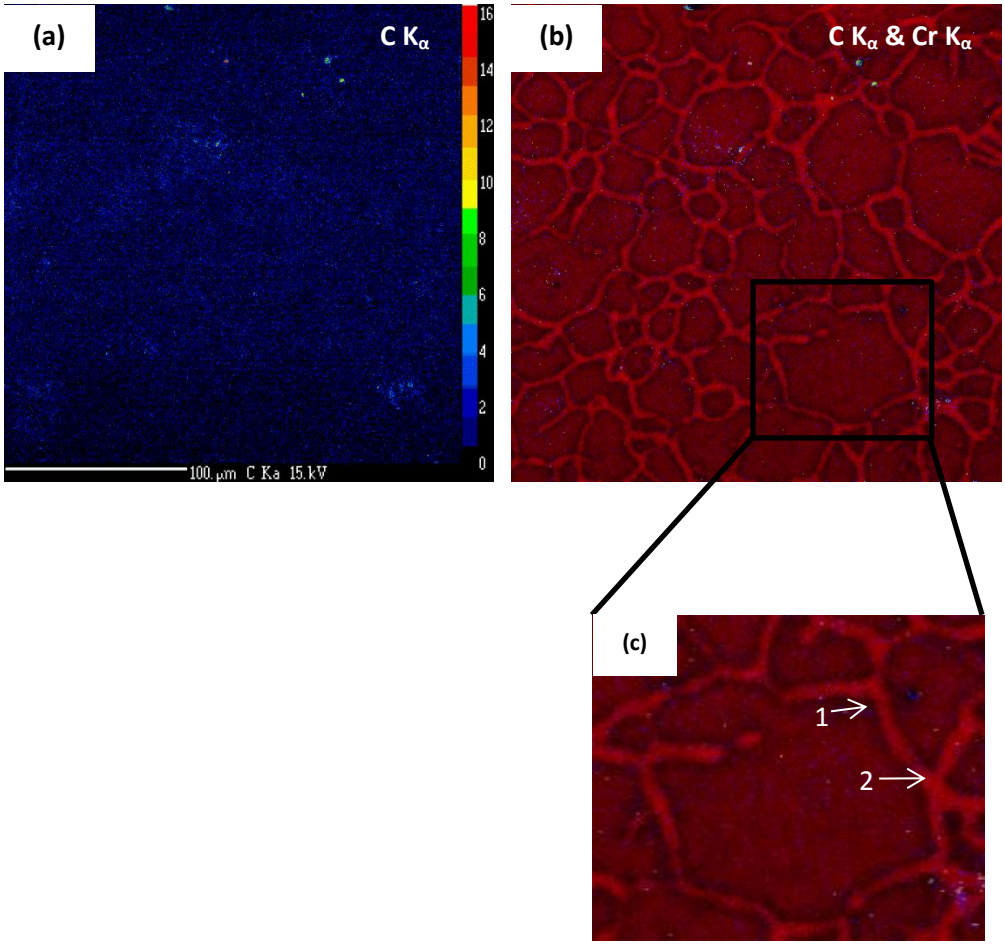


Figure 4.5. Elemental map of the Hastelloy C276 surface that was heat treated at 800 °C in helium gas for 1 h showing: **(a)** C K_α, **(b)** C K_α which was overlaid onto Cr K_α and **(c)** A magnification of (**b**) where C K_α and Cr K_α were overlaid onto each other.

The distribution of Mo was relatively constant over the surface and in grain boundaries as depicted in Figure 4.4(d). The Fe distribution (Figure 4.4(e)) was also relatively constant on the surface of the Hastelloy C276 except on the borders of the grain boundaries where they were recorded to be relatively low. The oxygen content was also mapped as seen in Figure 4.5(f) and was found to be relatively constant over the surface with lower oxygen content in the grain boundaries. However, the oxygen content in the He treated Hastelloy block was substantially higher than in the untreated one (see Figures 4.3(f) and 4.4(f) for comparison). This suggested that somehow during the heat treatment of the Hastelloy in helium, more oxides had formed. The formation of these oxides was therefore investigated further using PXRD.

4.3.1.1.4. Powder X-ray Diffraction (PXRD)

The helium treated and untreated Hastelloy blocks were subjected to PXRD for analysis as shown in Figure 4.6.

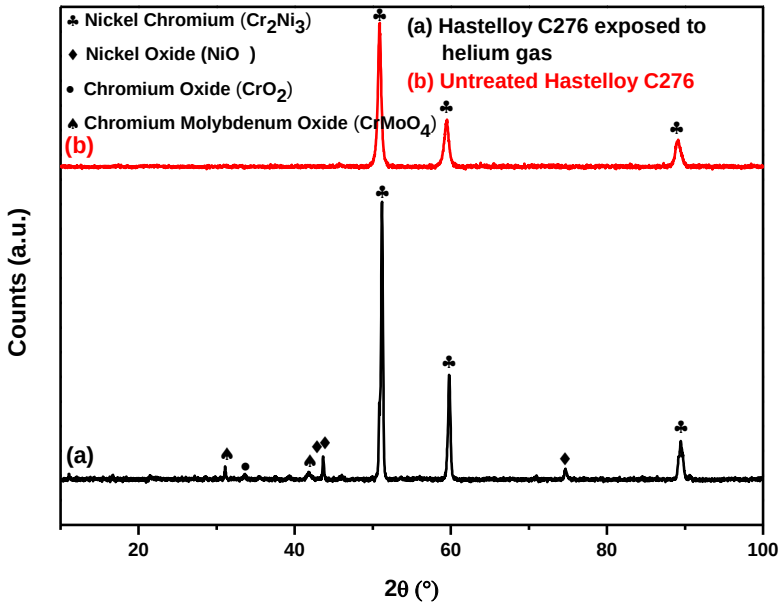


Figure 4.6. PXRD patterns showing Hastelloy C276: **(a)** After exposure to helium at 800 ^{o}C (black pattern) and **(b)** Untreated i.e. in its pristine polished form (red pattern).

PXRD analysis of the unreacted Hastelloy block before exposure to helium gas at 800 ^{o}C showed that the main phase present was a chromium nickel phase (Cr_2Ni_3). However, after exposure to helium gas at 800^{o}C thee new oxide phases (i.e. NiO, CrO_2 and $CrMoO_4$) were present in addition to the chromium nickel alloy (Cr_2Ni_3). This indicated that oxidation of the Hastelloy surface had taken place during the reaction. Since all air had been removed from the reactor prior to the reaction (*see Section 3.1.2 for experimental conditions*), the source of the oxygen was sought. It was found that helium gas, while very pure, still contained trace quantities of moisture ($\leq$3 ppm) and oxygen ($\leq$2 ppm). Hence the oxidation on the surface of Hastelloy C276 had taken place at 800 °C due to the minute quantities of moisture and oxygen contained in the helium. However, oxidation during the MD process with syngas has not been an uncommon observation, especially since the CO/CO_2 has been able to provide an oxidizing environment. Hence, the grey/black/brown formations, which were observed on the surface of Hastelloy C276 when heated treated in helium (Figure (4.1(a)), were evidently oxides (i.e. NiO, CrO_2 and $CrMoO_4$) as identified in the PXRD pattern shown in Figure 4.6. Indeed, Grabke [14] has noted that oxidation of Cr was possible if experiments were carried out in an oxygen containing atmosphere.

4.3.1.2. Polished Untreated Hastelloy blocks exposed to laboratory air at 800 °C

4.3.1.2.1. Optical Microscopy (OM)

In studies which were conducted later (*see Section 4.3.1.3*), polished Hastelloy blocks, which had been exposed to toluene at 800 °C, were heat treated in laboratory air to remove any products which had formed in the reaction between toluene and the blocks. This was done to study the effects that these products may have had on the surfaces of these polished Hastelloy blocks. However, it was unclear what effect the heat treatment in laboratory air alone would have on these

blocks. Hence experiments were conducted where polished untreated blocks were exposed to laboratory air at 800 °C.

OM was used to examine the surfaces of the Hastelloy blocks before and after exposure to laboratory air at 800 °C. Here a silver, shiny coloured polished block (Figure 4.1(b) – before exposure) turned to mixtures of grey, black and brown (Figure 4.7) after exposure to laboratory air at 800 °C. It was noted that the colour change was more intense than that observed on the Hastelloy block exposed to gaseous helium at 800 °C (Figure 4.1(a)). This was most likely due to the higher concentration of oxygen that was present in laboratory air.

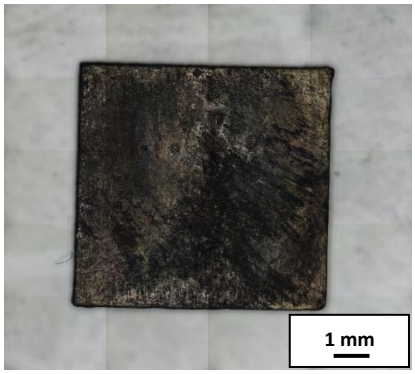


Figure 4.7. OM image of a polished Hastelloy C276 block after having been heat treated in laboratory air at 800 °C.

This block was then analysed by SEM to resolve if the pre-existing grain boundaries had become more visible as in the case when an equivalent block had been exposed to a gaseous helium environment at 800 °C.

4.3.1.2.2. Scanning Electron Microscopy (SEM)

The polished Hastelloy C276 block was analysed by SEM after having been heat treated in laboratory air at 800 °C. Once again this revealed that grain boundaries, similar those which originated when the blocks were exposed to helium at 800 °C had become more visible when the polished untreated Hastelloy block was

exposed to air at 800 °C (Figure 4.8). However, one major difference between the exposure to helium and air that was observed under SEM was that crystallites in the block exposed to air were not as disintegrated as those when the block was exposed to gaseous helium (Figure 4.8).

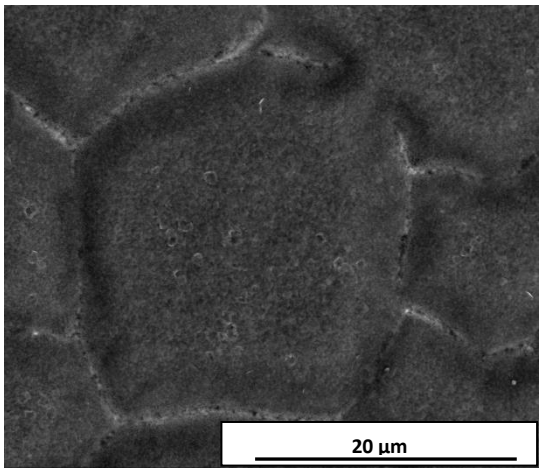


Figure 4.8. A SEM micrograph showing the effect of laboratory air at 800 °C on a polished Hastelloy C276 block.

The Hastelloy block was then investigated by EPMA to determine if the distribution of elements were similar or different to those of the block exposed to gaseous helium at 800 °C.

4.3.1.2.3. Electron Probe Microanalysis (EPMA)

The elemental compositions of the Hastelloy treated in laboratory air at 800 °C were mapped on the area of the SEM micrograph shown in Figure 4.9(a). As compared to the Hastelloy block exposed to helium gas at 800 °C (Figure 4.4), not all of the Cr migrated to the grain boundaries and a large amount of Cr was still observed on the surface of the Hastelloy (Figure 4.5(c)). However, the Ni content was much lower in the grain boundaries as compared to the surface when exposed to laboratory air (Figure 4.9(b)). This may have been due to the increase in Cr content in the grain boundaries as seen in Figure 4.9(c).

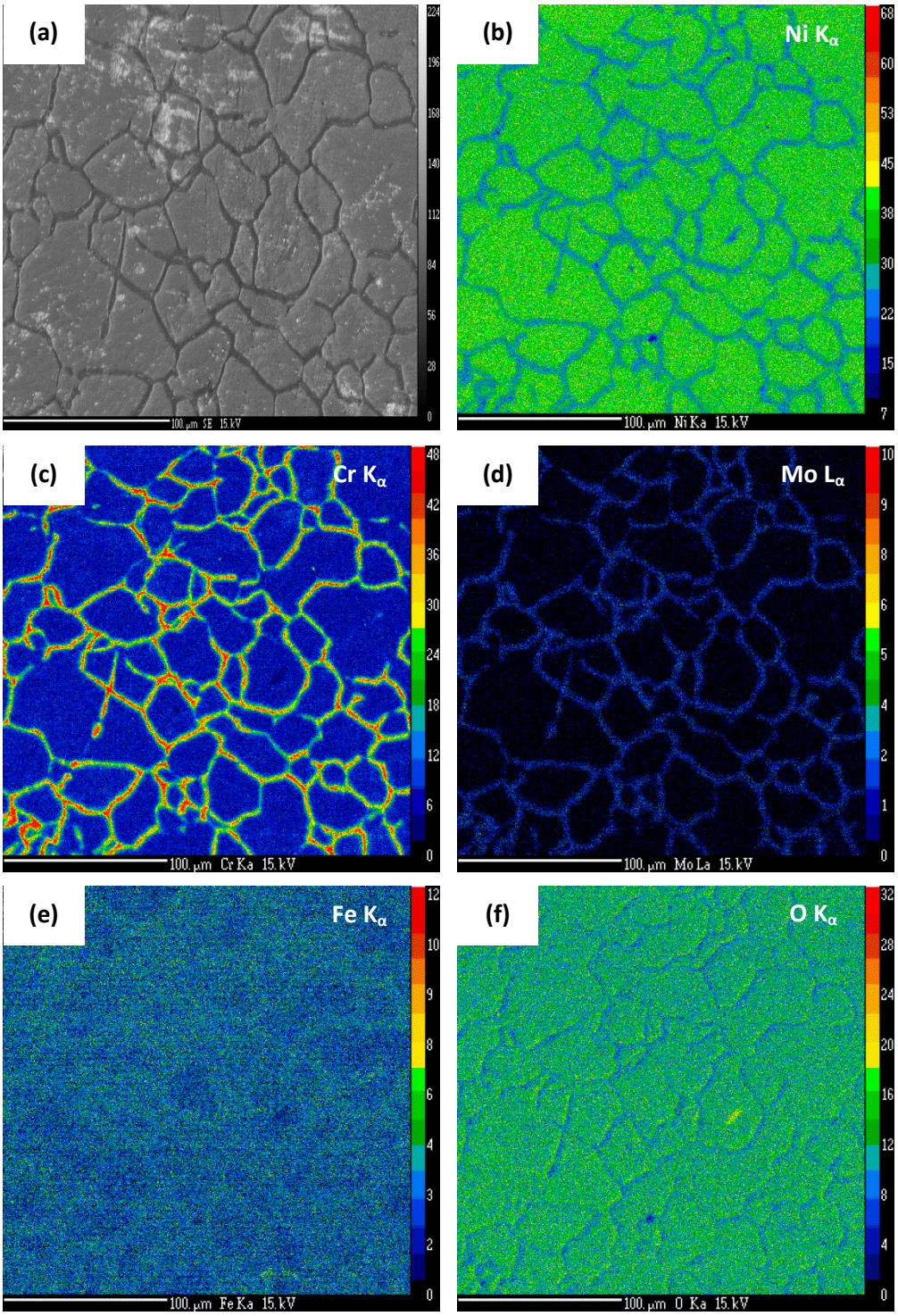


Figure 4.9. The elemental maps of the surface of a Hastelloy C276 block that was heat treated at 800 °C in laboratory air for 1 h showing: **(a)** A SEM micrograph of the mapped area, **(b)** Ni K_α, **(c)** Cr K_α, **(d)** Mo L_α,**(e)** Fe K_α and **(f)** O K_α.

As previously mentioned the Cr distributions in the Hastelloy blocks that were treated in helium and laboratory air showed both similar and dissimilar trends. For instance in both blocks a relatively high Cr count in the grain boundaries was observed, suggesting that some of the Cr had migrated to the grain boundary (compare Figure 4.4(c) with Figure 4.9(c)). However, very low Cr counts were observed on the surface of the Hastelloy block exposed to laboratory air (Figure 4.9(c)), while higher Cr counts were observed on the surface of the Hastelloy block exposed to helium gas (Figure 4.4(c)). As previously mentioned, this may suggest that sensitization took place faster in laboratory air than in helium gas at 800 °C.

The Mo distributions were found to be dissimilar on the surfaces of the blocks exposed to laboratory air at 800 °C (Figure 4.9(d)) as compared to helium gas (Figure 4.4(d)). In the former a higher Mo content was observed in the grain boundaries than in the latter. In a study regarding the resistance to sensitization and intergranular corrosion though extreme randomization of grain boundaries, Wasnik *et al.* [23] showed that the presence of Mo (in stainless steel 316) supressed sensitization, enhanced passivity and consequently lowered the degree of intergranular corrosion. This implies that in this study Mo may have migrated to the grain boundaries to lower the degree of sensitization of the C276 Hastelloy blocks.

When Fe was mapped, its distribution was found to be more uniform on the surface of the block exposed to laboratory air (Figure 4.9(e)) as compared to that of the block that was treated in helium (Figure 4.4(e)). Finally the oxygen distribution for the block exposed to laboratory air (Figure 4.9(f)) was found to be very similar to that of the block exposed to helium gas (Figure 4.4(f)). However, as expected the oxygen counts for the former were higher than the latter, as there was more oxygen in the laboratory air than in the helium gas.

The Hastelloy blocks were then analysed using PXRD to determine if the oxides formed were the same as those formed when exposed to helium at 800 °C.

4.3.1.2.4. Powder X-ray Diffraction (PXRD)

The PXRD analyses of the untreated Hastelloy blocks and those exposed to laboratory air were performed. Here the patterns obtained revealed that the block exposed to laboratory air (Figure 4.10 (a)) had two different oxides present (i.e. $NiCr_2O_4$ and $Ni(MoO_4)$ that were not present either in helium gas ((Figure 4.6) or in the untreated block (Figure 4.10 (b)). As before the difference in these oxides was most likely due to the different concentrations of oxygen present in the laboratory air and the helium gas.

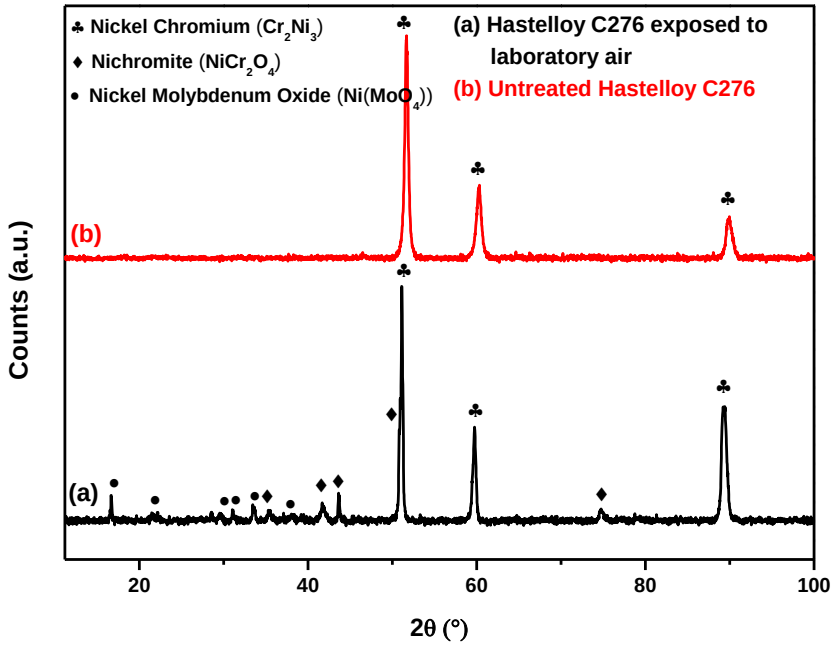


Figure 4.10. PXRD pattern showing Hastelloy C276: **(a)** Exposed to laboratory air at 800 °C and **(b)** Untreated (i.e. in its pristine polished form).

4.3.1.3. Polished untreated Hastelloy blocks exposed to toluene – Metal Dusting (MD)

4.3.1.3.1. Optical Microscopy (OM)

After investigating the effect of helium gas (which was employed in the reaction setup as a carrier gas) and laboratory air (which was used to burn off the soot-like products which were formed – to be discussed later in this section) on polished Hastelloy C276 blocks, polished untreated Hastelloy blocks were then subjected to reaction conditions (800 °C for 1 h) where vaporized toluene (the carbon source) and gaseous helium at 80 mL/min were simultaneously passed over them. An OM image of one of these blocks (Figure 4.11) was taken and it was observed that a black soot-like material covered the entire surface of the Hastelloy block. In addition to this a mass increase of 0.3 mg was recorded.

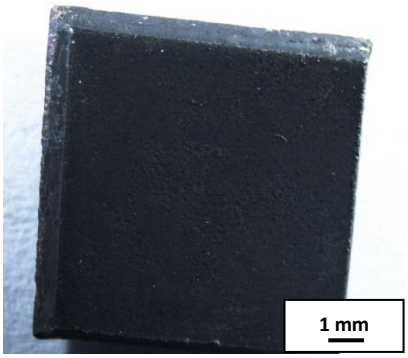


Figure 4.11. An OM image of a polished Hastelloy C276 after having been subjected to vaporized toluene and gaseous helium (80 mL/min) at 800 °C for 1 h.

4.3.1.3.2. Laser Raman Spectroscopy

In order to determine the inherent nature of the black soot-like products, some of these were carefully scraped off the surface of the Hastelloy block which had been subjected to vaporized toluene and gaseous helium (80 mL/min) at 800 °C for 1 h. Laser Raman spectrum of these black soot-like products were then obtained (Figure 4.12).

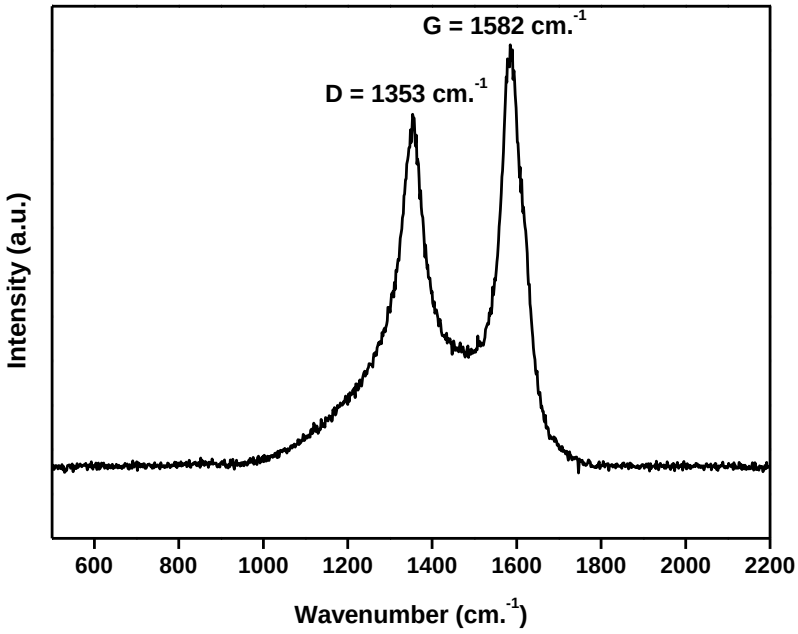


Figure 4.12. A laser Raman spectrum of a small sample of the black soot-like products which had formed on the surface of the Hastelloy block that had been subjected to vaporized toluene and gaseous helium (80 mL/min) at 800 °C for 1 h.

The Raman spectrum revealed distinct D (1353 cm^{-1}) and G (1582 cm^{-1}) bands which was consistent with the formation of carbonaceous nanomaterials (Figure 4.12). These findings were in agreement with that of Ferrari *et al.* [24] who reported D and G bands at 1355 and 1581 cm^{-1} respectively, as explained in *Section 3.2.6*. Hence the black soot-like products that had formed on the surface of the Hastelloy block that had been subjected to vaporized toluene and gaseous helium (80 mL/min) at 800 °C for 1 h were indeed carbonaceous. Consequently

this analysis confirmed that the highly corrosion resistant Hastelloy C276 had been carburized under these conditions.

4.3.1.3.3. Scanning Electron Microscopy (SEM)

Further analysis was then performed by using SEM to establish the morphology of the carbonaceous products which had formed (Figure 4.13). Here it was observed that, under these reaction conditions, carbon nanofilaments and graphite layers had formed on the surface of the Hastelloy (Figure 4.13). A similar result has been reported by Zhang *et al.* [17] on ***polished*** Ni surfaces after 2 h of reaction. However, unlike in this study, a 50%CO-48.9%H_2-1.1%H_2O mixture was used. Similarly Zhang *et al.* [17] noted that the reaction kinetics and morphologies of the deposited carbon were affected by the composition of the gas consumed.

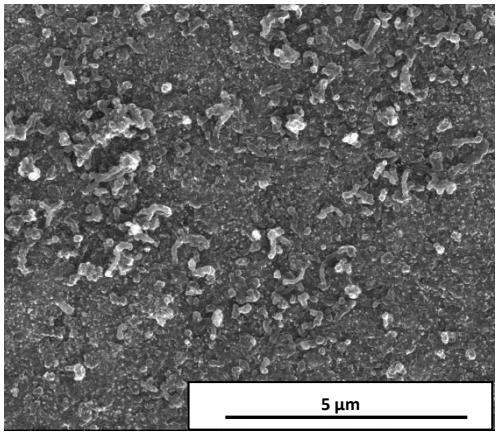


Figure 4.13. A SEM micrograph showing the carbonaceous products formed on the surface of Hastelloy C276 due to reaction with vaporized toluene at 800 °C.

4.3.1.3.4. Electron Probe Microanalysis (EPMA)

EPMA elemental mapping was one again conducted on the area of the SEM micrograph shown in Figure 4.14(a), similar to the one shown in Figure 4.13 (taken on a high resolution SEM (**FEI Nova Nanolab 600 FEG-SEM**).

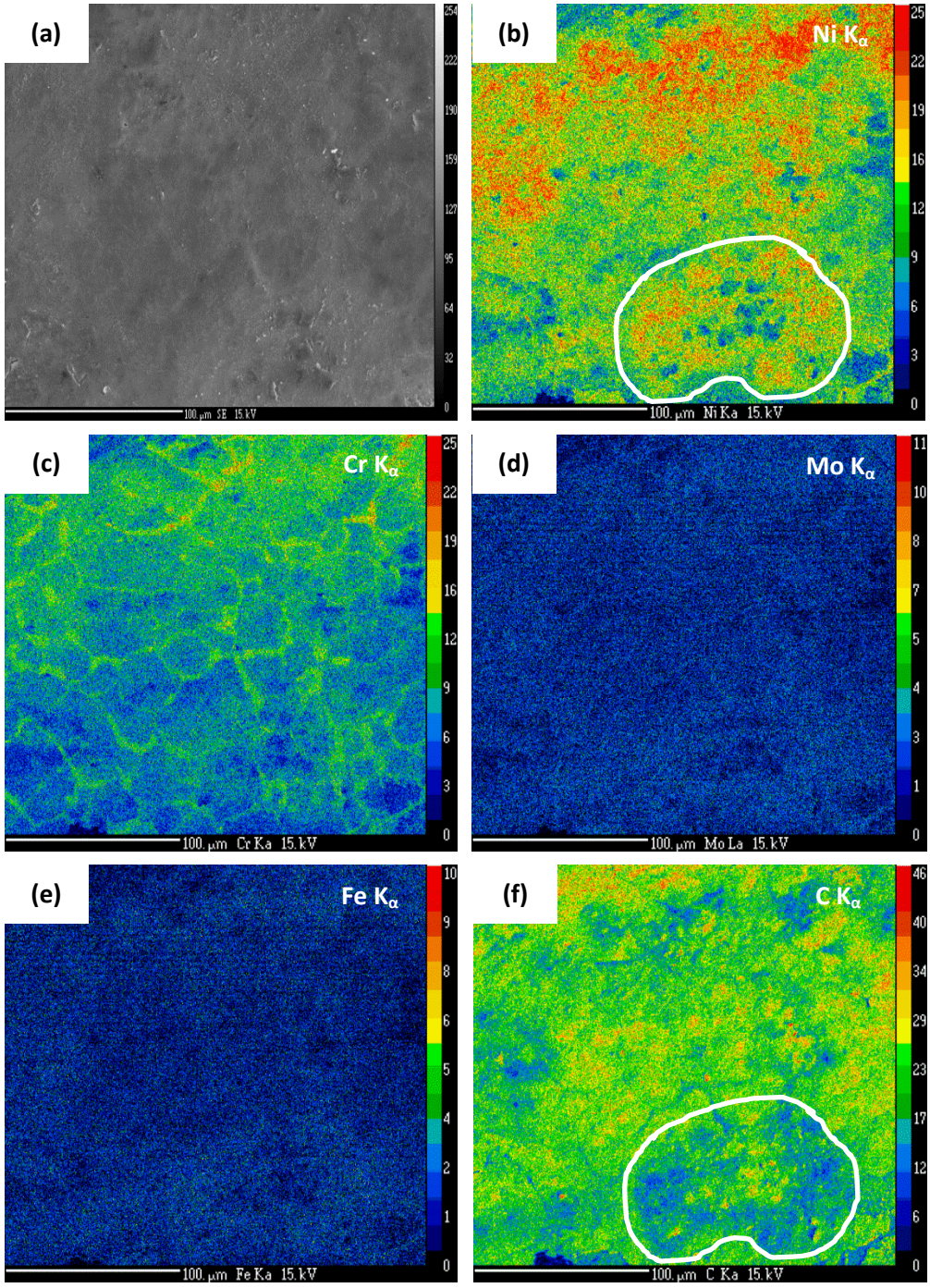


Figure 4.14. Elemental maps of a polished Hastelloy C276 surface exposed to toluene for 1 h at 80 mL/min showing: **(a)** A SEM micrograph of the mapped area, **(b)** Ni K_α, **(c)** Cr K_α, **(d)** Mo L_α, **(e)** Fe K_α and **(f)** C K_α.

Ni, as seen in Figure 4.14(b), predictably showed higher counts since it was the main constituent of Hastelloy C276. However, the highest number of counts for Ni were recorded in areas where carbon counts (Figure 4.14(f)) were relatively low (compare outlined areas in (Figure 4.14(b)) and (Figure 4.14(f)). This suggested that carbon deposition had not been uniform. In a similar result to this, where Zhang *et al.* [17]had studied carbon deposition on a polished Ni surface by focused ion beam SEM, it was found that non-uniform deposition of carbon had also taken place. As before, where the effects of helium gas (Figure 4.4 (c)) and laboratory air (Figure 4.9 (c)) were investigated, the elemental map of Cr (Figure 4.14(c)) showed that the largest counts of Cr were within the grain boundaries. This observation may have been as a result of the helium which was used as the carrier gas, as investigated earlier (S*ection 4.3.1.1.*).

Unlike in previous studies, here there the formation of carbon nanomaterial in the grain boundaries appeared to have been restricted, as the carbon counts along certain areas in these boundaries had decreased (Figure 4.14(f)). For EPMA images at higher magnification and better clarification of grain boundaries regarding restricted carbon growth in grain boundaries please refer to *Appendix 1*.

Elemental analysis of Mo and Fe respectively (displayed in Figures 4.14(d) and (e)) revealed the least amount of activity regarding the exposure the Hastelloy to these reaction conditions (which were similar to conventional MD conditions). Here both Mo and Fe showed uniform distributions with relatively low counts. In terms of MD, this would have been a surprising result for Fe, as it has been an element which has contributed strongly to the MD mechanism in the past. However, given that Fe only makes up a low percentage of Hastelloy C276 (i.e. 5.4 wt%) by comparison with Ni (58.3 wt%), it appears that its contribution to the carburisation reaction was proportional to it composition in the Hastelloy. Similarly, in the case of Mo (whose percentage composition was similar to that of Cr), very little change regarding the surface of Hastelloy C276 was observed.

Another contributing factor in the prevention of carburisation was the formation of an oxide scale as seen in the elemental map of oxygen (Figure 4.15). Here it was observed that oxygen counts were substantially higher in the grain boundaries as well as in other areas (see the distribution in the bottom right quarter in Figure 4.15). In comparison to the bottom right quarter of Figure 4.15 where the oxygen content was high, the carbon count was relatively low. This demonstrated the resistance of carburisation due to oxygen though oxide formation. This type of scale has been known to show resistance to carburisation and hence the MD mechanism.

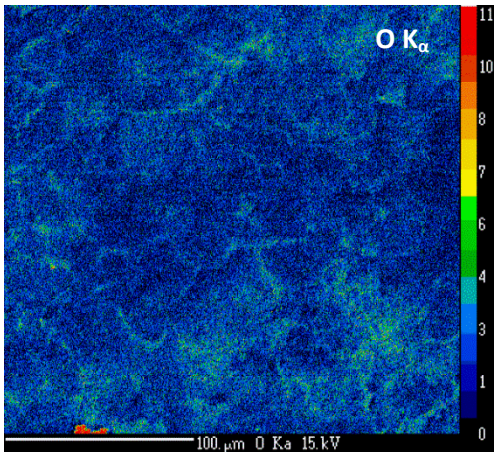


Figure 4.15. Elemental map of a polished Hastelloy C276 surface exposed to the above-mentioned reaction conditions showing the distribution of O K_{α}.

With regard to the grain boundaries where Cr was also abundant (Figure 4.14(c)), Cr oxides have also played a role in defeating carburisation and hence the MD mechanism [11]. Compared to the oxygen maps for helium gas (Figure 4.4 (f)) and laboratory air (Figure 4.9 (f)), when Hastelloy C276 was exposed to these reaction conditions (which were similar to previous types of MD conditions) higher oxygen contents were found in grain boundaries as shown Figure 4.15 where chromium was abundant.

In 1999, Schmid *et al.* [7], considered the possibility of an active role of oxygen during MD conditions in gaseous environments with low steam content. The

concept of the role of oxygen during MD conditions has been studied by Szakalos *et al.* [16] who reported that oxidation of the grain boundaries occurred when MD conditions were induced. It appears that the oxidation of the grain boundaries, as seen in Figure 4.15 (when compared to Figure 4.4 (f) and Figure 4.9 (f) were little or no oxidation was present in the grain boundaries and where no MD conditions had appeared to have been induced) was in agreement with the results of Szakalos *et al.* [16].

4.3.1.3.5. Powder X-ray Diffraction (PXRD)

The formation of oxides after vaporized toluene and gaseous helium were passed over a polished untreated Hastelloy block was investigated using PXRD (Figure 4.16).

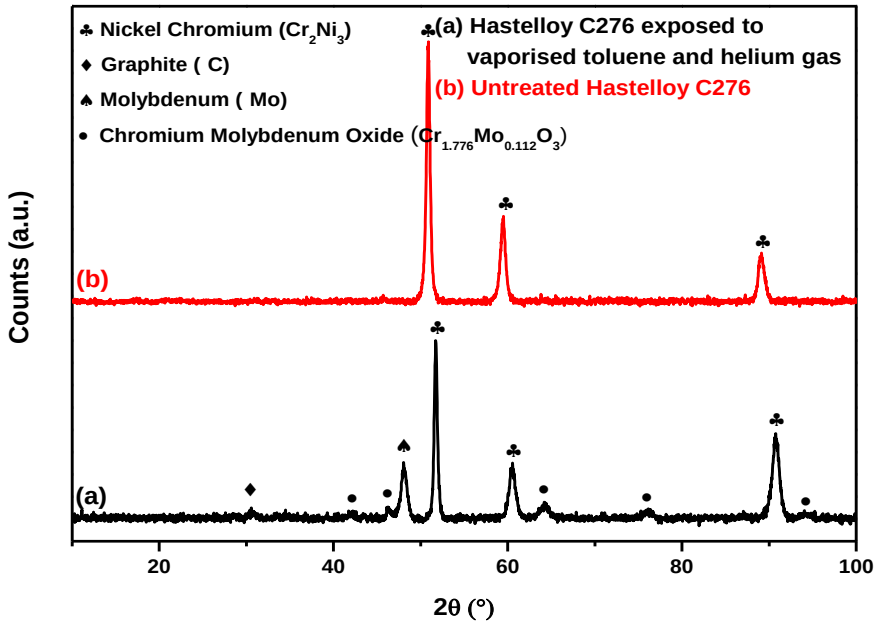


Figure 4.16. PXRD pattern showing the formation of oxides when vaporized toluene and helium gas at 80 mL/min was passed over an untreated polished Hastelloy C276 block at 800 °C.

Here a chromium molybdenum oxide ($Cr_{1.776}Mo_{0.112}O_3$) phase was observed to be the only oxide phase present. This same oxide phase, but in a different stoichiometric ratio ($CrMoO_4$) was also present when the polished untreated Hastelloy blocks were subjected to helium gas at 800 °C (Figure 4.6). A molybdenum peak also appeared in the PXRD pattern and its presence will be further explained further in Chapter 5 *(Section 5.3.6).*

A small graphitic peak was observed at about 2Θ = 30 °. This provided evidence in addition to laser Raman spectroscopy *(Section 4.3.1.3.2.)* that carbonaceous products had formed. However, the number of counts of this peak was very small, since the PXRD instrument used (Bruker D2) measured the bulk of the block and not the surface of the Hastelloy where the carbonaceous material was formed. Further enhancement of this low intensity peak will be shown in Chapter 5 *(Section 5.3.6),* where grazing angle XRD was used to measure the surface of the Hastelloy block.

4.3.1.4. Removal of the carbonaceous material from Hastelloy C276 using laboratory air at 800 °C to determine the effects of metal dusting (MD) using vaporized toluene

4.3.1.4.1. Optical Microscopy (OM)

Some of the blocks which had been exposed to vaporized toluene and gaseous helium were exposed to laboratory air at 800 °C for 1 h to burn off the carbonaceous products which had formed. An OM image of one of these blocks (Figure 4.17) revealed that under such conditions, the carbonaceous materials were removed and the surface was irregular. Here areas that appeared black and grey in colour seemed to be significantly more rough than the surfaces which were exposed to gaseous helium (Figure 4.1(a)) and laboratory air (Figure 4.7 (a)) at 800 °C.

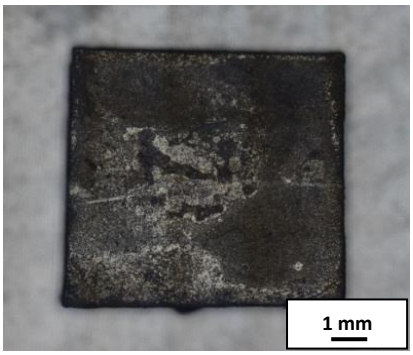


Figure 4.17. An OM image of a Hastelloy C276 block which had been heat treated at 800 °C for 1 h in laboratory air after having being carburized in vaporized toluene with helium as the carrier gas at 800 °C.

The Hastelloy block still appeared to be black in most regions even after being heat treated to 800 °C for 1 h in laboratory air and it seemed that not all of the carbonaceous products may have been burnt off.

4.3.1.4.2. Scanning Electron Microscopy (SEM)

Further investigation under SEM revealed that there was no sign of a graphite layer or carbon nanofilaments on the surface of the Hastelloy (Figure 4.18(a)). This meant that all carbonaceous materials were indeed burnt off after 1 hour in laboratory air at 800 °C and the black colour was due to something else. A closer inspection of Figure 4.18(a), demarcated in red in Figure 4.18(b), showed that a piece of the surface of Hastelloy C276 had been removed. This observation confirmed that MD had taken place and that a pit had evolved on the surface of the Hastelloy.

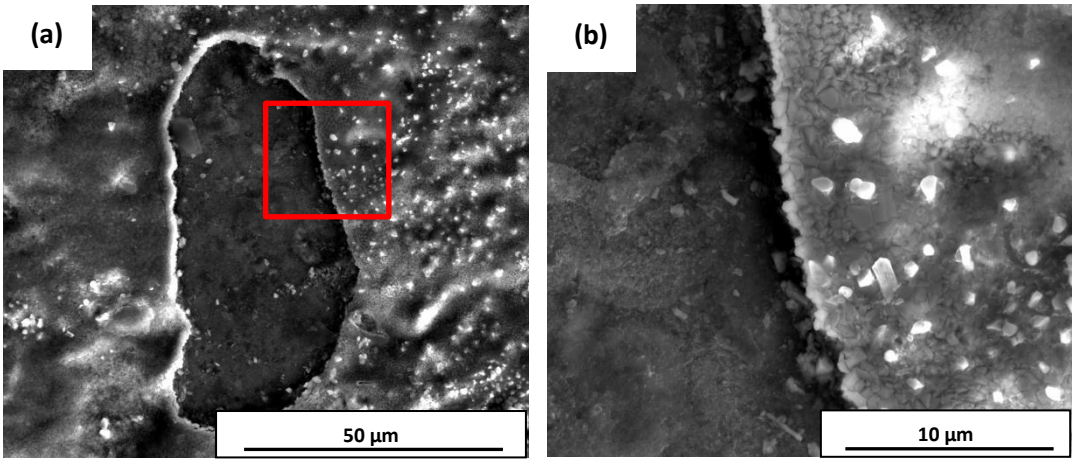


Figure 4.18. SEM micrographs showing: **(a)** A MD pit which had formed on the surface of a polished Hastelloy C276 block due to toluene after the carbonaceous products had been burnt off, **(b)** A magnified section of (**a**).

The region around the pit in Figures 4.18 (a) and (b) may have been interpreted by some as an oxide scale. However, a few reasons have been proposed below to strongly suggest that this was indeed a pit caused by MD and not an oxide scale that sat above the surface of Hastelloy C276. The first is that the conditions in these experiments were not conducive to form an oxide scale of this magnitude for two reasons: (1) the oxygen content in the helium gas that was used was very low, i.e. oxygen was a contaminant in the low ppm range as previously mentioned and (2) the duration of exposure to air in these experiments, even at 800 °C, was far too short for such scales to have formed. For instance, Chen *et al.* [25] have shown that adherent Cr oxide scales were only grown on commercial Ni-based alloys after ***1000 hs*** at 750 °C. In these experiments the exposure time was only 1 hour. The second is that further evidence to establish the nature of the change that had taken place on the surface of the Hastelloy, was gathered though EPMA analyses. These are shown in the section which follows (S*ection 4.3.1.4.3*).

4.3.1.4.3. Electron Probe Microanalysis (EPMA)

Elemental maps of Ni, Cr, Mo and Fe on the surface of the Hastelloy were obtained after the carbonaceous products had been burnt off (Figure 4.19). The

SEM micrograph of the area on which elemental mapping was executed is shown in Figure 4.19(a), which was similar to that of the SEM micrograph in Figure 4.18(a) that was taken on a high resolution SEM (**FEI Nova Nanolab 600 FEG-SEM**).

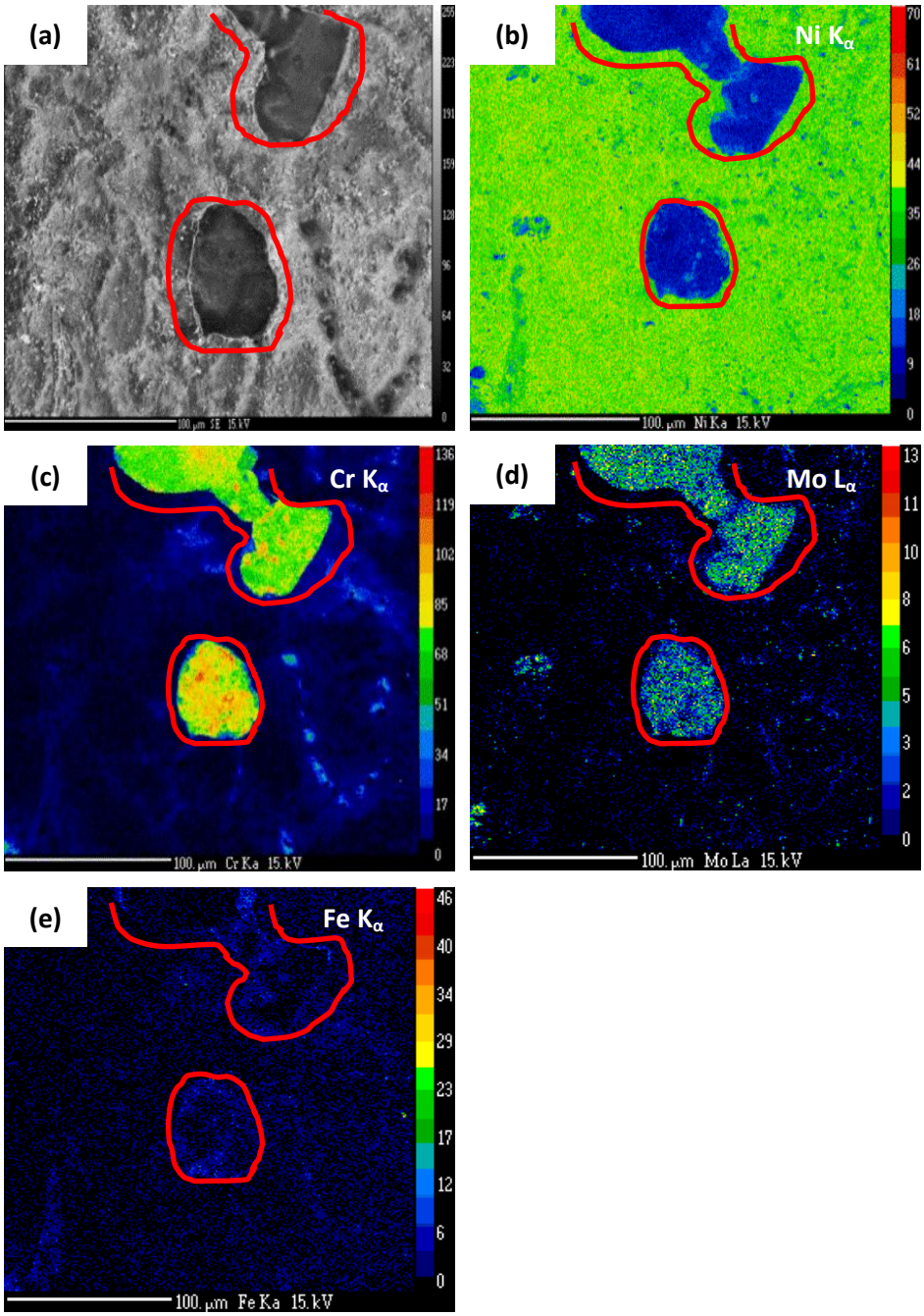


Figure 4.19. Elemental Maps of a carburised Hastelloy C276 surface, after the carbonaceous products had been burnt off, showing: **(a)** a SEM micrograph of the mapped area, **(b)** Ni K_α **(c.)** Cr K_α, **(d)** Mo L_α, and **(e)** Fe K_α.

Here it was noted that contrary to the Hastelloy composition, Ni counts made up the minority of the composition in the pit (Figure 4.19(b) - see marked out areas in red) while Cr (Figure 4.19(c)) and Mo (Figure 4.19(d)) made up higher counts than expected in the pit (see marked out areas in red). Apart from the pitted areas, the Ni content on the surface was proportionately high as compared to Cr. Fe, due to its low percentage composition, possessed distinctively low counts (except for a few areas were Fe was agglomerated (Figure 4.19(e)).

In order to settle the question of whether the feature observed in Figure 4.18 (a.) was a pit or an oxide scale, oxygen was mapped in a pitted area similar to those shown in Figures 4.18(a) and 4.19 (a). The SEM micrograph on which oxygen was mapped is shown in Figure 4.20(a). The oxygen map (O K_α) is shown in Figure 4.20(b) *(see Appendix 2 for Ni K_α, Cr K_α, Fe K_α and Mo K_α maps).*

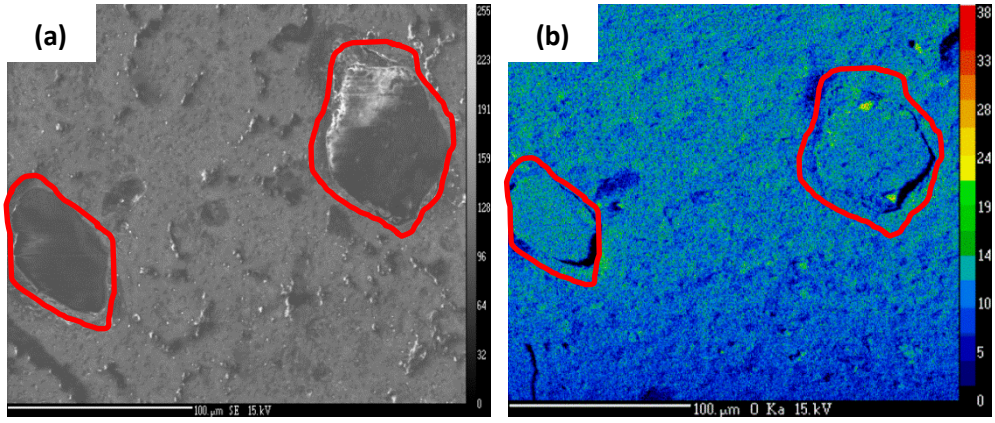


Figure 4.20. Elemental Maps of a polished Hastelloy C276 surface exposed to MD conditions after carbon had been burnt off, showing: **(a)** A SEM micrograph of the mapped area and **(b)** O K_α.

Here it was observed that the oxygen content (Figure 4.20) was low and uniform thoughout the surface and the pits. However, a higher quantity of Ni was distributed on the surface than in the pits (Figure 4.19(b.)). If this had indeed been and oxide scale, then a higher oxygen count would have been expected to have been observed on the surface and a lower one in the pit. This together with the

other reasons suggested previously confirmed that, the feature observed in Figure 4.18 (a.) was a pit and not an oxide scale.

4.3.1.4.4. Powder X-ray Diffraction (PXRD)

PXRD was performed on the Hastelloy after the carbonaceous material was burnt off its surface in laboratory air at 800 °C (Figure 4.21). Here a very similar pattern was noted compared to that which was observed when a polished untreated Hastelloy block was exposed to laboratory air at 800 °C (Figure 4.10). This suggested that after the carbonaceous material had been burnt off, perhaps in a short period of time, small quantities of the same types of oxides ($NiCr_2O_4$ and ($Ni(MoO_4)$) had been formed as those when the Hastelloy had been exposed to laboratory air at 800 °C.

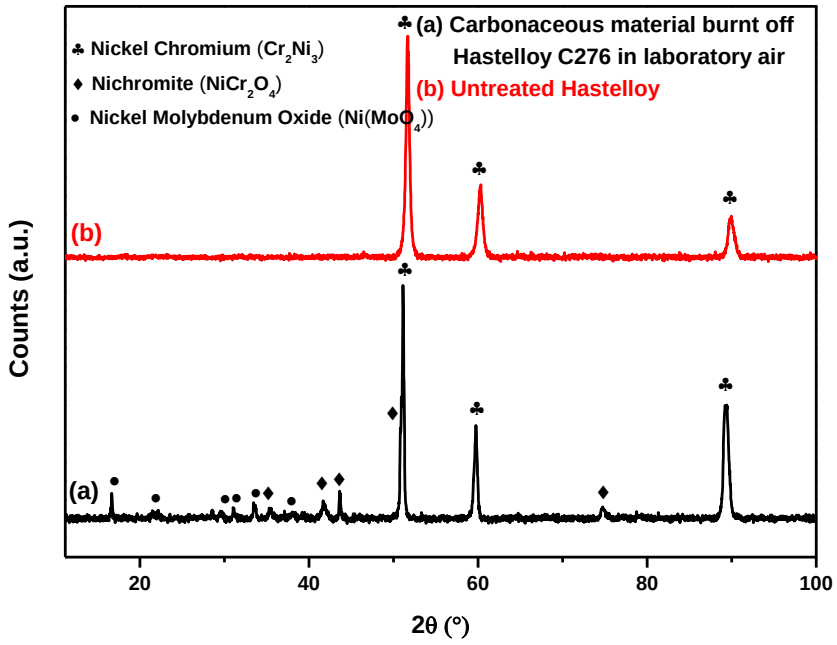


Figure 4.21. PXRD pattern showing Hastelloy C276: **(a)** Exposed to vaporised toluene and gaseous helium at 800 °C and then burnt in laboratory air at 800 °C to remove carbonaceous materials and **(b)** Untreated (i.e. in its pristine polished form).

4.4. Conclusions

The results have shown that helium (which was employed as carrier gas) and laboratory air (which was used to burn off carbonaceous material) did not cause any pitting (i.e. MD) on the surface of Hastelloy C276, but only revealed pre-existing grain boundaries. However, when vaporised toluene and gaseous helium was passed over the Hastelloy block at 800 °C, carbonaceous material was formed and when this was burnt off in laboratory air at 800 °C it revealed that pits had formed on the surface of the Hastelloy. These pits were exclusively as a consequence of the carburisation of toluene (the liquid hydrocarbon source), since the possibility that helium gas and laboratory air had caused these observations had been ruled out when separate experiments with helium and laboratory air had been carried out.

When utilising EPMA to determine the elemental distribution in the surface of an untreated Hastelloy C276 block, the data revealed that the elements therein were distributed evenly over the surface. However, when exposed to helium gas and an air environment in the laboratory, disorder in the distribution of metallic elements had been introduced. The redistribution of these elements, especially Cr, suggested evidence of sensitization which may have led to intergranular attack or intergranular corrosion cracking.

In the case where Hastelloy blocks were exposed to toluene at 800 °C, this revealed that Ni had remained dominant on the surface of Hastelloy C276, but was deficient in the pits that were observed on the surface. However, the opposite effect was noted for Cr and Mo where the majority of these elements was observed in the pits and the minority on the surface.

Where oxidation was concerned, it was noted that very little oxidation had taken place on Hastelloy C276 in the form that it was supplied. This was expected as Hastelloy C276 is meant to be a highly corrosion resistant alloy. When Hastelloy C276 was treated with helium gas and laboratory air, the oxidation of the two

Hastelloy C276 blocks were observed to be the same (except for the higher intensity of oxides on the surface of the blocks in laboratory air) i.e. the majority of the oxygen was observed on the surface and a minority in the grain boundaries. However, when Hastelloy C276 was exposed to toluene i.e. MD conditions, oxygen was found to be uniformly distributed on the surface of the Hastelloy blocks.

Results presented in this chapter showed a great deal of similarity to those in literature regarding MD, which had occurred in syngas environments were limited data regarding liquid hydrocarbons and MD have been reported. It can therefore be concluded, from results throughout this study, that the highly corrosion resistant Hastelloy C276 was demonstrated to have been susceptible to MD at 800 °C when exposed to toluene (a liquid hydrocarbon source).

4.5. References

1. J. Dampc, Z. Grzesik, and J. Hucińska, *Metal dusting in CCR platforming unit.* Materials and corrosion, 2009. **60**(3): pp. 211-217.
2. M. Szkodo and G. Gajowiec, *Studies of the mechanism of metal dusting of 10CrMo9-10 steel after 10 years of operation in the semi-regenerative catalytic reformer.* Corrosion Science, 2016. **102**: pp. 279-290.
3. G.A. Slabbert, F.M.L. Mulaudzi, L.A. Cornish, M.J. Papo, V. Morudu and J Zhang, *The effect of the matrix structure on the metal dusting rate in hydrocarbon environments.* Journal of the Southern African Institute of Mining and Metallurgy, 2013. **113**(2): pp. 81-90.
4. S. Strauss and H.J. Grabke, *Role of alloying elements in steels on metal dusting.* Materials and corrosion, 1998. **49**(5): pp. 321-327.
5. H.J. Grabke, R. Krajak, and J.N. Paz, *On the mechanism of catastrophic carburization:'metal dusting'.* Corrosion Science, 1993. **35**(5): pp. 1141-1150.
6. J.N. Paz and H.J. Grabke, *Metal dusting.* Oxidation of metals, 1993. **39**(5-6): pp. 437-456.
7. B. Schmid, Ø. Grong, and R. Ødegård, *Coke formation in metal dusting experiments.* Materials and corrosion, 1999. **50**(11): p. 647-653.
8. H.J. Grabke, *Thermodynamics, mechanisms and kinetics of metal dusting.* Materials and corrosion, 1998. **49**(5): pp. 303-308.
9. Z. Zeng and K. Natesan, *Relationship of carbon crystallization to the metal-dusting mechanism of nickel.* Chemistry of materials, 2003. **15**(4): pp. 872-878.
10. Z. Zeng and K. Natesan, *Relationship between the growth of carbon nanofilaments and metal dusting corrosion.* Chemistry of materials, 2005. **17**(14): pp. 3794-3801.
11. D.J. Young, J. Zhang, C. Geers and M. Schütze, *Recent advances in understanding metal dusting: A review.* Materials and corrosion, 2011. **62**(1): p. 7-28.
12. J. Zhang, D.M.I. Cole, and D.J. Young, *Alloying with copper to reduce metal dusting of nickel.* Materials and corrosion, 2005. **56**(11): pp. 756-764.
13. D.J. Young and J. Zhang, *Metal dusting: Catastrophic corrosion by carbon.* JOM, 2012. **64**(12): pp. 1461-1469.
14. H.J. Grabke, *Nickel-based alloys in carbonaceous gases.* Corrosion, 2000. **56**(8): pp. 801-808.
15. J. Zhang, P. Munroe, and D.J. Young, *Microprocesses in nickel accompanying metal dusting.* Acta Materialia, 2008. **56**(1): pp. 68-77.
16. P. Szakalos, R. Pettersson, and S. Hertzman, *An active corrosion mechanism for metal dusting on 304L stainless steel.* Corrosion Science, 2002. **44**(10): pp. 2253-2270.
17. J Zhang. and D.J. Young, *Kinetics and mechanisms of nickel metal dusting I. Kinetics and morphology.* Corrosion Science, 2007. **49**(3): pp. 1496-1512.
18. P. Szakalos, *Mechanisms and driving forces of metal dusting.* Materials and corrosion, 2003. **54**(10): pp. 752-762.
19. C. Tedmon, D. Vermilyea, and J. Rosolowski, *Intergranular corrosion of austenitic stainless steel.* Journal of The Electrochemical Society, 1971. **118**(2): pp. 192-202.
20. Y.F. Yin and R.G. Faulkner, *Model predictions of grain boundary chromium depletion in Inconel 690.* Corrosion science, 2007. **49**(5): pp. 2177-2197.

21. W.E. Mayo, *Predicting IGSCC/IGA susceptibility of Ni-Cr-Fe alloys by modeling of grain boundary chromium depletion.* Materials Science and Engineering: A, 1997. **232**(1): pp. 129-139.
22. *HASTELLOY® C-276 alloy Information*. 2001 [cited 2016 8 March]; Available from: http://www.haynesintl.com/HASTELLOYC276Alloy/HASTELLOYC276AlloyPF.htm.
23. D. Wasnik, V. Kain, I. Samajdar, B. Verlinden and P. De, *Resistance to sensitization and intergranular corrosion though extreme randomization of grain boundaries.* Acta Materialia, 2002. **50**(18): pp. 4587-4601.
24. A.C. Ferrari and J. Robertson, *Interpretation of Raman spectra of disordered and amorphous carbon.* Physical review B, 2000. **61**(20): p. 14095.
25. J. Chen, P. Rogers, and J. Little, *Oxidation behavior of several chomia-forming commercial nickel-base superalloys.* Oxidation of Metals, 1997. **47**(5-6): pp. 381-410.

5 SYNTHESIS AND CHARACTERISATION OF CARBON NANOFILAMENTS VIA THE METAL DUSTING (MD) MECHANISM

5.1. Introduction

It is widely known that CNTs were first observed by Iijima in 1991 [1-3]. Since electron microscopy had not been fully developed in the early part of the 20th century it is certain that CNTs had been around prior to this observation, as techniques like carbon combustion or vapour deposition in which CNTs are known to be synthesised were developed much earlier than 1991 [3]. Due to their remarkable mechanical and physical properties CNTs have gained a great deal of consideration with a wide variety of applications ranging from field emission sources to hydrogen storage [3]. With regard to the synthesis of CNTs, thee methods are well known namely: arc-discharge, laser ablation and catalytic chemical vapour deposition (CCVD) [2, 4].

With the increasing quantity of publications in the area of CNT synthesis, the MD mechanism in the synthesis of CNTs is becoming more and more popular for a variety of reasons. One of the primary ones is that the synthesis of CNTs via the MD mechanism is relatively similar to that of the CCVD method. As described by Kumar *et al.* [5], CCVD generally requires a hydrocarbon vapour coming into contact with hot metal 'nanoparticles' [5]. In the case of MD, metal nanoparticles are dislodged from an alloy due to the deposition, dissolution, diffusion, penetration and continuous precipitation of carbon into a carbon filament (as described in more detail in Chapter 2) [6].

More recently, contrary to research regarding the mechanisms and prevention of MD, researchers have been seeking new ways to exploit MD to synthesize CNTs

for applicative, commercialisation and research purposes. Chang *et al.* [2] have successively synthesized CNTs via the MD approach using stainless steel 304L, with CO-CO_2 as the carbon sources, after several post-treatments for a hydrogen storage application. On the other hand, Ghorbani *et al.* [3], have shown that a high yield of CNTs could be obtained via MD by the optimisation of reaction conditions. These reaction conditions were optimised by thermal cycling to accelerate Cr depletion, which accelerated the rate of MD [3]. Here CNT growth increased by between 700 – 800%[3]. Another successful attempt to enhance the yield of CNT growth via MD has been presented by Pattinson *et al.*, where reconstruction of stainless steel 316 was induced by oxygen [7]. In that case a 70-fold increase in the yield of CNTs was reported [7].

Research centred on the synthesis and characterisation of CNTs via MD also includes the work of Hashempour *et al.* where the growth of CNTs/CNFs was observed to have taken place on stainless steel 316 with ethylene as a hydrocarbon source [8]. Here it was demonstrated that growth of CNTs/CNFs took place by two mechanisms. The first of these was a tip-growth mechanism i.e. where metal nanoparticles (particularly iron) dissociated from the surface of stainless steel 316 [8]. In the second, CNTs/CNFs were found to have grown by a base growth mechanism, which resembled MD, but in these cases their growth was catalysed by nanosized hills on the surfaces of the stainless steel 316 [8]. In addition it was found that the sizes of the nano-hills determined whether CNTs or CNFs were formed [8].

In this chapter, the synthesis and characteristics of CNTs/CNFs were investigated via the MD mechanism using a Ni-based (Hastelloy C276) alloy as opposed to the commonly used stainless steel Fe-based alloys previously described. The reaction rates and the activation energy of toluene on Hastelloy C276 to form carbon nanomaterials were determined. Relationships between the CNTs/CNFs formation and the MD mechanism were formed using a variety of characterisation techniques.

5.2. Experimental Procedures

MD experiments to synthesize carbon nanofilaments were carried out in the CVD reactor that was shown in Figure 3.1 (Chapter 3). In prior experiments (*Appendix 3*) results that were obtained showed that the yield of carbon nanofilaments that were synthesized on unpolished Hastelloy C276 surfaces was higher than when compared to polished surfaces as seen in Chapter 4 (Figure 4.13). These as-supplied unpolished blocks were found to have rough surfaces which exhibited pits. Hence, as opposed to Chapter 4 where polished Hastelloy C276 blocks were studied, in this Chapter ***unpolished*** Hastelloy C276 blocks (Figure 5.1) were used to synthesize carbon nanofilaments.

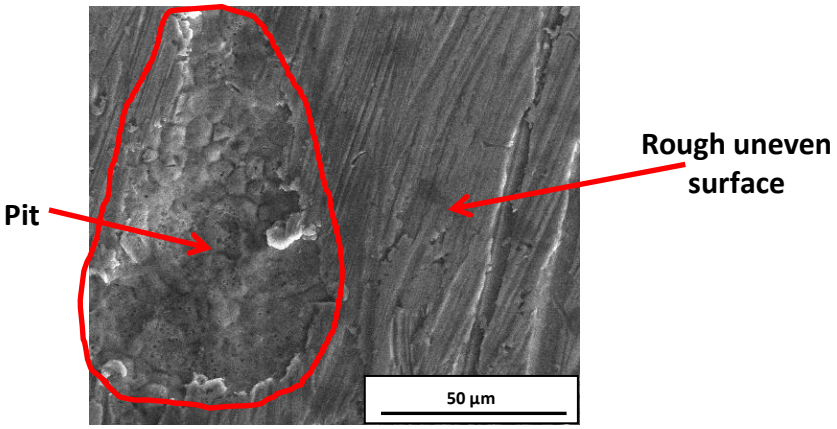


Figure 5.1. SEM image of an unpolished Hastelloy C276 block which showed a pit (left hand arrow with outline) with surface roughness (right hand arrow).

The carbon nanofilaments that were formed under these conditions were examined under SEM directly from the surface of Hastelloy C276. TEM analyses of the carbon nanofilaments removed from the surfaces of these blocks were performed to determine if they were either CNTs or CNFs and to establish if they contained metal particles embedded in their structures (a sign that would have confirmed that MD had occurred).

Initially the temperatures of the reactions were varied between 700 – 900 °C for the purposes of determining the effect of temperature on the synthesis of carbon nanofilaments. A study was then conducted at a fixed temperature (800 °C) to establish the effect of flow rate (i.e. 80, 160 and 240 mL/min) at various durations of reaction times (10, 15, 30, 45 60, 120, 240 min) on the diameter of the nanofilaments that were formed. TEM of these materials was then performed to establish if these nanofilaments were comprised of CNFs, CNTs or a mixture of the two.

Thereafter a kinetics study was performed in order to establish the order of the reaction in the reaction rate with respect to toluene on Hastelloy C276. Using the reaction order and the rates determined at various temperatures (800 °C, 850 °C and 900 °C) the activation energy for the decomposition of toluene on Hastelloy C276 was calculated.

A bulk PXRD method (**Bruker D2 phaser**) was then used to identify the phases of Hastelloy C276 as well as to establish the presence of graphite associated with the carbon nanofilaments. Since this proved inconclusive in identifying the graphite, grazing incidence XRD was used. Here a **Bruker D8 Discover** with Cu radiation was used for this measurement. The carbon nanofilaments formed in these studies were then analysed by laser Raman spectroscopy to identify their crystallinities.

Finally OM, SEM and EPMA analyses were performed to determine if shaped carbon nanomaterials of other kinds had formed during these reactions and if so what the carbon densities of these were relative to the carbon nanofilaments which had formed.

5.3. Results & Discussion

5.3.1. Temperature Study

A preliminary study was performed at a fixed flow rate (80 mL/min) at temperatures of: 700, 800 and 900 °C for 240 min with toluene on Hastelloy C276 in order to evaluate the formation of carbon nanofilaments on the surface of the Hastelloy C276 (Figure 5.2).

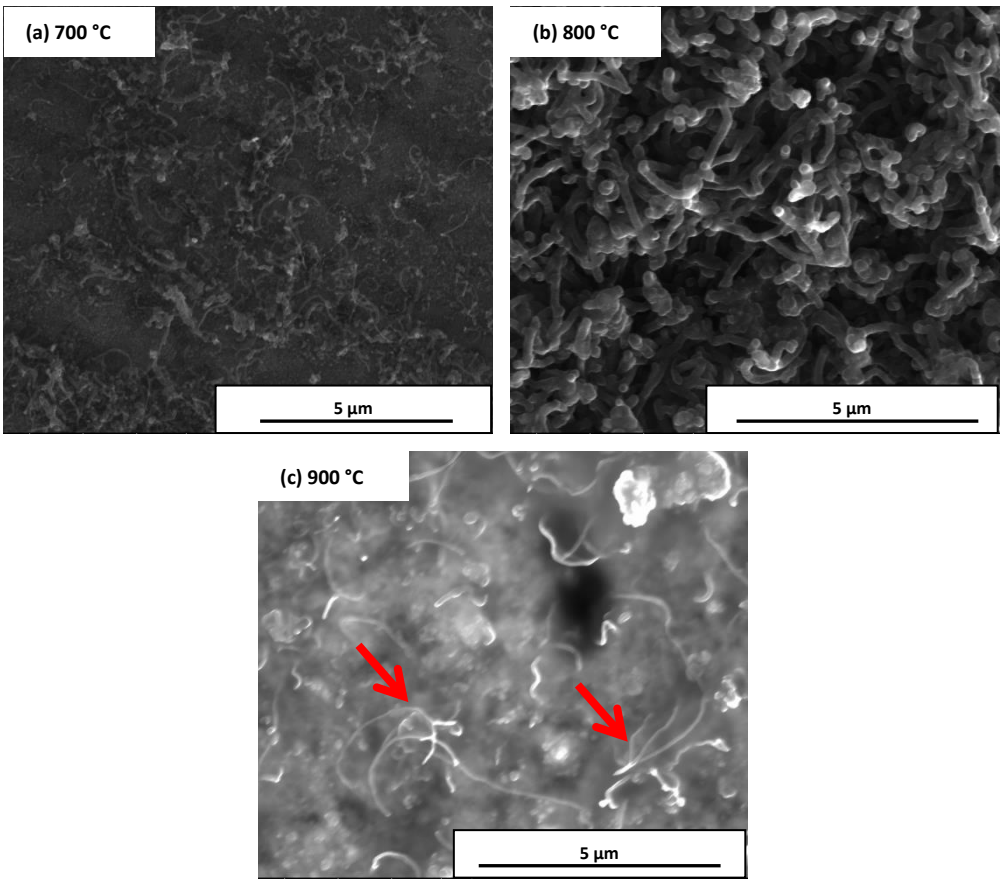


Figure 5.2. SEM micrographs of carbon nanofilaments synthesized on Hastelloy C276 at: **(a)** 700 °C, **(b)** 800 °C and **(c)** 900 °C at 80 mL/min for 4 h.

At 700 °C (Figure 5.2 (a)), the surface coverage of carbon nanofilaments, that formed on a representative Hastelloy C276 block, was relatively low by

comparison with that of 800 °C and 900 °C (Figure 5.2 (b) and (c)). On the other hand a very high agglomeration of carbon nanofilaments, some seen protruding off the Hastelloy surface (see arrows in Figure 5.2 (c)), was observed on a representative block at 900 °C. Carbon nanofilaments of an intermediate surface coverage between that of 700 °C and 900 °C were observed to be uniformly distributed over the surface of a representative Hastelloy C276 block at 800 °C. When the yield of carbon on Hastelloy C276 was plotted versus temperature a linear increase was observed (Figure 5.3). This trend was consistent with that which was observed by Zhang *et al.* [9] who showed that increased reaction temperature: (1) behaved as the driving force of the reaction by having increased gas phase supersaturation of carbon (and hence increased rate of carbon deposition like in this present study), and (2) utilised the energy difference to increase the rates of the various processes required in the MD process itself.

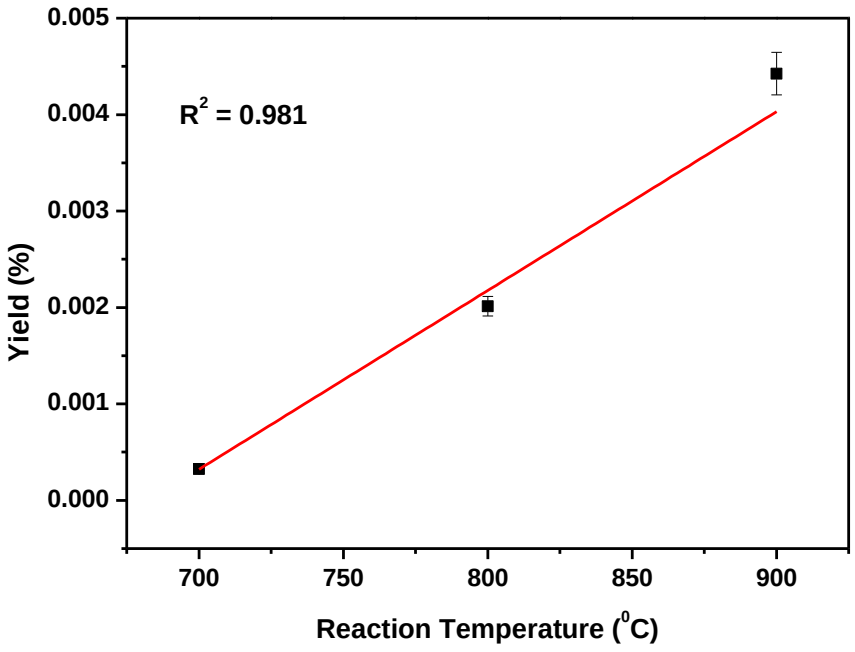


Figure 5.3. A plot of effect of the reaction temperature on the carbon yield on Hastelloy C276 at 80 mL/min during a 240 min reaction.

Based upon the results obtained from this study, it was concluded that the best temperature to more fully characterise the carbon nanofilaments that formed was 800 °C. This conclusion was arrived at because the carbon nanofilaments formed at this temperature were: (1) of intermediate surface coverage on the Hastelloy C276 blocks which was easy to observe by OM and SEM, (2) of sufficient quantity to analyse as opposed to at 700 °C, (3) less agglomerated and hence once again more easy to observe by OM and SEM than at 900 °C. For all these reasons the proceeding study, where the effect of the flow rate in association with reaction time were to be investigated, was conducted at 800 °C.

5.3.2. Flow rate and reaction time study

Reactions were conducted at 800°C for durations ranging from 10 min to 240 min at 80 mL/min (Figure 5.4), 160 mL/min (Figure 5.5) and 240 mL/min (Figure 5.6). In all cases carbon nanofilaments were observed to have formed.

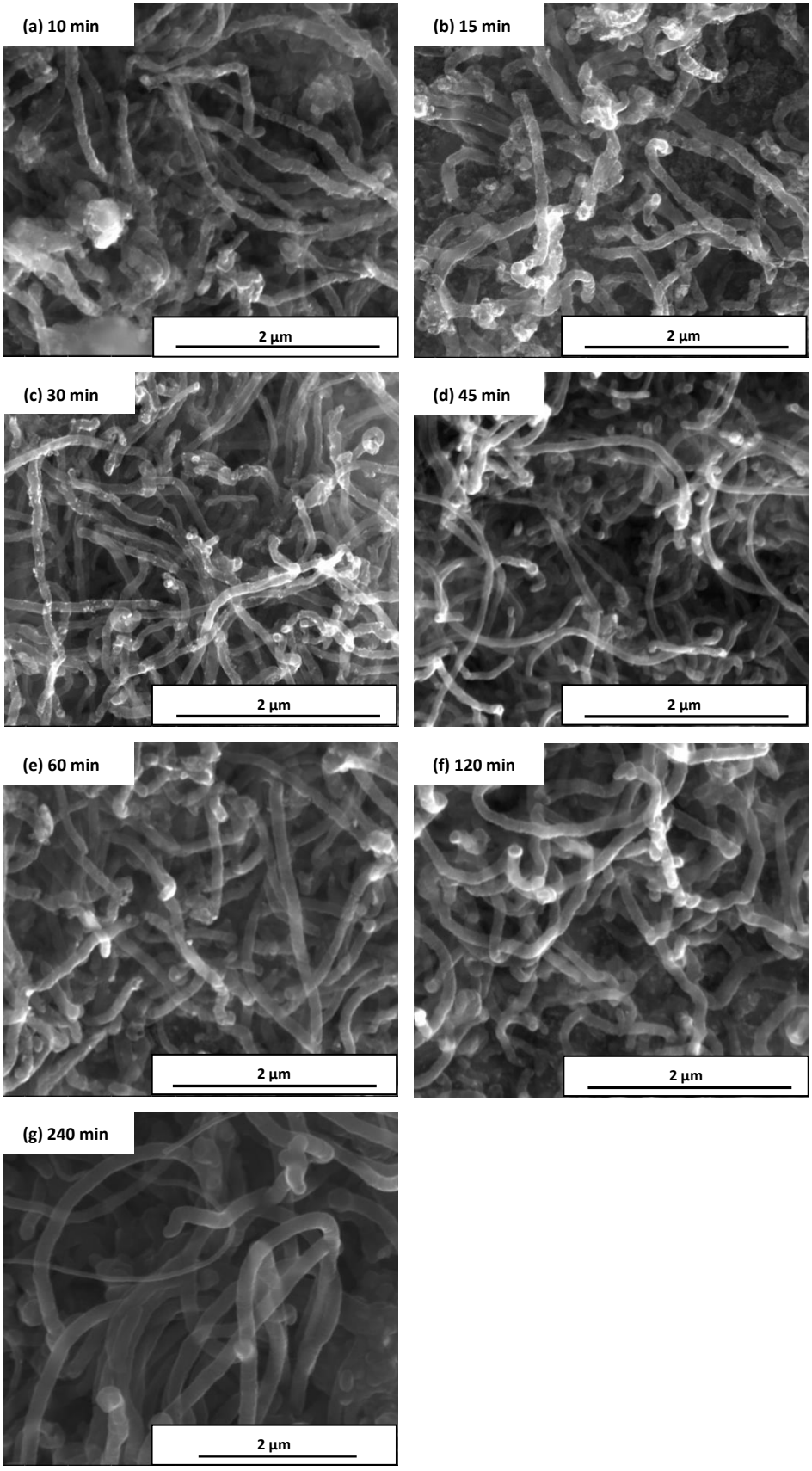


Figure 5.4. SEM images of carbon nanofilaments synthesized at 80 mL/min with varying durations of reaction times: **(a)** 10 min, **(b)** 15 min, **(c)** 30 min, **(d)** 45 min, **(e)** 60 min, **(f)** 120 min and **(g)** 240 min.

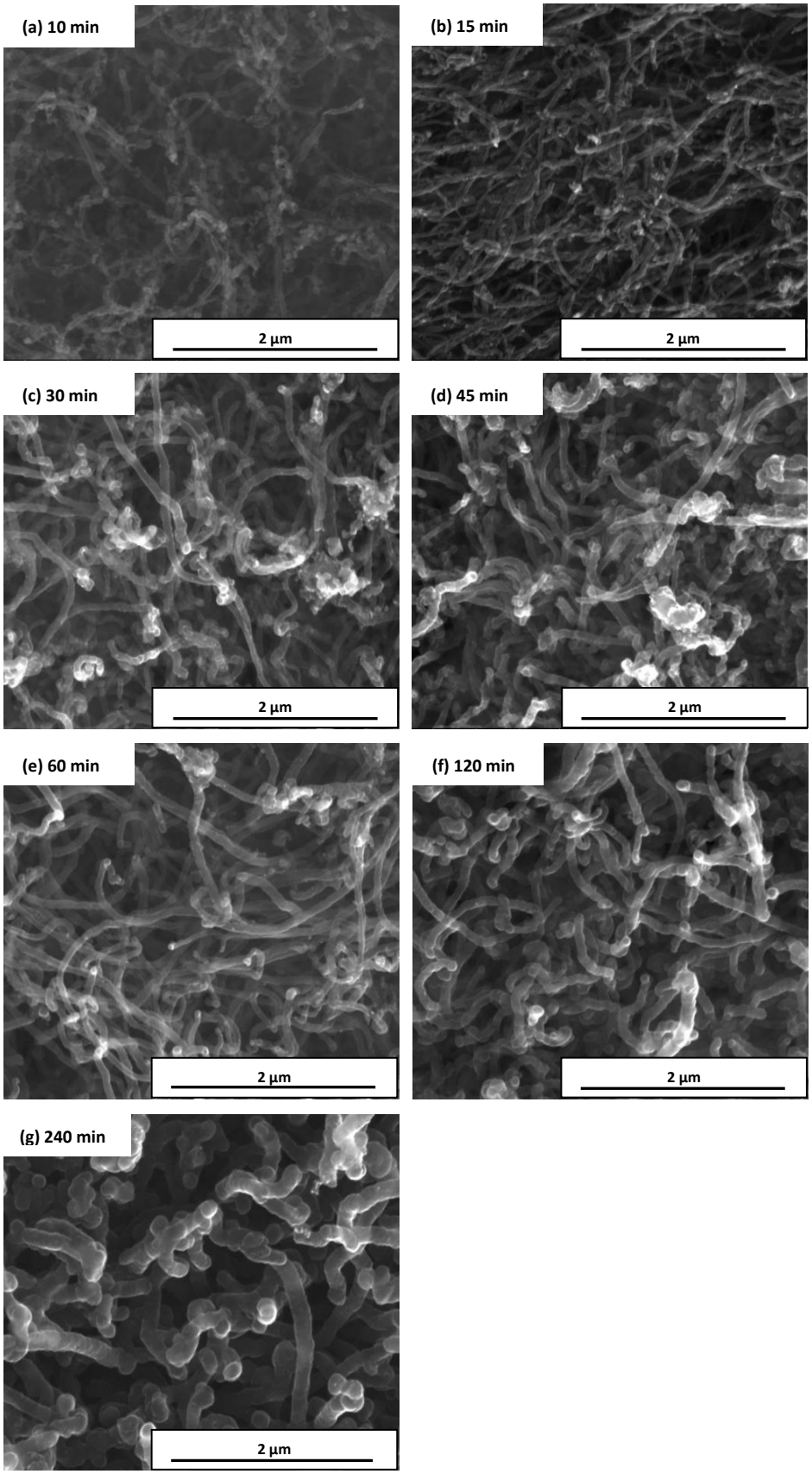


Figure 5.5. SEM images of carbon nanofilaments synthesized at 160 mL/min with varying durations of reaction times: **(a)** 10 min, **(b)** 15 min, **(c)** 30 min, **(d)** 45 min, **(e)** 60 min, **(f)** 120 min and **(g)** 240 min.

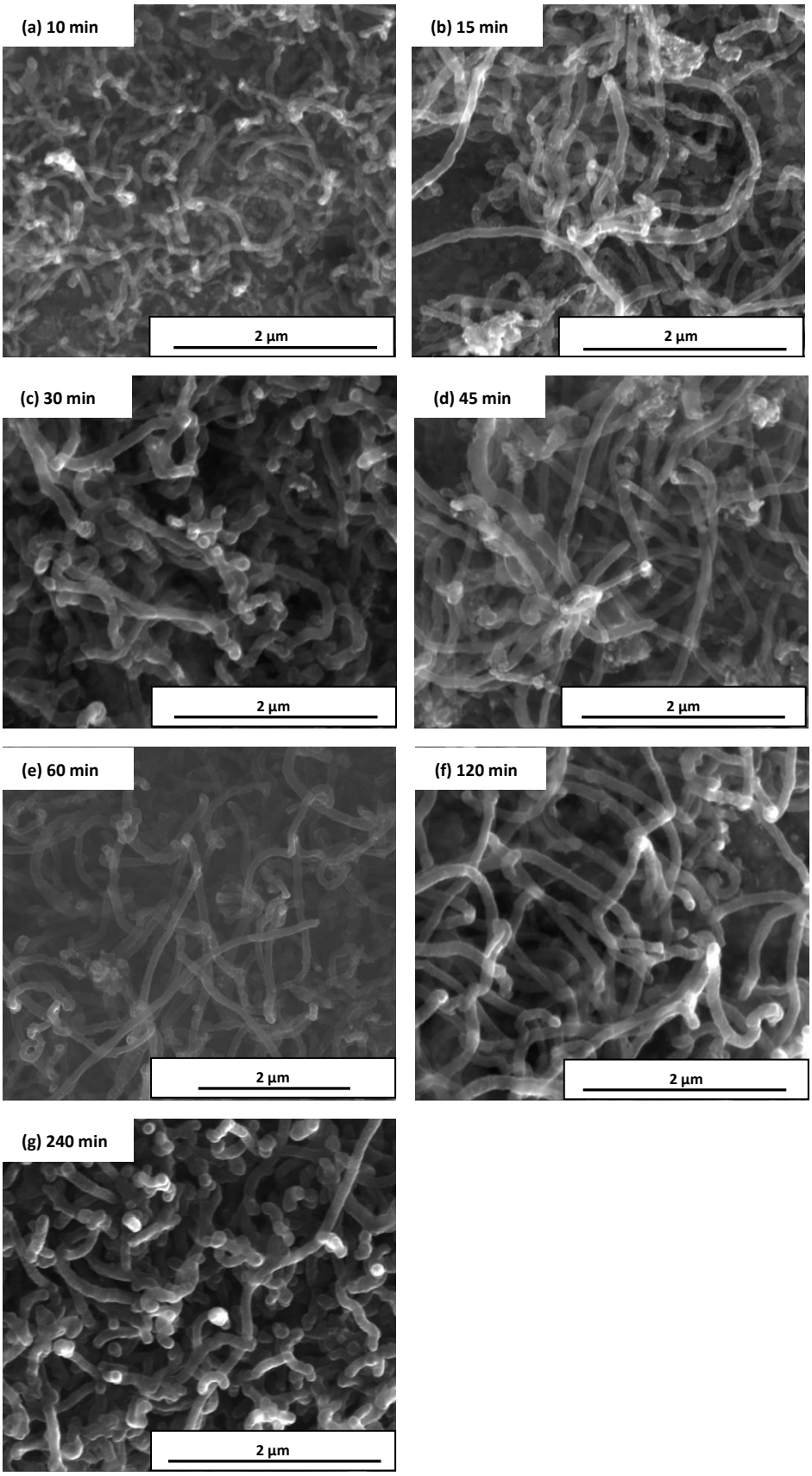


Figure 5.6. SEM images of carbon nanofilaments synthesized at 240 mL/min with varying durations of reaction times: **(a)** 10 min, **(b)** 15 min, **(c)** 30 min, **(d)** 45 min, **(e)** 60 min, **(f)** 120 min and **(g)** 240 min.

SEM observations revealed that the carbon nanofilaments that were formed were found predominantly on the rough surfaces of the Hastelloy C276 blocks as opposed to the pits (shown in Figure 5.1). Likewise, based on observations in the SEM micrographs, it was noted that carbon nanofilaments were relatively irregularly or poorly formed (*refer to Appendix 4 for TEM images of poorly formed carbon nanofilament images*) after reaction durations of 10 and 15 min, as compared to those at higher reaction durations across the flow rate range that was investigated. For instance, after a reaction duration of 30 min, an improvement in the form of the carbon nanofilaments was observed, especially for flowrates of 160 and 240 mL/min. Carbon nanofilaments that were formed at reaction durations longer than 30 min, across the flow rate range investigated, all appeared fully formed and of high quality. Thus it was concluded that longer reaction durations were required for high quality carbon nanofilaments to form via the MD mechanism.

An investigation into the effect of flow rate and reaction duration on the average nanofilament diameters was then conducted. Here the diameters of 300 nanofilaments per reaction duration and flow rate were measured, averaged and then plotted (*see Appendix 5 for histograms*). The results of this investigation are presented in Table 5.1.

Table 5.1. Average filament diameter at different flow rates.

Reaction Time (min)	Average Filament Diameter (nm)		
	80 mL/min	160 mL/min	240 mL/min
10	76.7 (± 1.2)	69.8 (± 4.2)	59.1 (± 2.5)
15	79.1 (± 4.1)	77.6 (± 3.7)	62.4 (± 3.9)
30	81.1 (± 3.6)	98.4 (± 2.0)	65.0 (± 3.1)
45	80.1 (± 1.9)	102.6 (± 3.2)	82.0 (± 2.4)
60	96.1 (± 6.7)	105.2 (± 5.3)	77.7 (± 4.8)
120	112.8 (± 2.3)	117.5 (± 1.2)	103.8 (± 3.0)
240	187.1 (± 6.1)	170.0 (± 5.9)	158.1 (± 6.3)

The results in Table 5.1, when plotted (Figure 5.7), revealed that the average diameters of these carbon nanofilaments generally increased with increased duration of reaction across a defined flow rate. This same kind of increase in CNF diameter has been reported by Jarrah *et al.* [10] when a Ni-foam catalyst (reduced in 20 % hydrogen in nitrogen gas) and ethylene gas (carbon source) at 700 °C was used. It may be regarded that with the increase in the duration of reaction, the deposition of carbon increased because the residential time of the vaporised toluene spent in the reactor (quartz tube furnace) increased and with that increased deposition the diameter of the carbon nanofilament increased. This observation has been confirmed by Mhalanga [11] in a study where a Fe-Co (metals also susceptible to MD) catalyst supported on calcium carbonate ($CaCO_3$) was used to synthesize multi-walled CNTs at 700 °C in which an increase in diameter of the outer walls of a multi-walled CNTs was observed.

It was noted that as the flow rate increased the average nanofilament diameter generally (with some inconsistencies between 30-60 mins for the 160 mL/min) decreased (Figure 5.7). In this case, the increased average filament diameter at a lower flow rate may have been attributed to the fact that there was more time for the vaporised to toluene to further deposit on the CNTs/CNFs already formed on the surface of the Hastelloy, whereas at higher flow rates (e.g. 240 mL/min) there was less time for the vaporised toluene to interact with carbon already deposited.

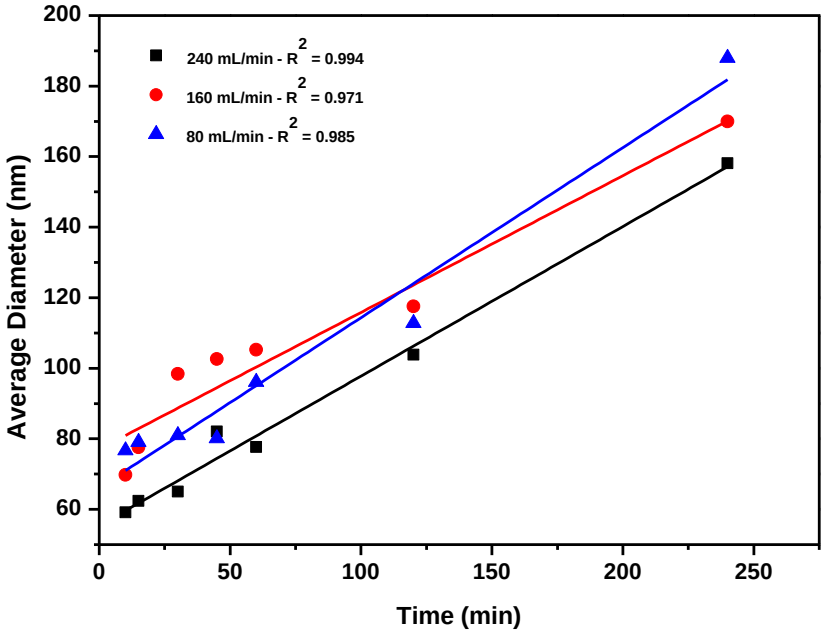


Figure 5.7. A plot of the effects of flow rate and reaction duration on the average diameter of carbon nanofilaments that were synthesized at 800 °C.

5.3.3. TEM analyses of the Carbon Nanofilaments synthesized

Up until now the filamentous carbon material synthesized on Hastelloy C276 have been referred to as carbon nanofilaments and have not been identified as either CNTs or CNFs. TEM analyses of these nanofilaments were conducted to establish, which of these (if any) may have dominated under the various reaction conditions. TEM micrographs (Figure 5.8) revealed that these nanofilamentous materials that formed on the surfaces of Hastelloy C276, regardless of the flow rate and reaction duration, were composed of an ensemble of CNFs (Figure 5.8 (a), (d), (e) and (f)) and CNTs (Figures 5.8 (b) and (c)).

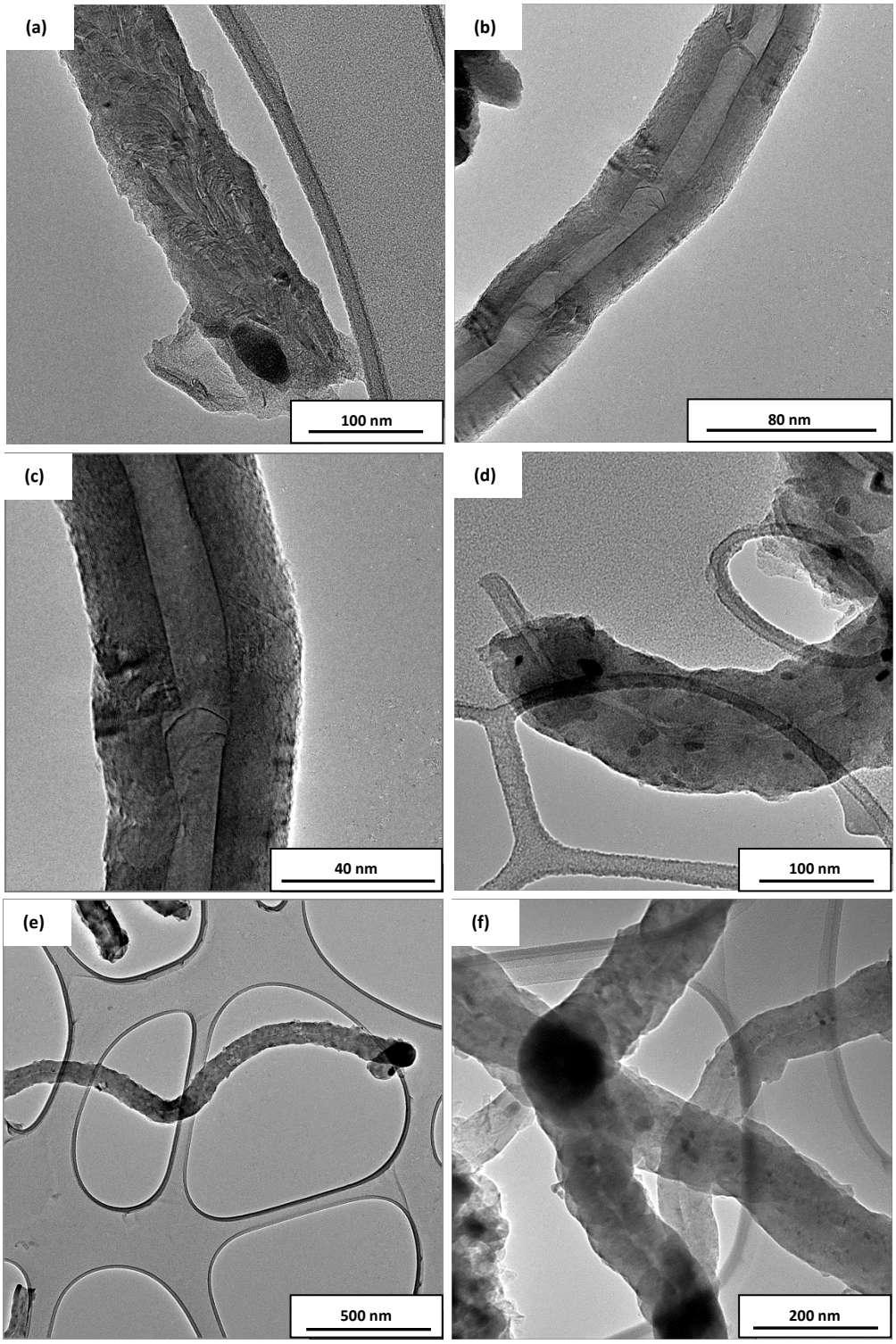


Figure 5.8. TEM micrographs of nanofilamentous materials formed under various reaction conditions showing a: **(a)** CNF, **(b)** CNT, **(c)** CNT showing rolled graphene sheets, **(d)** CNF with a herringbone morphology, **(e)** CNF with a metal particle at its tip and **(f)** CNF with a metal particle in the middle.

For instance, the TEM micrograph shown in Figure 5.8 (c) (which is a section of Figure 5.8 (b)), provided evidence that the CNT shown therein was composed of graphene sheets that were rolled into a tube to form multi-walled CNTs (see Figure 2.3 in Chapter 2.3.1) as described by Shaikjee *et al.* [12], as opposed to graphene sheets that were stacked on top each other to form either the platelet-like or herringbone structures that were observed in Figure 5.8 (a). Also, as reported by Shaikjee *et al*. [12] a very common observation in these ensembles of carbon nanofilaments was the presence of CNFs with graphene sheets stacked as herring-bone structures (Figure 5.8 (d)).

Metal particles were generally observed either at the tips (Figures 5.8 (a) and (e) or in the middle (Figure 5.8 (f)) of these CNTs/CNFs (*see Appendix 6 for energy dispersive spectroscopy (EDS) results of the metal particle*). In the case of CNT/CNF growth, two dominant growth mechanisms have been reported [5, 13, 14] i.e. the tip growth mechanism (as evidenced in Figures 5.8 (a) and (e)) and the root growth mechanism, which was not observed in these filamentous materials. The root growth mechanism occurs when the catalyst-support or metal-support interaction is strong, but in the case where MD occurs, the interaction is weak, hence a tip growth mechanism is most often observed. Metal particles in the middle of the carbon filaments, shown in Figure 5.8 (f), have also been reported by Zeng *et al*. [6] where carbon nanofilament growth and MD corrosion relationships were investigated and it was suggested that filaments may have grown in two directions from a twin crystal metal particle with different orientations. In research pertaining to carbon materials with helical morphologies, it has been reported that different shapes of catalyst particles have been responsible for the production of helical-shaped or in this case linear CNFs [15].

For applicative purposes, beyond the scope of this work, the removal of these metal particles from CNTs produced via MD (as described in this study) for hydrogen storage has been achieved [2]. Chang *et al.* [2] have shown that most of the metal particles in CNTs produced via MD could be removed via heat treatment, where amorphous carbon was also burnt off producing thinner and

smoother tubes. However, this heat treatment was insufficient to remove the metal particles at the tips of these CNTs and further treatments (using boiling nitric acid) were required [2].

5.3.4. Reaction Kinetics

As previously indicated, the masses of the Hastelloy C276 blocks increased with reaction duration and flow rate as a consequence of the carburisation of toluene over Hastelloy C276. The kinetics of this reaction, using these mass increases was therefore studied in order to establish the order of this reaction with respect to toluene. Initially, the mass gains per area of the Hastelloy blocks relative to their flow rates (as reaction duration was increased) for a fixed reaction temperature (800 °C) were plotted (Figure 5.9).

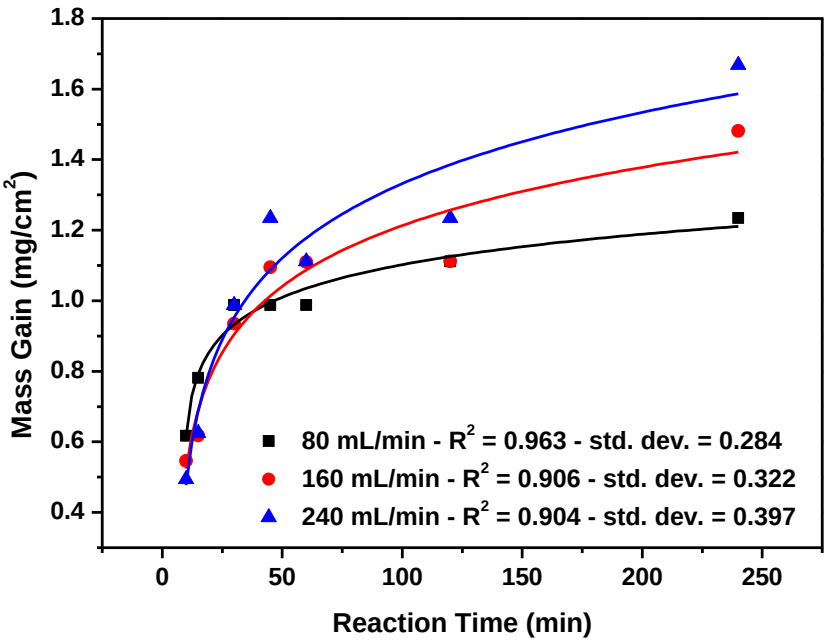


Figure 5.9. A plot of the effect of reaction duration at various flow rates on the mass of carbon gained per area on Hastelloy C276 at 800 °C.

Mass gain due to carbon deposition (i.e. carburisation) over increased reaction time is a familiar occurrence with MD. However, the mathematical functions used to fit such observations have differed widely due to different reaction conditions and alloy compositions or modifications [16-19]. In certain instances no mathematical functions have been able to fit the trends that have been observed [18]. When the data (i.e. the mass of carbon gain per area) were fitted for this study, a logarithmic increase in the mass of carbon gained (per area of Hastelloy block) with increased flow rate (as reaction duration was increased), was observed. This data was then converted to a carburisation rate (i.e. mass of carbon gained per area of Hastelloy block per hour of reaction) and replotted with respect to flow rate and duration of reaction (Figure 5.10). From this data it appeared that the carburisation rate started at some larger value initially and then decreased exponentially to a steady, slower rate for all flow rates as the reaction proceeded with time. At short reaction times, the high carburisation rate may have been due to the fresh metal surface of the Hastelloy block was exposed and interacted with the vaporised toluene easily. At longer reaction times the surface of the Hastelloy was already saturated with carbon and fewer metallic particles would be exposed for MD to occur, hence the carburisation rate decreases at longer reaction times. Initially at short reaction times at 80 mL/min, the carburisation rate was higher as opposed to 160 and 240 mL/min. At a slower flow rate (80 mL/min), the vaporised toluene had a longer residence time to interact with the Hastelloy block. In terms of faster flow rates (i.e. 160 and 240 mL/min), a shorter residence and hence less interaction with the Hastelloy block may have contributed to a low carburisation rate.

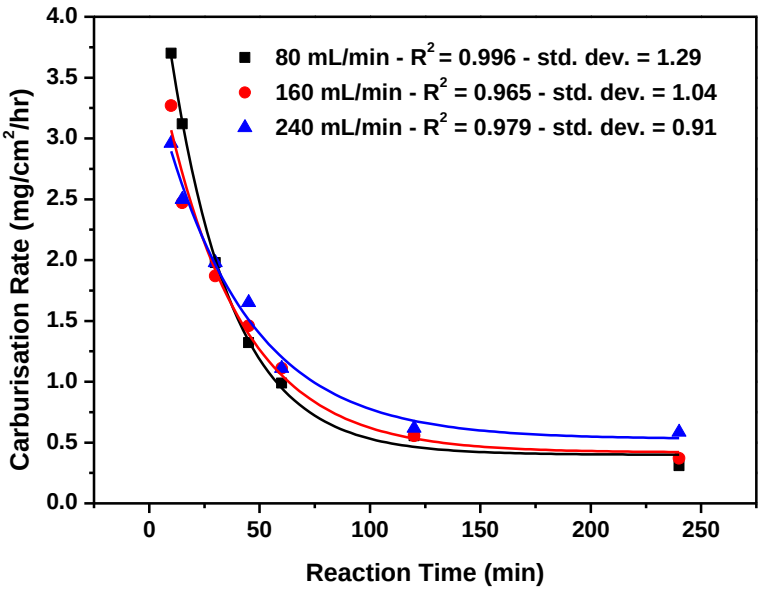


Figure 5.10. A plot of the effect of flow rate on the carburisation rate on Hastelloy C276 at 800 °C.

When the carburisation rate became constant (Figure 5.10), it was observed at 80 mL/min that the carburisation rate was low as compared to higher flow rates. At low flow rates since the surface was already saturated with carbonaceous material, the vaporised toluene may have had more time to react with the carbonaceous material already deposited. This observation was in line with the increase in carbon nanofilament diameter at low flow rates as compared to higher flow rates (Figure 5.7). However, at higher flow rates there were more vaporised toluene passed through the system, but with a shorter residential time to react with the carbonaceous material that had already formed, hence the carbon nanofilaments were smaller in diameter. However, at higher flow rates the vaporised toluene, being more haste may have precipitated under Ni or other metallic particles may have grown into more carbon nanofilaments increasing the carburisation rate at higher flow rates and longer reaction times. Continuous carbon precipitation under Ni particles has been reported in the MD mechanism for Ni as shown in Chapter 2 (Figure 2.9) [6].

In order to determine the order of the carburisation reaction with respect to toluene, two plots were drawn up based on first or second order kinetics. The first was a plot of the natural logarithm of the carburisation rate versus duration of reaction (Figure 5.11) and the second a plot of the inverse of the carburisation rate versus duration of reaction (Figure 5.12).

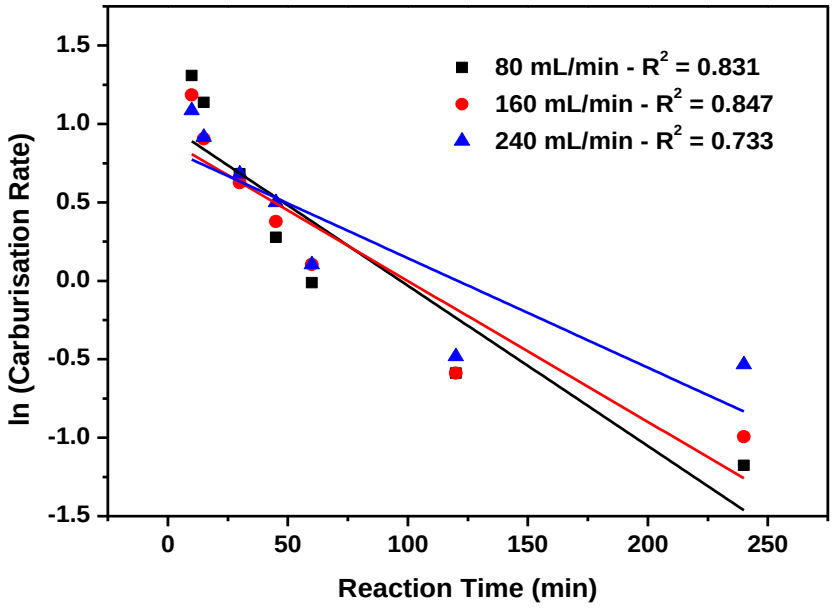


Figure 5.11. A plot of the natural logarithm of the carburisation rate versus the duration of reaction.

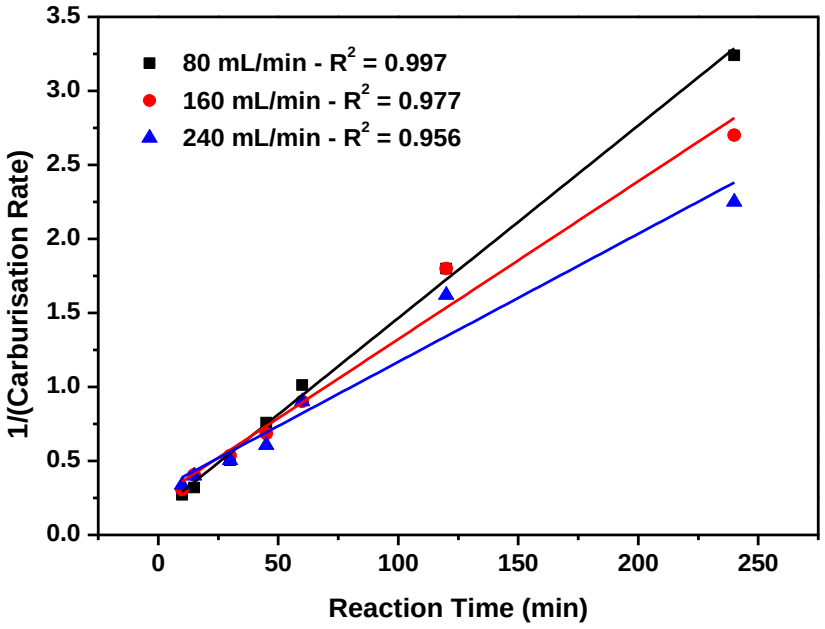


Figure 5.12. A plot of the inverse of the carburisation rate versus the duration of reaction.

When the fits for these plots were compared, it was found that the straight lines that were obtained for the plot of the second order reaction rate (Figure 5.12) had high confidence levels (R^2 > 0.95), while the plot for the first order reaction (Figure 5.11) had much lower one (R^2 < 0.847). Based upon this it was concluded that the data obtained best fit a 2nd order rate law for the synthesis of carbon nanomaterials from toluene on Hastelloy C276 (Figure 5.12) i.e. the rate law was best expressed as:

$$-\frac{d[toluene]}{dt} = +\,Carburisation\,rate = k[toluene]^2.$$

5.3.5. Activation Energy (E_a)

Zeng *et al.* have shown that the crystallisation of carbon could not take place in a satisfactory manner at low temperatures and that catalytic activation was required for this process due to the strength of the sp^2 C – C bonds which would otherwise have resulted in a very high melting temperature of carbon (4492 °C) [6]. For these reasons the activation energies for the carburisation of toluene on Hastelloy C276 were explored at different, relatively high temperatures as shown in Table 5.2. The values of these activation energies were determined as derived from the equations shown below (*see Equation* 13) based on the conclusion that the rate of the carburisation reaction was second order with respect to toluene (*see Section 5.3.4*).

The activation energy (E_a) was determined for the reaction of toluene over Hastelloy C276 to synthesize carbon nanomaterials, by starting with the well-known Arrhenius equation (1). Here the dependence of temperature for reaction rates was represented by:

$$k = Ae^{-\frac{E_a}{RT}} \qquad (1)$$

where k = rate constant, A = pre-exponential factor, E_a = activation energy, R = relative gas constant and T = temperature in Kelvin.

Since the pre-exponential factor was not known, two different reaction temperatures and two rate constants were required, in order for this constant to be eliminated i.e.:

$$k_1 = Ae^{-\frac{E_a}{RT_1}} \qquad (2)$$

$$k_2 = Ae^{-\frac{E_a}{RT_2}} \qquad (3)$$

Applying natural logarithms to both equations yielded:

$$lnk_1 = lnA - \frac{E_a}{RT_1} \qquad (4)$$

$$lnk_2 = lnA - \frac{E_a}{RT_2} \qquad (5)$$

By rearranging equation 5 this gave:

$$lnA = lnk_2 + \frac{E_a}{RT_2} \qquad (6)$$

When equation 6 was substituted into equation 4 and rearranged it gave:

$$lnk_2 - lnk_1 = -\frac{E_a}{RT_2} - \left(-\frac{E_a}{RT_1}\right) \qquad (7)$$

By applying logarithmic properties into equation 7 and simplifying this gave:

$$ln\frac{k_2}{k_1} = \frac{E_a}{R}\left(\frac{1}{T_1} - \frac{1}{T_2}\right) \qquad (8)$$

Finally, when equation 8 was rearranged to make E_a the subject of the formula this gave:

$$E_a = \frac{ln\frac{k_2}{k_1} \times R}{\left(\frac{1}{T_1} - \frac{1}{T_2}\right)} \qquad (9)$$

Although the rate constants (k_1 and k_2) were unknown, the reaction rate at each of these different temperatures (i.e. T_1 and T_2) could be measured, as the reaction order had been determined (*see Section 5.3.4*). This led to:

$$Rate_1 = k_1[Toluene]^2 \qquad (10)$$

$$Rate_2 = k_2[Toluene]^2 \qquad (11)$$

Since the concentration of toluene remained fixed in each reaction, then combining 10 and 11 gave:

$$\frac{Rate_2}{Rate_1} = \frac{k_2}{k_1} \qquad (12)$$

Finally substituting equation 12 into 9 yielded:

$$E_a = \frac{\left(ln\frac{Rate_2}{Rate_1}\right) \times R}{\left(\frac{1}{T_1} - \frac{1}{T_2}\right)} \qquad (13)$$

Equation 13 was then used to determine the E_a for reactions that were conducted at combinations of 800 °C, 850 °C and 900 °C as shown in Table 5.2.

Table 5.2. The determination of E_a at different temperature ranges

Temperature $_1$ (°C)	Temperature $_2$ (°C)	E_a (kJ/mol)
800	**850**	**46.82**
800	**900**	**44.26**
850	**900**	**41.46**

As seen in Table 5.2 the activation energies for different temperatures were relatively similar. Taking an average and standard deviation of these values in Table 5.2 yielded an E_a of 44.18 ± 2.68 kJ/mol. A good comparison for the data reported here is by the related work of Grabke *et al.* [20-22] where an activation energy of 55 kJ/mol was reported for reaction temperatures greater than 540 °C. It is of interest to note that although the above-mentioned value was reported for an Fe-based or low alloy steel, where H_2-24%CO-2%H_2O were used (and the carbon black that was formed was reported as coke), it closely resembled the average

value determined in this study. This is despite the fact that in this present study a different carbon source and alloy (i.e. a Ni-based Hastelloy) were used.

As mentioned above, the activation energies reported in Table 5.2 were found to be reasonably consistent in the temperature range reported (i.e. 800 – 900 °C). However, when the activation energies were determined at lower temperatures (i.e. < 800 °C) they were found to be larger, just as Grabke *et al.* [20-22] observed, but significantly less consistent *(see Appendix 7)*. This inconsistency was considered to primarily be due to the small incremental changes in mass of carbon material that were obtained at low reaction temperatures, which in turn caused increased the errors when the rates of these reactions were determined.

5.3.6. Powder X-ray Diffraction (PXRD)

The bulk Hastelloy C276 in its supplied form and after being exposed to MD conditions (over different flow rates) was analysed by PXRD and the patterns of each were displayed in Figures 5.13-5.15 respectively. It was found that the patterns were very similar across the flow rates studied. Likewise similarities in these patterns were also seen at different durations of reaction ranging from 10 to 240 min. Hence for simplicity, only patterns for reactions that were carried out for: 15, 45 and 240 min as well as a blank Hastelloy C276 are shown in the respective Figures *(see Appendix 8 for PXRD patterns with regard to the entire range of durations of reaction)*.

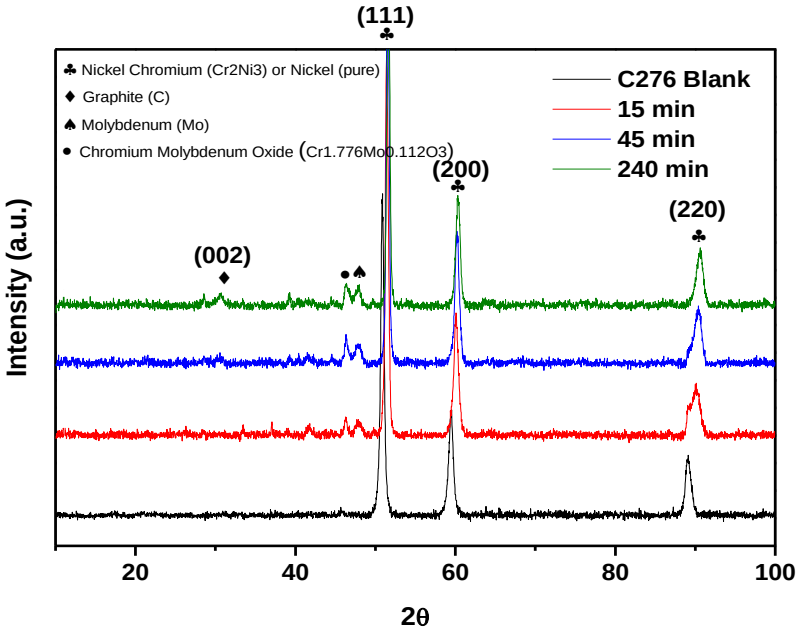


Figure 5.13. PXRD patterns of Hastelloy C276 exposed to MD conditions at 80 mL/min of different durations of reaction.

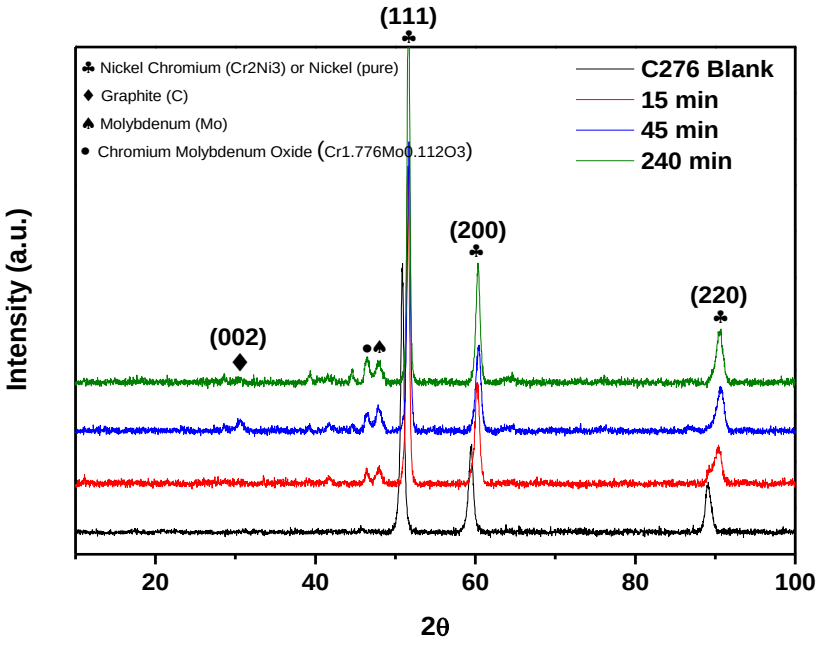


Figure 5.14. PXRD patterns of Hastelloy C276 exposed to MD conditions at 160 mL/min of different durations of reaction.

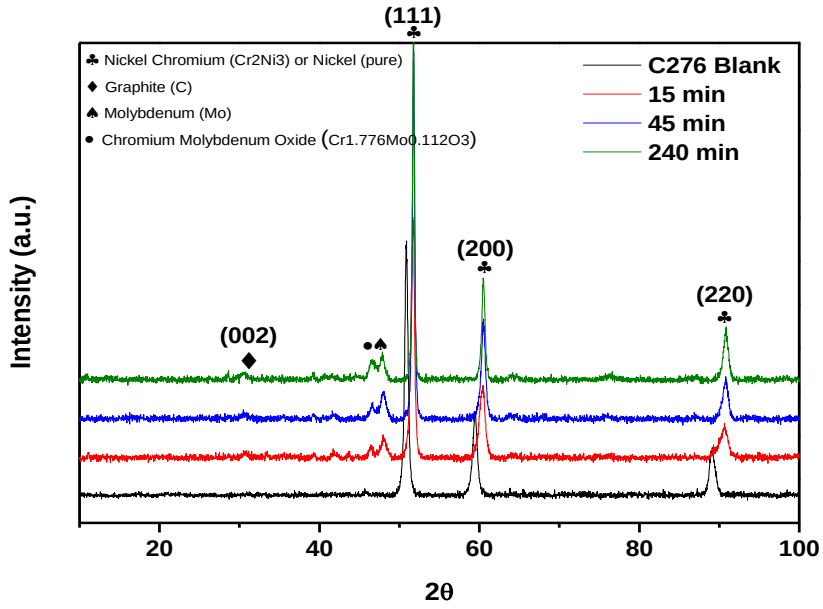


Figure 5.15. PXRD patterns of Hastelloy C276 exposed to MD conditions at 240 mL/min at different durations of reaction.

Here it was noted that the nickel chromium (Cr_2Ni_3) was the major phase observed before and after MD, which was consistent with the two main elemental constituents of Hastelloy C276. Many of the other constituents such as Mo and Fe or phases including these constituents tended to overlap this peak area. The peaks were indexed so that the main elements took priority. Peaks shown in Figures 5.13-5.15 were assigned to a FCC lattice system with (111), (220) and (200) planes which ranged from the strongest to the weakest peaks for the nickel chromium phases. Besides the nickel chromium phase, a pure nickel phase was indexed to this pattern and as before was also assigned to a FCC lattice system with (111), (220) and (200) planes which ranged from the strongest to the weakest peak. Several chromium molybdenum oxide peaks were also observed, however only the most distinct peak was matched here (*see Figure 4.6 for comprehensive indexed pattern*). Another distinct feature of the PXRD pattern was the appearance of a molybdenum peak at $2\Theta = 47.9°$. This observation was unforeseen, since no molybdenum phases appeared in the blank sample as well as

in Figure 4.6 were a PXRD pattern of an oxidised sample of Hastelloy C276 at 800 °C showed no evidence of this molybdenum phase. Hence, the presence of this molybdenum phase may have been due to the presence of carbon and consequently the MD mechanism.

Although indisputable evidence of carbon, in the form of nanofilaments, was observed in the TEM micrographs (Figures 5.8 (a)–(f)), which were later confirmed by laser Raman spectroscopy (*see section 5.3.7*) to have a graphitic nature, only a faint graphitic peak was observed in the PXRD patterns (Figures 5.13-5.15) at about 30.5° 2Θ. In some instances, especially low durations of reaction i.e. 15 min, no peak was observed at all. It is believed that the low intensity or even lack of this peak was due to the following reasons; (1) A bulk PXRD technique was used for these analyses and (2) The carbon content that was deposited on the surface or to some extent below the surface was minute i.e. < 5wt.%, which was below the detection limits of the instrument.

In order to establish if the graphitic carbon could be better detected, grazing incidence XRD was conducted on the surface of Hastelloy C276 instead of using bulk PXRD for the analysis, using the same Hastelloy block exposed to vaporised toluene at 80 mL/min for 1 h. The results of this analysis (Figure 5.16) revealed that a distinct graphite peak was present at about 2Θ = 25.8°.

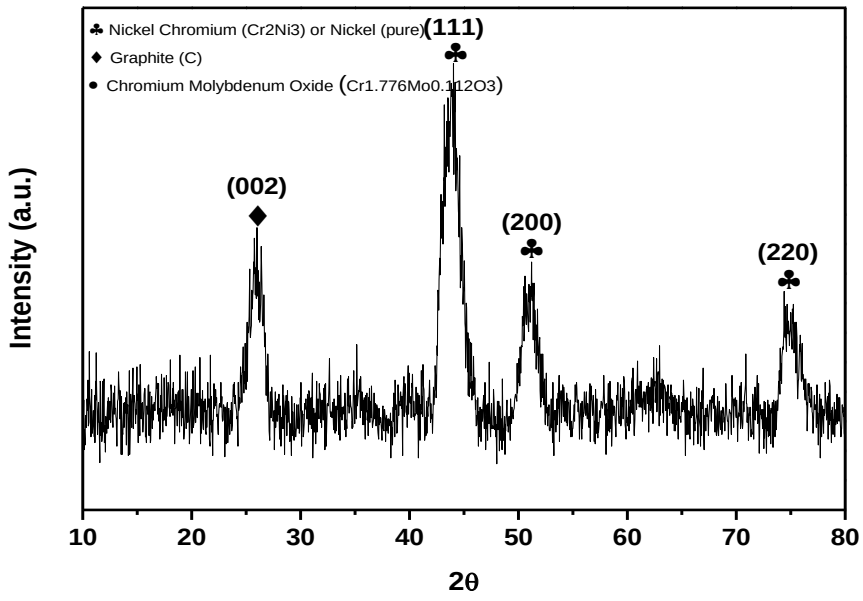


Figure 5.16. The **g**razing angle XRD pattern of the surface of Hastelloy C276 exposed to MD.

It must be noted here that the 2Θ angles differed from those reported for the bulk PXRD (i.e. 2Θ = 30.5°) as Cu radiation was used for the grazing angle XRD analysis as compared to Co radiation in the bulk PXRD analyses that were previously shown (Figures 5.13-5.15). The nickel chromium or pure nickel peaks were also observed by this technique.

Using the results from the grazing angle XRD analysis the graphite peaks were assigned to a hexagonal lattice with space group *P*63/*mmc* system and a (002) plane. This (002) plane of graphite was found to be consistent with the findings of Zeng *et al*. [23] (*see section 5.3.7*). Similarly, Yang *et al*. have schematically illustrated the formation the (002) graphite plane after the diffusion and precipitation of carbon from a metal particle as shown in Figure 5.17[24]. Here it was also noted that the graphite was parallel to the metal/graphite interface. These findings exhibited sp^2 hybridisation where carbon atoms were bonded strongly within layers, with these layers being bound by weak van der Waals forces in a

hexagonal crystalline structure which resembled a honeycomb network (described in *Section 5.3.7*).

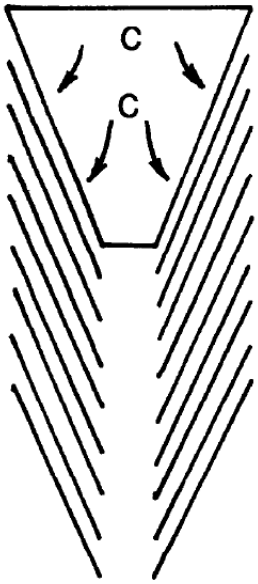


Figure 5.17. Schematic representation of the formation of the (002) graphite plane after precipitation of carbon from a metal particle**[24]**.

Further analysis of the PXRD patterns was then carried out based upon the data obtained as shown in Figures 5.13-5.15. Here it was noted that when Hastelloy C276 blocks were exposed to MD conditions, the PXRD patterns showed shifts of about 1° 2Θ when compared to the blank Hastelloy C276 blocks (as seen in the PXRD patterns in Figures 5.13-5.15). For clarification purposes the nickel chromium or pure nickel peak that was indexed with the (111) plane from Figure 5.13 was further magnified and shown in Figure 5.18. Here similar observations were seen for the nickel chromium or nickel peaks that were indexed at (200) and (220). It was also noted from Figure 5.18 as the duration of the reaction increased, the (111) peak shifted further and further to the right (i.e. the 2Θ shift increased).

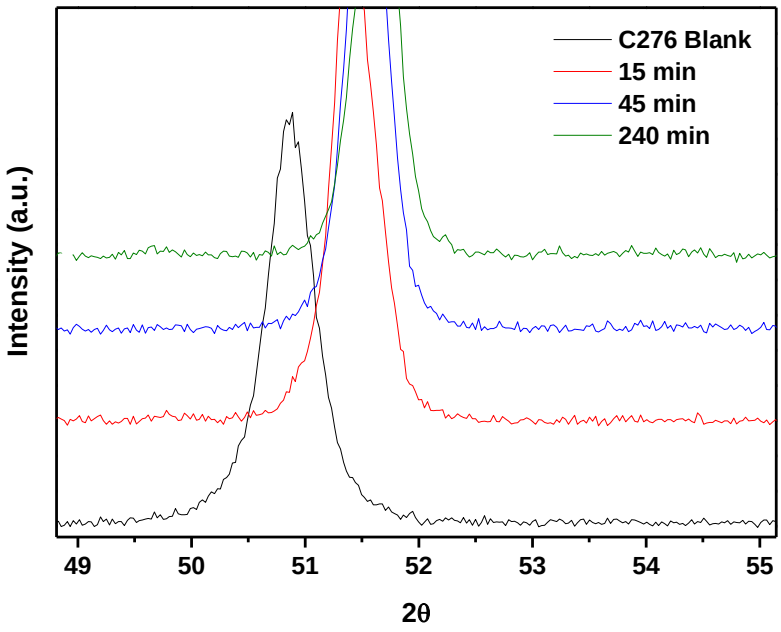


Figure 5.18. Magnification of PXRD patterns of the nickel chromium or nickel (111) plane of Hastelloy C276 at 80 mL/min ***(from Figure 5.13)***.

According to Bragg's law, nλ = 2dSinϴ, the inter-planar distance (d) of the crystalline lattice decreased when 2Sinϴ increased (as a consequence of the shift to larger values of 2ϴ). This implied that the graphite deposition which occurred on the Ni (111) surface may have caused a compressive stress on Hastelloy C276 before the growth of graphite into the Hastelloy, which in turn caused volume expansion and hence MD. This observation was consistent with Grabke *et al.* [25], who have suggested that for Ni and Ni-based alloys, initiation of graphite growth took place on the defective areas of the surface. After nucleation it was suggested that further attached into graphite planes took place by the oversaturation of carbon atoms [25]. Thereafter the inward growth of graphite into the metal matrix, which also occurred at the surface and grain boundaries of the metal was thought to have caused ***compressive stresses***; hence it is suggested that metals were pressed outwards from the metal matrix [25].

5.3.6.1. Carbon Crystallisation via MD

Catalytic crystallization of carbon would have had to occur in order for carbon nanofilaments to have been synthesised. It has been reported that Ni has improved the crystallinity of carbon materials in such reactions [23]. Zeng *et al*. [6] have suggested a mechanism for Ni and Ni-based alloys *(Section 2.4.3.2 – Figure 2.9)* where carbon atoms once deposited on a Ni surface, dissolve into and diffuse though its lattice. Thereafter it was proposed that crystallised carbon formed on the other side of the Ni lattice, as represented in Figure 5.19 [6]. In this way Ni particles would then have been dislodged from the nickel lattice, while carbon continued to precipitate and grow into a carbon nanofilament [6, 23].

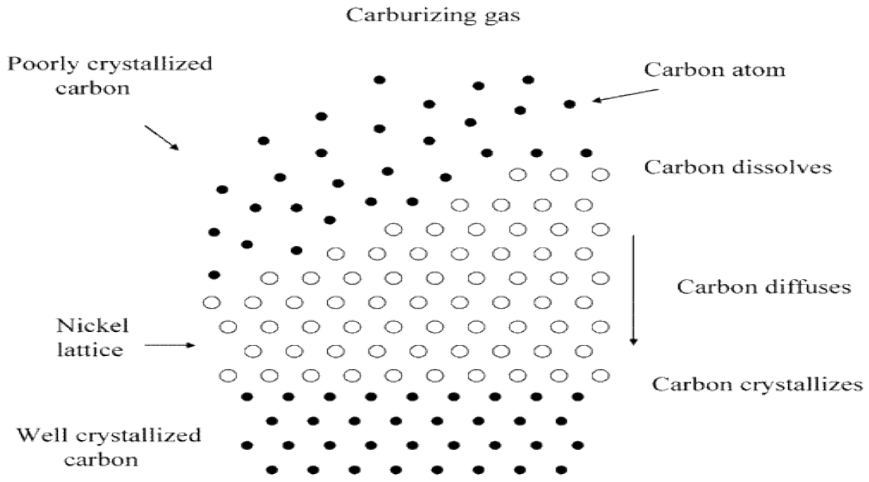


Figure 5.19. Process of carbon crystallisation via the assistance of Ni **[6]**.

In this mechanism the crystallisation of carbon were suggested to have favoured a facet where its atomic distance matched the lattice of graphite [6]. This is indeed consistent with carbon growth which has been reported on the Ni (111) facet [6, 24, 26, 27]. On the other hand the growth of carbon on the Ni (200) plane has been reported to be considerably less than the Ni (111) facet since the Ni (200) was not favourably orientated for epitaxial graphite deposition [26]. Additionally, extended Hückel molecular orbital (EHMO) calculations have showed that the Ni (111) faces contributed stronger epitaxial fits with graphite [24] and also indicated

that the most favourable faces for graphite binding were as follows: (111) > (311) > (100) > (110) [24].

For all these reasons it is believed in this study (as seen in Figures 5.13-5.16 and especially Figure 5.18) that the Ni (111) facet played a dominant role in the reaction of toluene with Hastelloy C276 and hence the high degree of carburisation that was observed in these experiments.

5.3.7. Laser Raman Spectroscopy

The carbon nanofilaments that were synthesized between 10-240 min at: 80, 160 and 240 mL/min were then analysed by laser Raman spectroscopy. The Raman spectra obtained for these materials are represented in Figures 5.20-5.22. In each case the defective (D) and graphitic (G) bands began to be observed for reactions from as early as 10 min all the way up until 240 min, across the flow rates that were studied. In Raman spectra, highly crystallised carbon have been known to show a sharp G band at 1580 cm^{-1} that has been allocated to the E_{2g} C – C stretching mode [28-30]. On the other hand, the D band has been known to be observed at 1355 cm^{-1} with an A_{1g} C – C breathing mode[31]. In this study the G bands were found to have ranged 1578 – 1582 cm^{-1} and the D bands 1349 – 1353 cm^{-1} respectively, which were consistent with their expected values.

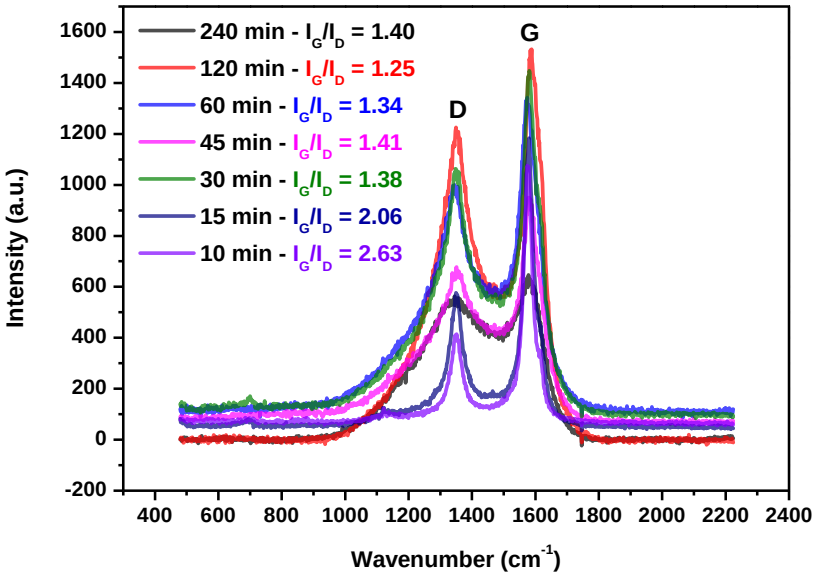


Figure 5.20. Raman spectra representing the D and G Bands of carbon nanofilaments synthesized at 80 mL/min.

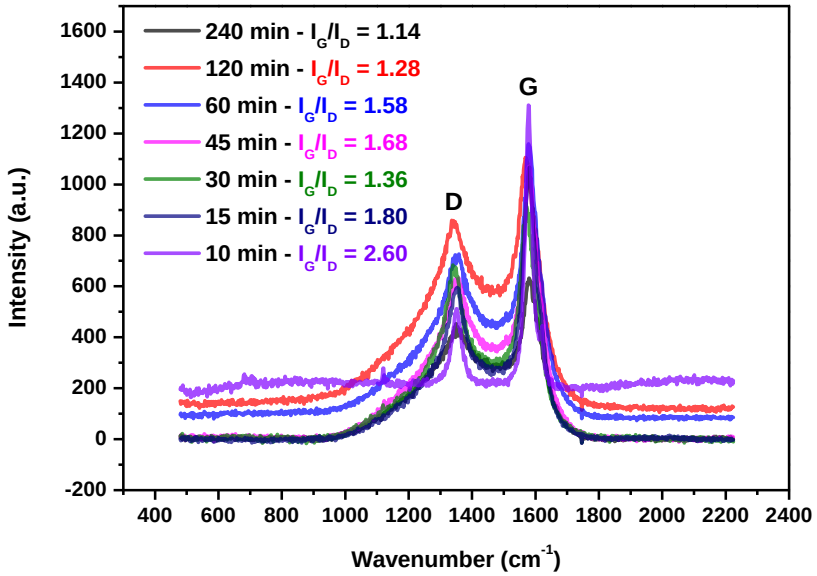


Figure 5.21. Raman spectra representing the D and G Bands of carbon nanofilaments synthesized at 160 mL/min.

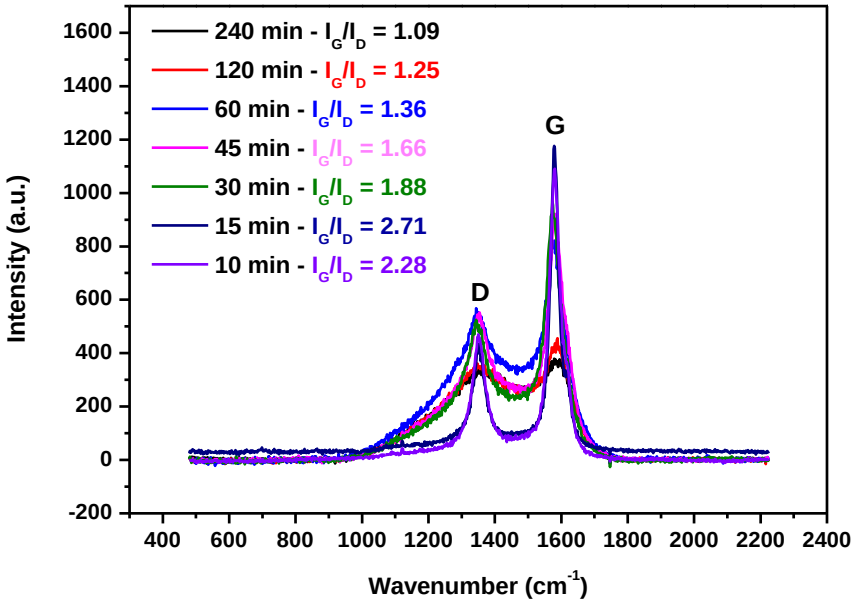


Figure 5.22. Raman spectra representing the D and G Bands of carbon nanofilaments synthesized at 80 mL/min.

In general it was observed that the I_G/I_D ratios decreased as the duration of the reaction increased from 10 min to 240 min (Figures 5.20-5.22). This observation appeared to be counterintuitive, since the SEM micrographs in Figures 5.4-5.6 revealed that the carbon nanofilaments that were synthesized after shorter durations of reaction were less well-developed and should have had more defective carbon present (i.e. should have had lower I_G/I_D ratios). Conversely carbon nanofilaments formed after longer durations of reaction should have had higher I_G/I_D ratios.

Therefore an explanation was sought to account for this observation. The structure of graphite has been reported to be layered with a space group of *P*63/*mmc* [6, 23]. As previously shown (*see Section 5.3.6*) the graphitic structure in this present study was also found to have a space group of *P*63/*mmc* (Figure 5.23) [6, 23]. Here the carbon atoms were strongly bonded via sp^2 hybridisation within their layers and formed a 2-D honeycomb network. These layers, typically 3.354 Å

apart, were stacked in hexagonal crystalline structures which were most likely bound together by van der Waals forces, which caused them to become disordered along the c-axis [6, 23].

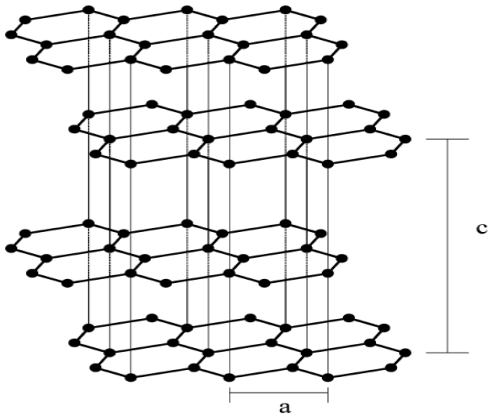


Figure 5.23. P63/mmc structure of graphite **[23]**.

Accordingly, it is believed that as the duration of the reaction increased, more carbon was deposited and the disorder among the c-axis was increased. Hence, the hexagonal symmetry of the graphite lattice was broken down, which enhanced the D peak and reduced the G peak. At the same time Zeng *et al*. [23] have reported that when carbon, synthesised by MD, adhered to a nickel surface it showed better crystallinity. Conversely carbon which did not adhere to a nickel surface, was shown to possess poor crystallinity [23]. Since fresh metal particles would have been fewer on the surface as the duration of the reaction increased (i.e. only dislodged metal or Ni nanoparticles would have been available for carbon crystallisation), this may have given rise to an increased quantity of poorly crystallised carbon being deposited. This notion was consistent with the observation that the rate of reaction decreased as the duration of reaction increased (Figure 5.10). Hence, together with the disorder that may have been introduced along the c-axis, these two phenomena may have accounted for the decrease in the I_G/I_D ratios that were observed as the duration of the reaction was increased.

In addition to the above reasoning and looking at the overlap of the D and G peaks, which occurred at longer reaction times in the Raman spectra as noted in Figures 5.20-5.22, Ferrari *et al.* [31] attributed the shapes of the Raman spectra to: (1) clustering of the sp^2 phases, (2) bond disorder, (3) the presence of sp^2 rings or chains and (4) the sp^2/sp^3 ratio as seen in Figure 5.24.

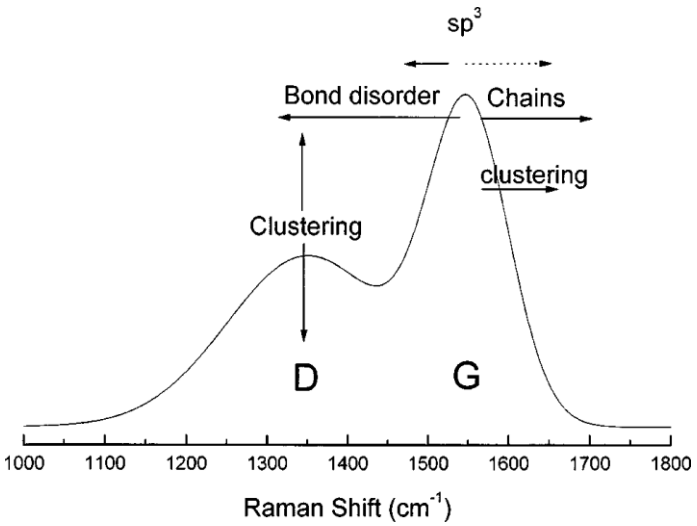


Figure 5.24. Issues which influence of the shape of the laser Raman spectrum **[31]**.

Another observation regarding the studies across the flow rate range was that as the flow rate increased with increased duration of reaction, the I_G/I_D ratio generally decreased (Figure 5.25).

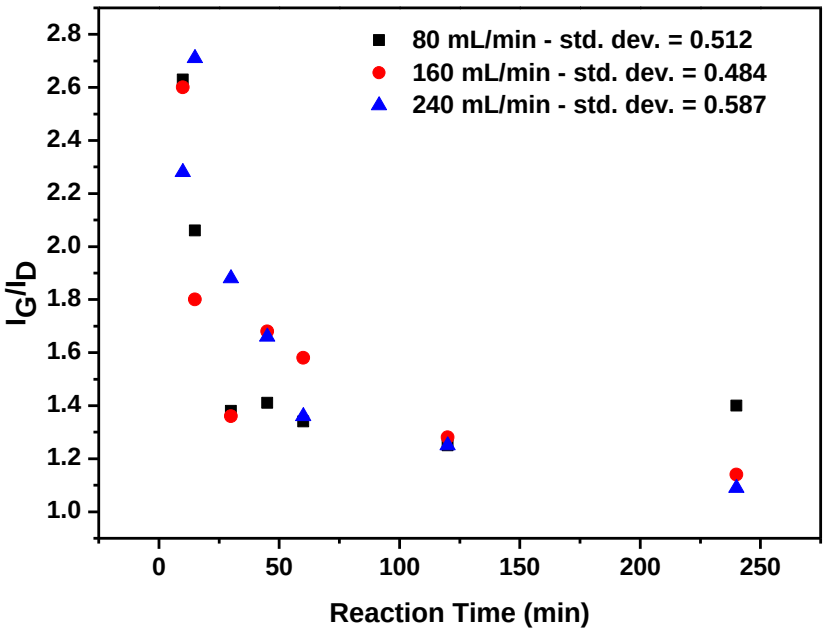


Figure 5.25. A plot of the effect of flow rate on the I_G/I_D ratio as the duration of reaction increased.

The rationale behind this observation was that at higher flow rates there was less time for toluene vapour to interact with the metal particles formed in the MD mechanism in order for carbon to crystallise. However, when flow rates were lowered the interaction time was increased and better crystallinity of carbon occurred, hence a higher I_G/I_D ratio was observed.

5.3.8. MD mechanism and Carbon Nanofilament Formation Relationship

Despite the various MD mechanisms, common catalysts for the synthesis of CNTs include transition metals. The most commonly used are: Fe, Ni and Co since they possess high carbon diffusion rates especially at high temperatures [5]. The most

widely accepted mechanism reported by Kumar *et al*. [5] in a review regarding the growth mechanisms and mass production of CNTs by CCVD has been described as follows: Hot metal nanoparticles come into contact with hydrocarbon vapour. The hydrocarbon vapour decomposes into carbon and hydrogen. The hydrogen gas escapes and the carbon is dissolved into the metal. The metal than reaches carbon solubility at a specified temperature and the carbon precipitates out in a cylindrical network. The decomposition of hydrocarbons releases heat to the metal exposed whilst the crystallisation of carbon absorbs heat from the area were the metal precipitates. The continuation of crystallisation is due to the rigid thermal gradient inside the metal particle. The mechanism discussed above is widely accepted and is known as the vapour liquid solid (VLS) mechanism which was first proposed for the growth of silicon whiskers [32] and adopted by Baker *et al*. [33, 34] for the growth of filamentous carbon nanomaterials.

Two overall cases exist for the VLS mechanism i.e. the tip growth model (Figure 5.26 (a)) and the base-growth model (Figure 5.26 (b)) [5].

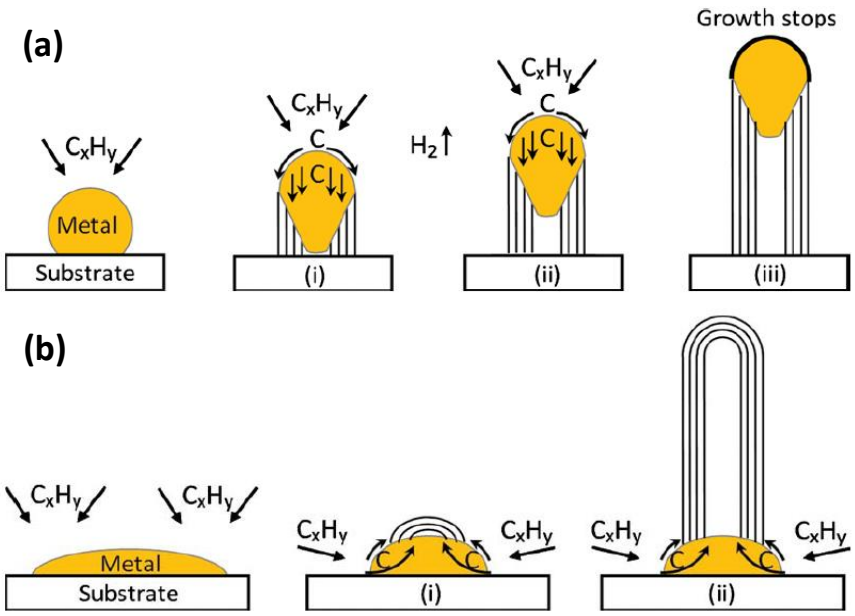


Figure 5.26. VLS model showing: **(a)** Tip growth and **(b)** Root growth mechanism **[5]**.

The tip growth model (Figure 5.26 (a)) occurs when there is a weak interaction between the catalyst and the substrate [5]. Decomposition of the hydrocarbon source occurs at the surface of the metal and diffuses. Precipitation of the CNT occurs at the bottom of the metal particle, dislocating the metal particle off from the substrate. Carbon diffusion continues and the CNT continues to grow. When the metal particle is saturated with carbon, the catalytic activity is halted and CNT growth is discontinued. In the case of the base growth model (Figure 5.26 (b)), there is a strong interaction between the catalyst and substrate. The hydrocarbon source decomposes on the surface of the metal as in the tip growth model. However, the precipitation of carbon in this case is unsuccessful in pushing the metal particle out and precipitation occurs from the highest point of the metal particle. Continued hydrocarbon deposition takes place and the dissolved carbon diffuses upwards; hence the CNT grows upwards with the catalyst particle adhered to its base. The concepts proposed by Zeng *et al*. [6] explained by Figure 5.19 and the VLS model are recognised to be identical in terms of carbon crystallisation. Hence, it can be established that the Ni nanoparticles and other metals in small quantities such as Fe constituted in Hastelloy C276 or any other alloy, can act individually to catalyse the growth of CNTs/CNFs. Looking at Figure 4.2(c) and 5.1, the polished and unpolished form of Hastelloy C276, no facets were observed. However, when the polished sample was subjected to a heat treatment process, faceted particles were observed as seen in Figure 4.2 (b.). The exposures of these facets, especially those which though carbon can diffuse and precipitate out off were then subjected to MD. The exposure of these faceted particles was a result of increased temperatures which was an important factor which influenced the MD mechanism. For unpolished alloy surfaces these facets would have been more prone to carbon nanofilament formation since the surfaces were rough and faceted particles would have been more easily available for the growth of carbon nanofilaments as the data in Figures 5.4, 5.5 and 5.6 showed. From these observations, it was conclusive that the MD mechanism took place in these studies in a similar manner to the MD mechanism as proposed by Zeng *et al*. [6, 23] *(section 2.4.3.2 – Figure 2.9)* in accordance with the VLS mechanism.

Additionally, the SEM analyses (Figures 5.4-5.6) and especially the TEM analyses (Figure 5.8) clearly showed that the tip-growth mechanism, which was characteristic to the VLS model, had taken place. Since the tip growth mechanism resulted in metal particles being removed from the metal substrate/alloy, as a consequence of a weak interaction between the metal nanoparticle and the growth of a carbon nanofilament, this led to MD. Evidence of the root growth mechanism was not observed in this study. This may have been due to two possibilities: (1) Evidence could not be obtained due to the reduced visibility under SEM because of the heavy layers of carbon on the surface of Hastelloy C276, or (2) That the root growth mechanism may not have been involved in the reactions that occurred in this study.

5.3.9. Additional Carbon Nanomaterials (CNMs)

In addition to the formation of the carbon nanofilaments that have been described previously, an additional morphology of carbon was observed on the surface of Hastelloy C276 in its unpolished form in these reactions. This carbon morphology is shown in Figure 5.27(a) (see areas encircled) and was termed as graphite particle structures (GPSs) in this study, although they have also been described as metal particles encapsulated by graphite shells in other studies [19, 35]. These GPSs were exclusively found in the pits of unpolished Hastelloy C276 samples as shown Figure 5.27(b) (see outlined area) as compared to the uneven rough surface where the majority of the carbon nanofilaments were found.

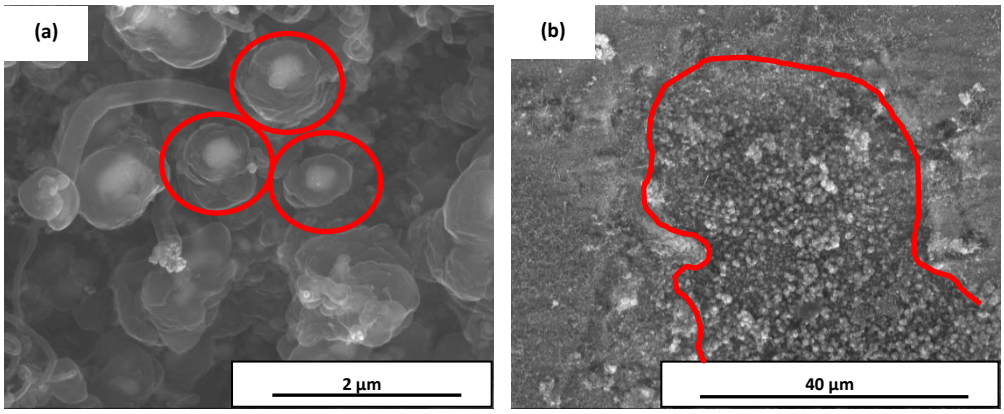


Figure 5.27. SEM micrographs of: **(a)** Graphite particle structures (GPSs) on the surface of unpolished Hastelloy C276 and **(b)** The site where graphite particle structures (GPSs) were formed on Hastelloy C276.

Zhang *et al.* [19, 35] have proposed that the metal particles in the GPSs and carbon nanofilaments may possibly have been the result of different mechanisms. It has been suggested that since a large quantity of graphite particle structures had developed on the surface in particular areas, that an eruption of metal particles had occurred which were encapsulated by graphite shells from a localised inexorable carburising area [35]. In this case, the localised inexorable carburising area may have been the pitted areas on the pristine Hastelloy C276 (Figure 5.1), since this area was attacked extensively by carbon compared to the rough surface. This observation was complimented by OM (Figure 5.28) and EPMA (Figure 5.29). The OM showed that the pits were attacked to a greater extent as compared to the rough surface. To supplement this data, EPMA showed that carbon deposition in the pits where GPSs were grown and accumulated was much denser as compared to areas were carbon nanofilaments were grown.

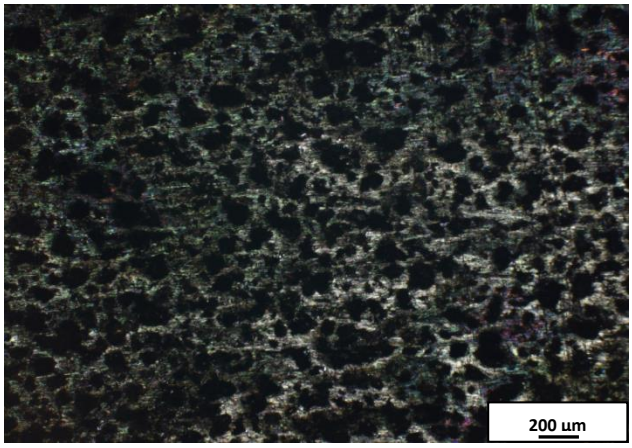


Figure 5.28. OM image showing excessive carbon deposition in the pits of Hastelloy C276.

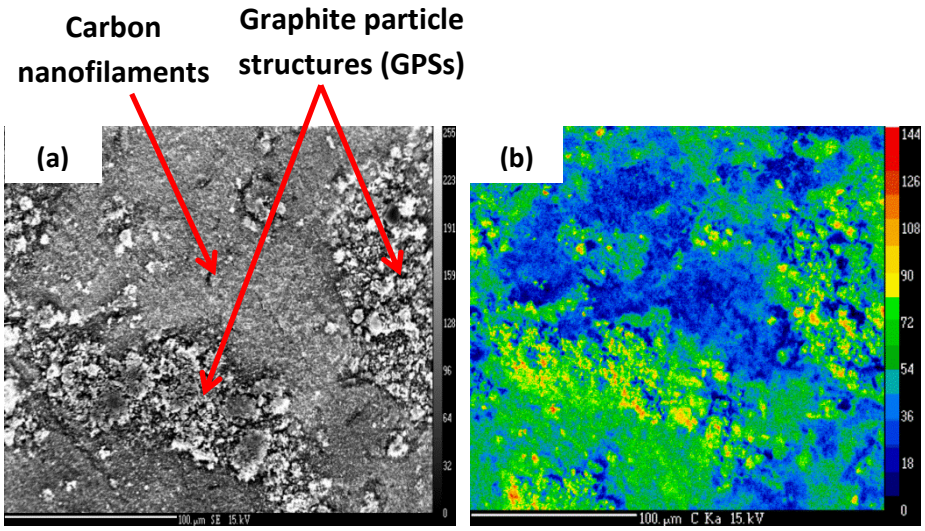


Figure 5.29. Elemental map of carbon nanofilaments and agglomeration of GPSs showing: **(a.)** SEM micrograph of mapped area and **(b.)** C K_{α}.

5.4. Conclusions

Carbon nanofilaments in the form of CNTs and CNFs were concurrently synthesized on the surface of Hastelloy C276 using toluene via the MD mechanism at 800 °C ranging between 10 – 240 min. The CNTs/CNFs at lower durations of reaction were impaired and better formed at higher durations of reaction. The diameters of the carbon nanofilaments varied. At shorter durations of reaction thin carbon nanofilaments were synthesized and longer durations of reaction larger diameter nanofilaments were observed. With regards to flow rate studies, lower flow rates at a fixed temperature (800 °C) resulted in increased carbon nanofilament diameters as opposed to higher flow rates which resulted in smaller diameter carbon nanofilaments. TEM had made it possible to distinguish between CNFs and CNTs.

The kinetics of the carburisation of Hastelloy C276 by toluene showed that as the reaction time increased the carburisation rate decreased. However, a higher carburisation rate was seen at a higher flow rates and decreased as flow rates decreased. From the reaction rate data the reaction which occurred between toluene and the surface of Hastelloy C276 was determined to follow a 2^{nd} order rate law i.e. rate of $carburisation = k\,[Toluene]^2$. Consequently the activation energy (E_a) was calculated and found to be 44.18 ± 2.68 kJ/mol. This result showed a good agreement with the E_a reported in literature regarding MD although different alloys and gas compositions were used.

PXRD executed on the bulk of Hastelloy C276 revealed that Ni was composed of: (111), (200) and (220) planes. Literature confirmed that the (111) planes, the strongest peak, had the most affinity to carbon compared to the (200); hence a favourable amount of crystallised carbon was formed. In some cases a graphite peak was not detected when using the bulk PXRD technique after MD conditions, since it was believed that the quantities of graphitic carbon formed were below the detection limit of the technique. However, grazing incidence XRD gave a positive

result regarding graphite. Shifts in the PXRD patterns of the nickel or nickel chromium peaks to the right i.e. an increase in the 2Θ have suggested that as reaction time increased compressive stresses occurred in Hastelloy C276.

Laser Raman spectra showed that the carbon nanofilaments synthesized were graphitic/crystalline in nature since they possessed an $I_G/I_D > 1$ regardless of the flow rates and duration of reaction involved. However, at longer durations of reaction where I_G/I_D ratios >>1 would have been expected, the I_G/I_D ratios approached unity. Two possible reasons were put forward to explain this observation i.e. the increased disorder that may have been introduced along the c-axis due to the stacking of graphite layers and the formation of disordered carbon due to the depletion of metal in the reaction zone.

Many similarities were identified between the well-known VLS mechanism and the MD mechanism proposed by Zeng *et al*. [6, 23]. The mechanisms showed that the many similarities regarding carbon crystallisation into carbon nanofilaments.

In addition to the formation of carbon nanofilaments, structures known as graphite particle structures (GPSs) were also formed. These structures were formed in the pits of the unpolished surfaces of Hastelloy C276, compared to carbon nanofilaments which were formed on the rough surface. Literature has suggested that the formation of GPSs was not a consequence of MD. To date no applicative purposes have been reported for these structures, hence at this stage they are considered unimportant and a curious side-product.

Lastly, as described in *Section 5.1* many researchers have optimised reaction processes in a variety of ways to use the MD in the synthesis of CNTs. From the work represented in this chapter, different facets of Ni for e.g. the (111) facets are known to have high affinity to carbon. One interlinking solution either to enhance CNT/CNF formation or to eliminate it for the use in petroleum industries is to redesign alloys gaining or reducing certain planes to either allow carbon diffusion/crystallisation or not. So, all things considered, alloys should be

designed either to promote the epitaxial relationship with graphite or not in the case of MD prevention.

5.5. References

1. S. Iijima, *Helical microtubules of graphitic carbon.* nature, 1991. **354**(6348): pp. 56-58.
2. J.K. Chang, H.Y. Tsai, and W.T. Tsai, *Effects of post-treatments on microstructure and hydrogen storage performance of the carbon nano-tubes prepared via a metal dusting process.* Journal of Power Sources, 2008. **182**(1): pp. 317-322.
3. H. Ghorbani, A. Rashidi, S. Rastegari, S. Mirdamadi and M. Alaei, *Mass production of multi-wall carbon nanotubes by metal dusting process with high yield.* Materials Research Bulletin, 2011. **46**(5): pp. 716-721.
4. J.P. Tessonnier and D.S. Su, *Recent progress on the growth mechanism of carbon nanotubes: a review.* ChemSusChem, 2011. **4**(7): pp. 824-847.
5. M. Kumar and Y. Ando, *Chemical vapor deposition of carbon nanotubes: a review on growth mechanism and mass production.* Journal of nanoscience and nanotechnology, 2010. **10**(6): pp. 3739-3758.
6. Z. Zeng and K. Natesan, *Relationship between the growth of carbon nanofilaments and metal dusting corrosion.* Chemistry of materials, 2005. **17**(14): pp. 3794-3801.
7. S.W. Pattinson, B. Viswanath, D.N. Zakharov, J. Li, E.A. Stach and A.J. Hart, *Mechanism and Enhanced Yield of Carbon Nanotube Growth on Stainless Steel by Oxygen-Induced Surface Reconstruction.* Chemistry of materials, 2015. **27**(3): pp. 932-937.
8. M. Hashempour, A. Vicenzo, F. Zhao and M. Bestetti, *Direct growth of MWCNTs on 316 stainless steel by chemical vapor deposition: Effect of surface nano-features on CNT growth and structure.* Carbon, 2013. **63**: pp. 330-347.
9. D.J. Young, J. Zhang, C. Geers and M. Schütze, *Recent advances in understanding metal dusting: A review.* Materials and corrosion, 2011. **62**(1): pp. 7-28.
10. N.A. Jarrah, F. Li, J.G. van Ommen and L. Lefferts, *Immobilization of a layer of carbon nanofibres (CNFs) on Ni foam: a new structured catalyst support.* Journal of Materials Chemistry, 2005. **15**(19): pp. 1946-1953.
11. S.D. Mhlanga, *Synthesis and study of carbon nanotubes and carbon spheres*, 2009, Faculty of Science, University of the Witwatersrand, Johannesburg.
12. A. Shaikjee and N.J. Coville, *The synthesis, properties and uses of carbon materials with helical morphology.* Journal of Advanced Research, 2012. **3**(3): pp. 195-223.
13. Coville, N.J., S.D. Mhlanga, E.N. Nxumalo and A. Shaikjee, *A review of shaped carbon nanomaterials.* South African Journal of Science, 2011. **107**(3-4): p. 01-15.
14. M. Endo, T. Hayashi, Y.A. Kim, M. Terrones and M.S. Dresselhaus, *Applications of carbon nanotubes in the twenty–first century.* Philosophical Transactions of the Royal Society of London A: Mathematical, Physical and Engineering Sciences, 2004. **362**(1823): pp. 2223-2238.
15. A. Shaikjee, P.J. Franklyn, and N.J. Coville, *The use of transmission electron microscopy tomography to correlate copper catalyst particle morphology with carbon fiber morphology.* Carbon, 2011. **49**(9): pp. 2950-2959.
16. H.J. Grabke, *Thermodynamics, mechanisms and kinetics of metal dusting.* Materials and corrosion, 1998. **49**(5): pp. 303-308.

17. J.N. Paz. and H.J. Grabke, *Metal dusting.* Oxidation of metals, 1993. **39**(5-6): pp. 437-456.
18. G.A. Slabbert, F.M.L. Mulaudzi, L.A. Cornish, M.J. Papo, V. Morudu and J. Zhang, *The effect of the matrix structure on the metal dusting rate in hydrocarbon environments.* Journal of the Southern African Institute of Mining and Metallurgy, 2013. **113**(2): pp. 81-90.
19. J. Zhang and D.J. Young, *Kinetics and mechanisms of nickel metal dusting I. Kinetics and morphology.* Corrosion Science, 2007. **49**(3): pp. 1496-1512.
20. H.J. Grabke, *Carburization, carbide formation, metal dusting, coking.* Materiali in Tehnologije, 2002. **36**(6): pp. 297-306.
21. H.J. Grabke, *Metal dusting.* Materials and corrosion, 2003. **54**(10): pp. 736-746.
22. H.J.Grabke, *Corrosion by carbonaceous gases, carburization and metal dusting, and methods of prevention.* Materials at high temperatures, 2000. **17**(4): pp. 483-487.
23. Z. Zeng. and K. Natesan, *Relationship of carbon crystallization to the metal-dusting mechanism of nickel.* Chemistry of materials, 2003. **15**(4): pp. 872-878.
24. R. Yang and J. Chen, *Mechanism of carbon filament growth on metal catalysts.* Journal of Catalysis, 1989. **115**(1): pp. 52-64.
25. H.J. Grabke, *Nickel-based alloys in carbonaceous gases.* Corrosion, 2000. **56**(8): pp. 801-808.
26. J. Zhang, P. Munroe, and D.J. Young, *Microprocesses in nickel accompanying metal dusting.* Acta Materialia, 2008. **56**(1): p. 68-77.
27. D.J.Young and J. Zhang, *Metal dusting: Catastrophic corrosion by carbon.* JOM, 2012. **64**(12): pp. 1461-1469.
28. R. Al-Jishi, and G. Dresselhaus, *Lattice-dynamical model for graphite.* Physical review B, 1982. **26**(8): pp. 4514.
29. R.J.Nemanich and S. Solin, *First-and second-order Raman scattering from finite-size crystals of graphite.* Physical review B, 1979. **20**(2): pp. 392.
30. F. Tuinstra and J.L. Koenig, *Raman spectrum of graphite.* The Journal of Chemical Physics, 1970. **53**(3): pp. 1126-1130.
31. A.C. Ferrari and J. Robertson, *Interpretation of Raman spectra of disordered and amorphous carbon.* Physical review B, 2000. **61**(20): pp. 14095.
32. R.S. Wagner and W.C. Ellis, *VAPOR-LIQUID-SOLID MECHANISM OF SINGLE CRYSTAL GROWTH.* Applied Physics Letters, 1964. **4**(5): pp. 89-90.
33. R. Baker, M. Barber, P. Harris, F. Feates and R. Waite, *Nucleation and growth of carbon deposits from the nickel catalyzed decomposition of acetylene.* Journal of Catalysis, 1972. **26**(1): pp. 51-62.
34. R. Baker, P. Harris, R. Thomas, and R. Waite *Formation of filamentous carbon from iron, cobalt and chromium catalyzed decomposition of acetylene.* Journal of Catalysis, 1973. **30**(1): pp. 86-95.
35. J. Zhang, D. Cole, and D. Young, *Alloying with copper to reduce metal dusting of nickel.* Materials and corrosion, 2005. **56**(11): pp. 756-764.

6 GENERAL CONCLUSIONS & RECOMMENDATIONS

6.1. General Conclusions

Firstly, MD was proven to have taken place on a polished highly corrosion resistant alloy, Hastelloy C276. Initial studies to remove any ambiguity in this study using gaseous helium and laboratory air at 800 °C showed the formation of grain boundaries after 1 h of reaction. Within the grain boundaries, a high presence of Cr was observed as compared to the surface of the Hastelloy. This observation was in line with the phenomena known as intergranular attack (IGA) which leads on to intergranular corrosion (IGC). When the Hastelloy block was exposed to vaporised toluene with helium as carrier gas pits had occurred on the surface after the removal of carbonaceous material with laboratory air. These pits were formed as a consequence of MD using vaporised toluene at 800 °C, since conclusive evidence was provided that these pits were not caused by laboratory air or helium gas.

In Chapter 5, all Hastelloy C276 blocks used were in its unpolished form (as opposed to Chapter 4), since it was discovered that unpolished Hastelloy blocks synthesized carbon nanofilaments that were more complete and much higher in yield. The carbon nanofilaments synthesized were an ensemble of CNFs and CNTs which varied in diameter according to different reaction times and flow rates studied. The carburisation rates followed an exponential decay trend, but showed a deviation amongst the different flow rates studied. In addition the carburisation rate followed a second order rate law. The activation energy (E_a) calculated for the vaporised toluene to react with the Hastelloy showed good comparison with the values reported in literature.

PXRD showed an increase in 2Θ values when exposed to MD conditions. The shift was due to compressive stresses which are generally caused by MD. Grazing angle XRD used to analyse the surface of Hastelloy C276 where carbonaceous material was formed as bulk analysis PXRD could barely or not detect a graphitic peak. Laser Raman spectroscopy had shown the relevant D and G peaks associated with carbon nanomaterials, more specifically carbon nanofilaments.

Other carbonaceous material, known as GPSs, was formed in the pits of the unpolished Hastelloy C276 blocks, but were reported in literature not to be a cause of the MD mechanism. On the whole, carbon nanofilaments were formed on the rough surfaces of an unpolished Hastelloy C276 block, whereas GPSs were formed in the pits.

With everything taken in to consideration OM, SEM, EPMA, TEM, laser Raman spectroscopy and PXRD have assisted in understanding the effect of MD on Hastelloy C276 using a liquid hydrocarbon source, toluene. The use of toluene has shown that MD does take place on the surface of Hastelloy C276 and equivalent carbon products such as CNFs and CNTs were synthesised which were observed in those MD conditions taking place in syngas mixtures. Moreover, studying the mechanistic details using the characterisation techniques mentioned yielded many similarities between the data reported in this dissertation and data reported in literature from reactions taking place in syngas. This was of importance since the mechanism of MD in charge heater tubes i.e. MD due to naphtha (a similar carbon source to that which was researched in this project) has been insufficiently explained.

6.2. Recommendations

The following are recommendations based upon lessons learned in this study:

- The synthesis of CNTs/CNFs may be up-scaled by using a Hastelloy C276 reactor in place of a quartz tube reactor for mass production. The reactor would replace the quartz tube providing a higher surface area for CNTs/CNFs to form compared to a single Hastelloy C276 block.

- Various other alloys instead of commonly used stainless steel in literature and Hastelloy C276 used for this study may be investigated to synthesize carbon nanomaterials with different morphologies or CNFs/CNTs with different characteristics. Changing the alloy may also synthesize CNTs or CNFs selectively.

- The carbon source may be changed to other liquid hydrocarbons, also to presumably synthesize carbon nanomaterials with different morphologies or CNTs/CNFs with different characteristics. This may also assist in synthesizing CNTs or CNFs individually.

- Determination of the E_a of different alloys and carbon sources could be performed for two reasons: (1) Industrial purposes were MD corrosion is likely to occur, a variety of alloys can be tested with the carbon source where the E_a will give an indication as to the best alloy to use in the carbon environment and (2) Acquire the best alloys and carbon sources to synthesize carbon nanomaterials.

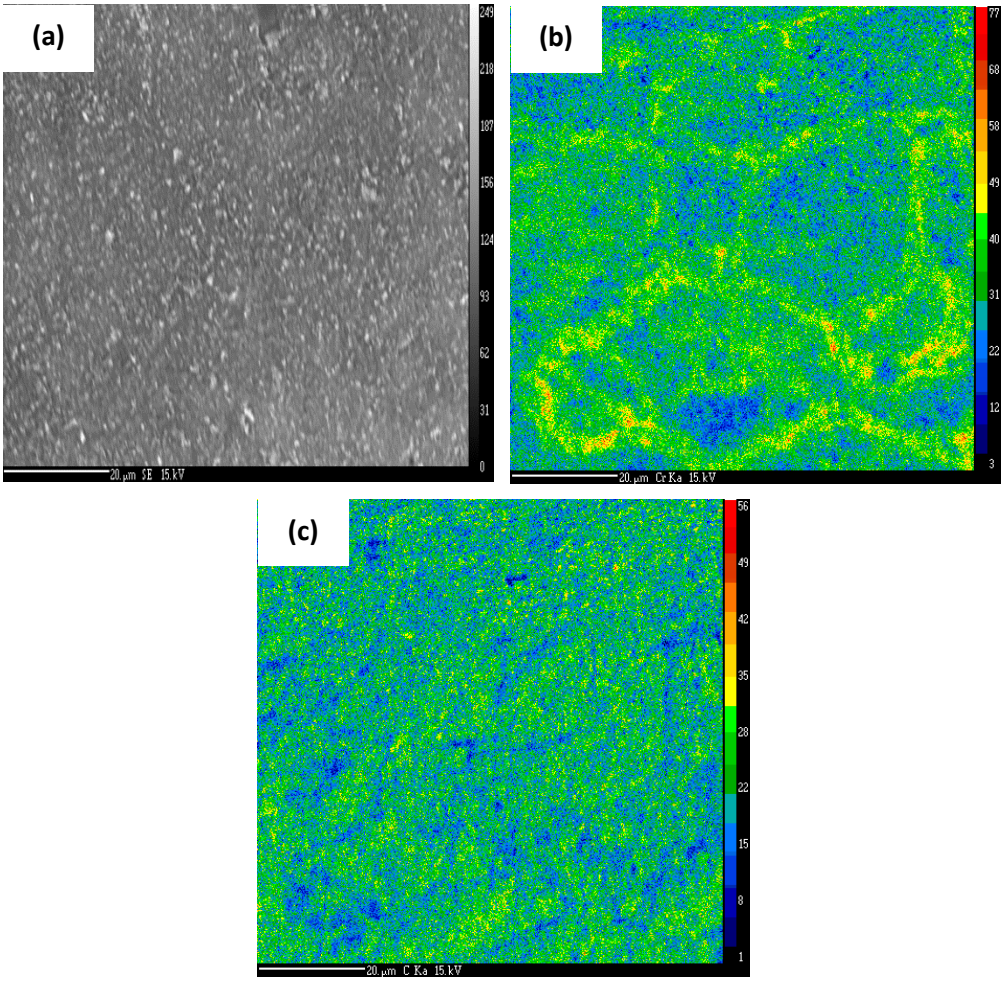
- Provide a variety of coated Hastelloy C276 blocks for study (e.g. silica coated Hastelloy C276 blocks via the cold spray technique) with a view to testing which coating best prevents MD corrosion.

- Modify the surfaces of alloys with acids and/or bases to entice the growth of other carbon morphologies. This has been done as a preliminary study where carbon spheres were formed.

APPENDICES

Appendix 1

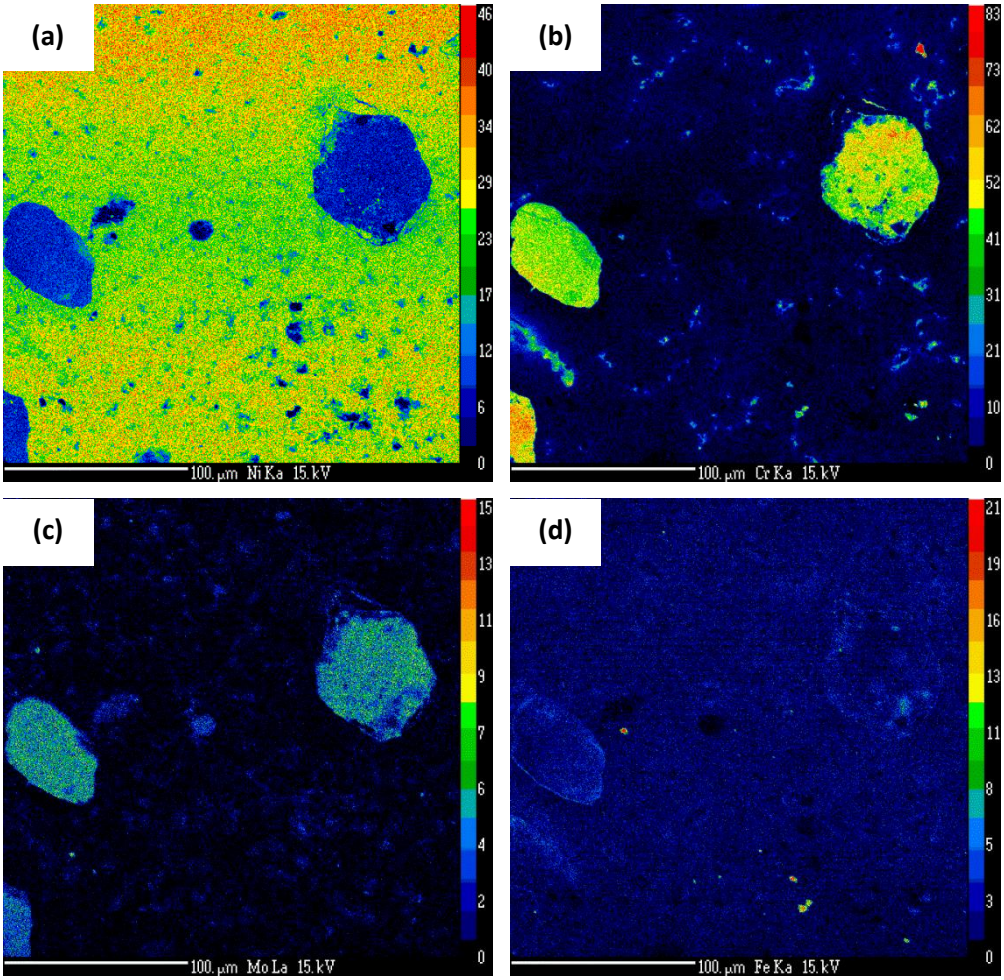
Supplementary images for Figure 4.9(c) and (f), showing that carbon growth was limited in the grain boundaries where Cr was abundant. EPMA was done at higher magnification for better clarity as compared to Figure 4.9(f).



A1.1. Elemental maps of a polished Hastelloy C276 surface exposed to MD conditions at higher magnification showing: **(a)** SEM image of the mapped area, **(b)** Cr K_α and **(c)** C K_α.

Appendix 2

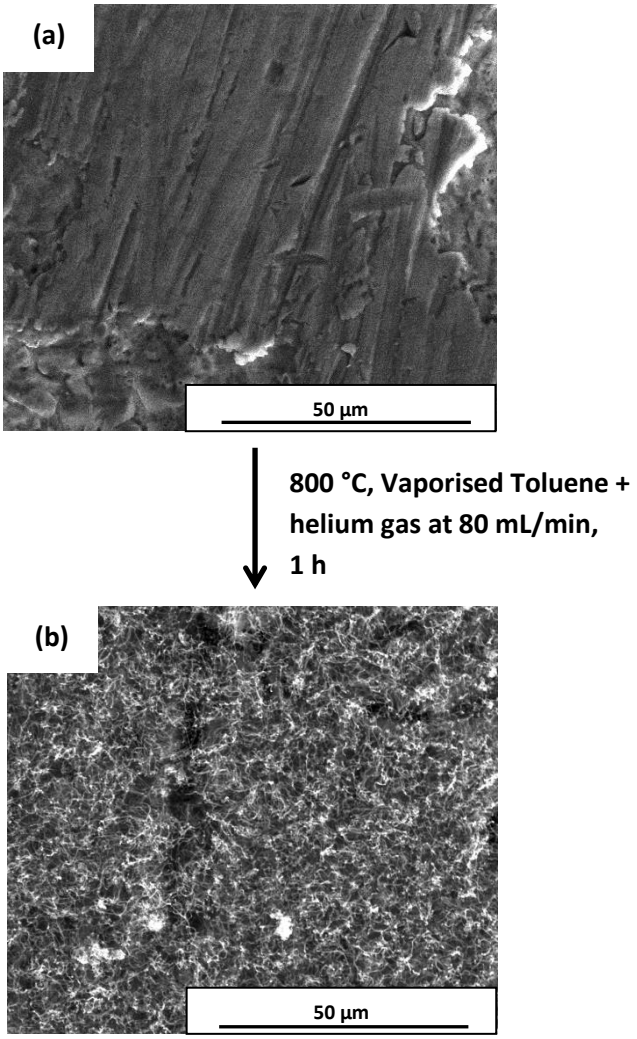
Extension of Figure 4.13, showing Ni K_α, Cr K_α, Mo L_α and Fe K_α.



A2.1. Extension of elemental maps of a polished Hastelloy C276 surface exposed to MD conditions after carbon had been burnt off from *Figure 4.13*, showing: **(a)** Ni K_α, **(b)** Cr K_α, **(c)** Mo L_α and **(d)** Fe K_α.

Appendix 3

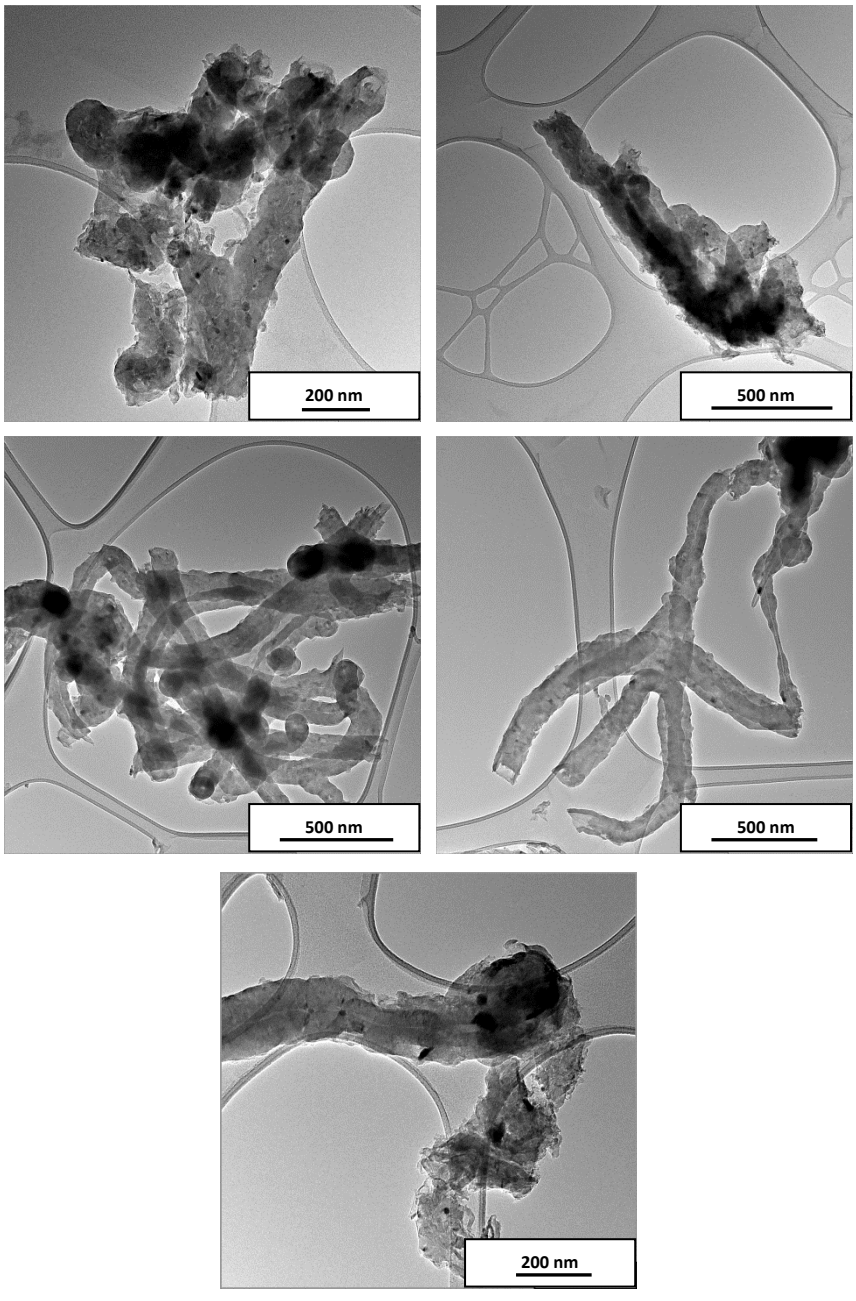
Carbon nanofilaments synthesized on an unpolished (rough surface) Hastelloy C276 sample when exposed to vaporised toluene and helium gas at 800 °C for 1 h. The quantity of carbon nanofilaments synthesized was plentiful as compared when synthesized to a polished (smooth) Hastelloy C276 surface.



A3.1. SEM image showing: **(a)** A rough Hastelloy C276 surface and **(b)** A high yield of carbon nanofilaments that formed when synthesized on an unpolished surface of Hastelloy C276 and exposed to reaction conditions.

Appendix 4

TEM images of poorly formed carbon nanofilaments synthesized at 10 and 15 min.

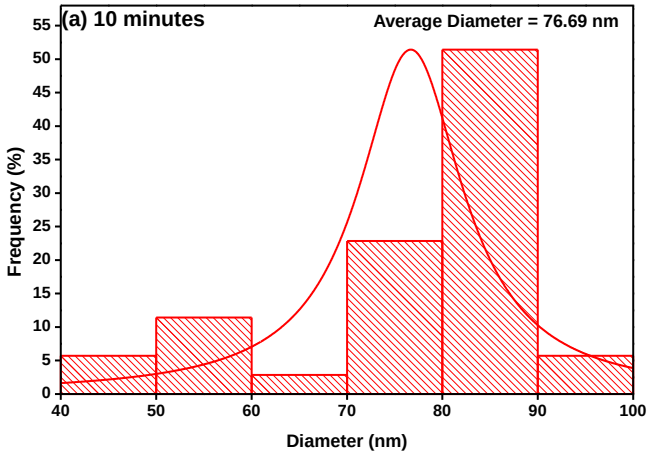


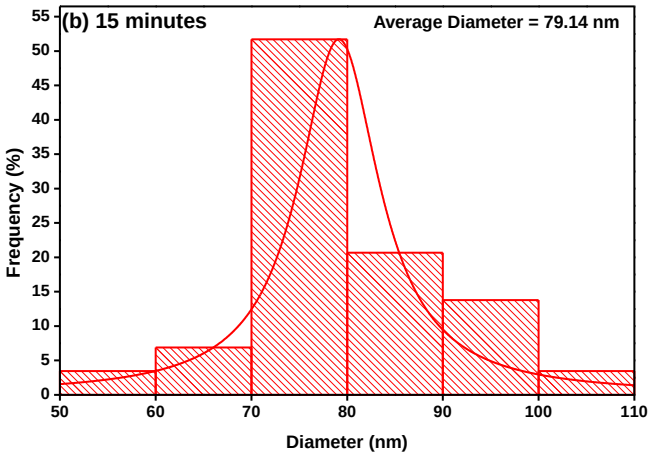
A4.1. TEM images showing carbon nanofilaments that were poorly formed.

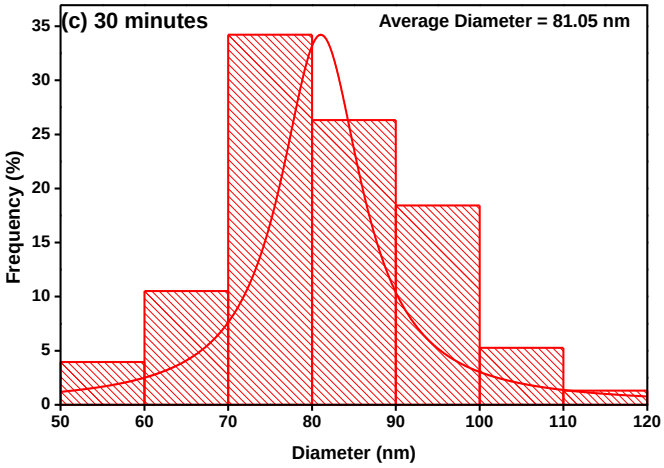
Appendix 5

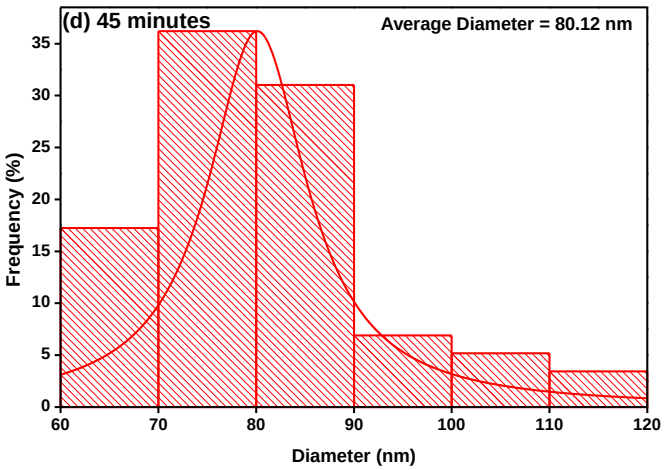
Histogram plots of average filament diameters shown in Table 5.1 after measuring 300 filaments.

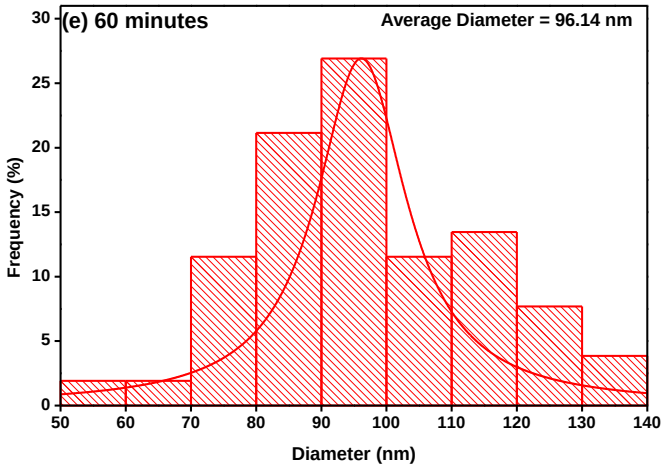
A5.1. 80 mL/min for the various times shown

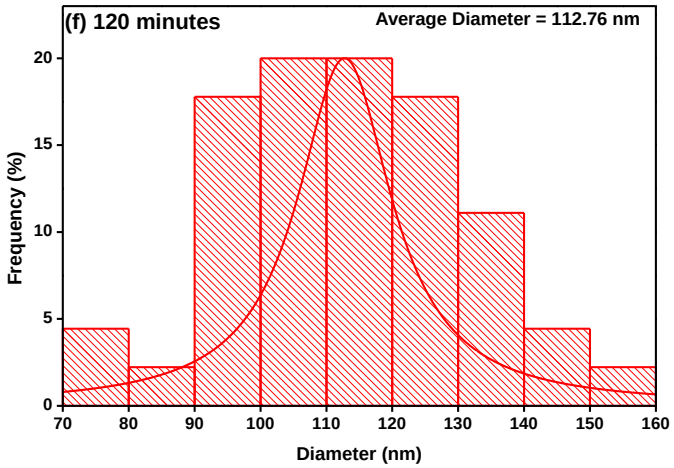


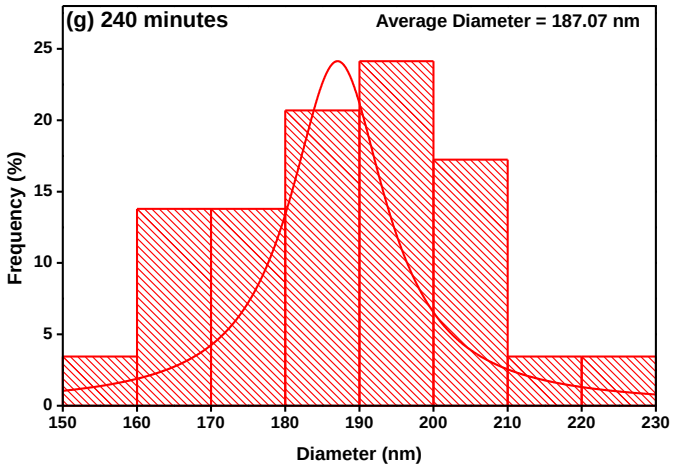



(c) 30 minutes
Average Diameter = 81.05 nm
Frequency (%)
Diameter (nm)
0
5
10
15
20
25
30
35
50
60
70
80
90
100
110
120

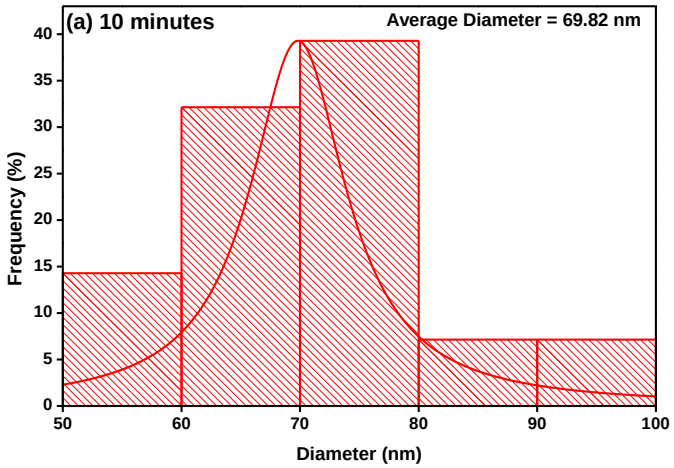

(d) 45 minutes
Average Diameter = 80.12 nm
Frequency (%)
Diameter (nm)
0
5
10
15
20
25
30
35
60
70
80
90
100
110
120

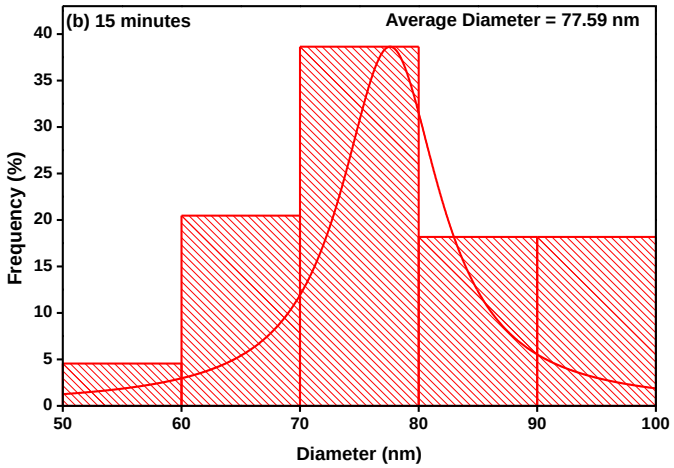

(e) 60 minutes
Average Diameter = 96.14 nm
Frequency (%)
Diameter (nm)
0
5
10
15
20
25
30
50
60
70
80
90
100
110
120
130
140

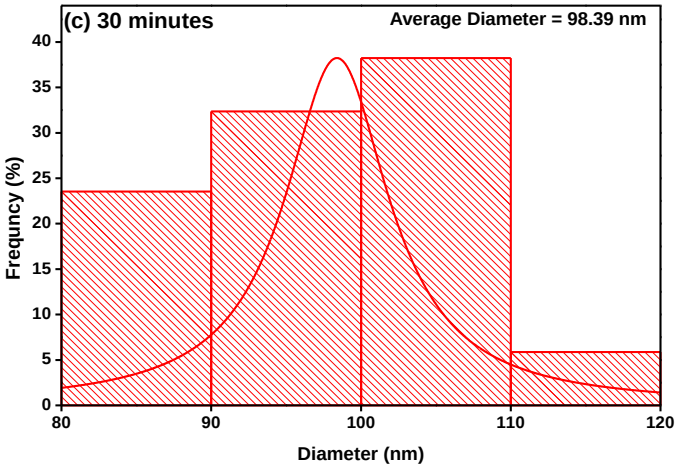

(f) 120 minutes
Average Diameter = 112.76 nm
Frequency (%)
Diameter (nm)
0
5
10
15
20
70
80
90
100
110
120
130
140
150
160

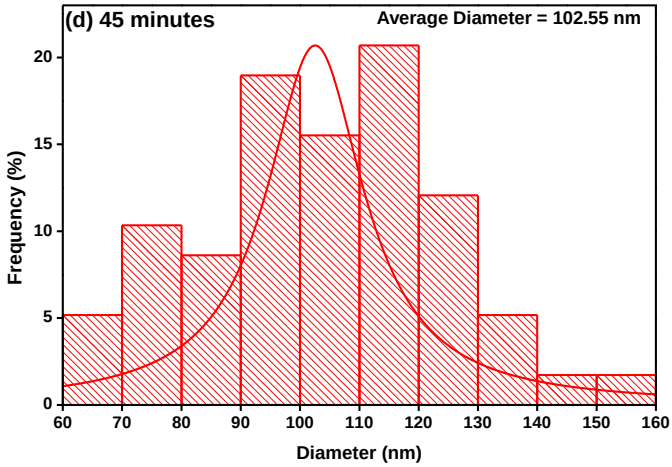

(g) 240 minutes
Average Diameter = 187.07 nm
Frequency (%)
Diameter (nm)
0
5
10
15
20
25
150
160
170
180
190
200
210
220
230

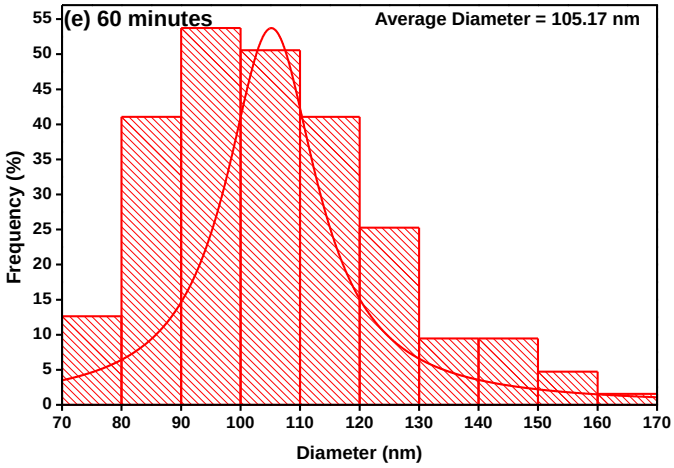
A5.2. 160 mL/min for the various times shown

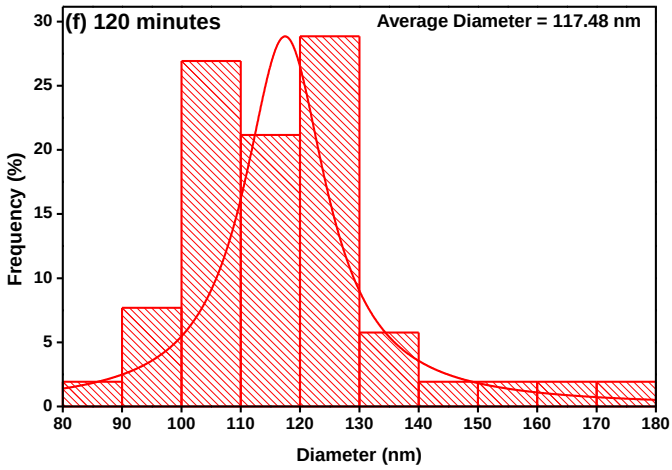


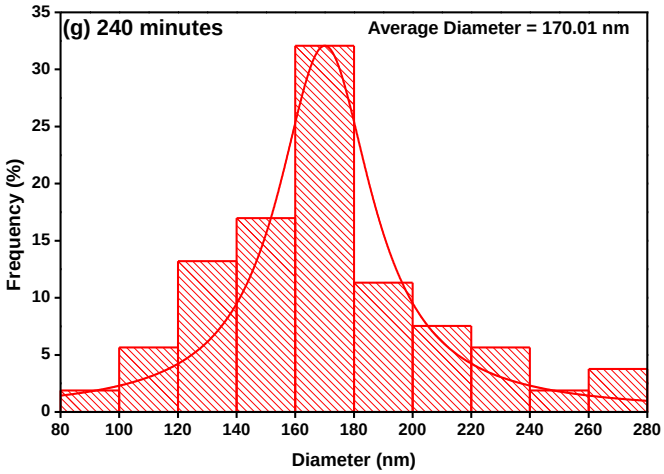




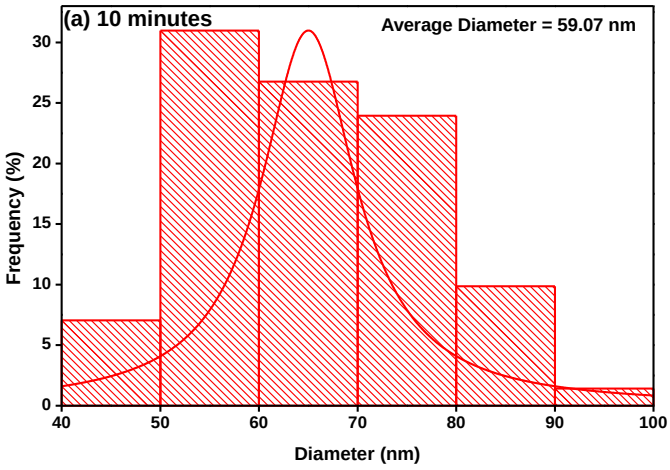

(d) 45 minutes
Average Diameter = 102.55 nm
Frequency (%)
Diameter (nm)

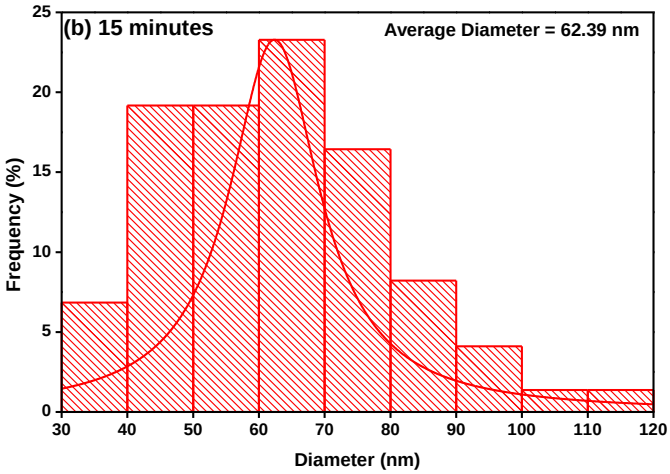

(e) 60 minutes
Average Diameter = 105.17 nm
Frequency (%)
Diameter (nm)

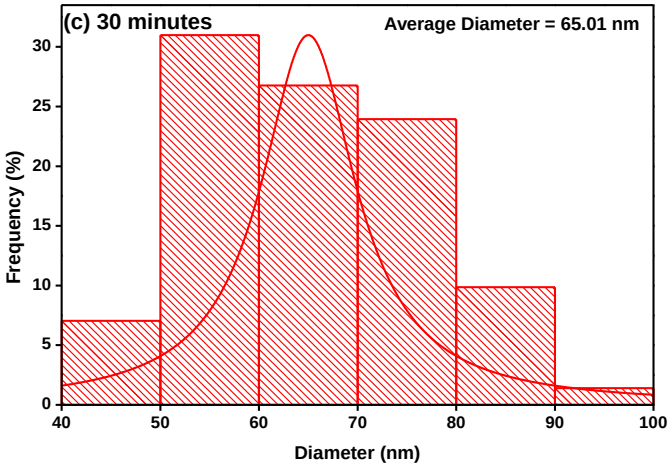

(f) 120 minutes
Average Diameter = 117.48 nm
Frequency (%)
Diameter (nm)

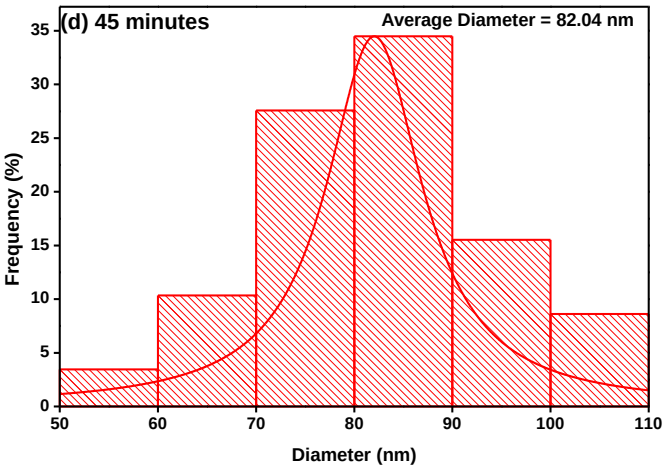


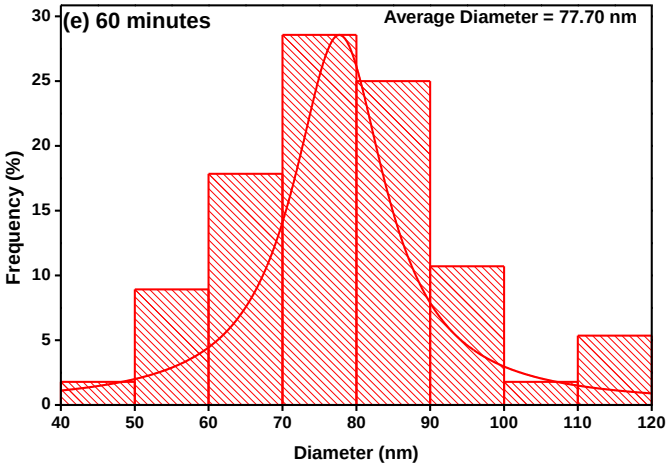
A5.3. 240 mL/min for the various times shown

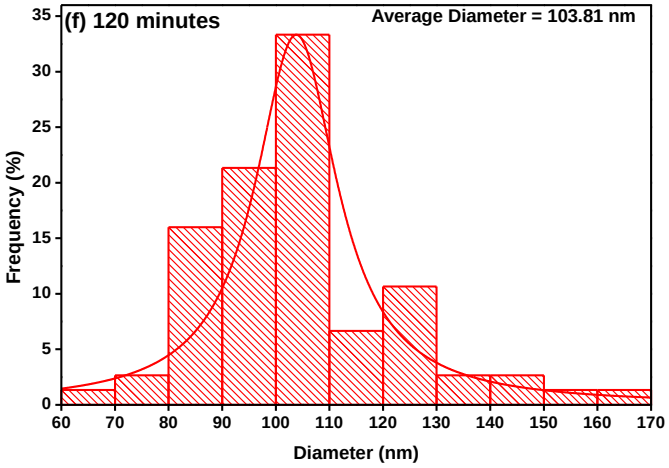


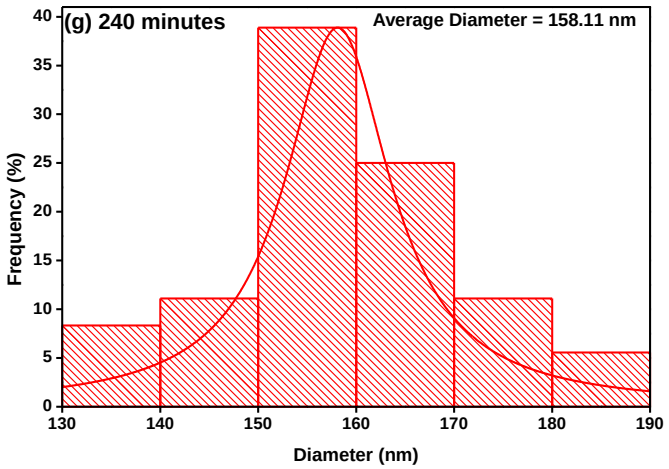

(b) 15 minutes
Average Diameter = 62.39 nm
Frequency (%)
Diameter (nm)
0
5
10
15
20
25
30
40
50
60
70
80
90
100
110
120


(c) 30 minutes
Average Diameter = 65.01 nm
Frequency (%)
Diameter (nm)
0
5
10
15
20
25
30
40
50
60
70
80
90
100


(d) 45 minutes
Average Diameter = 82.04 nm
Frequency (%)
Diameter (nm)
0
5
10
15
20
25
30
35
50
60
70
80
90
100
110

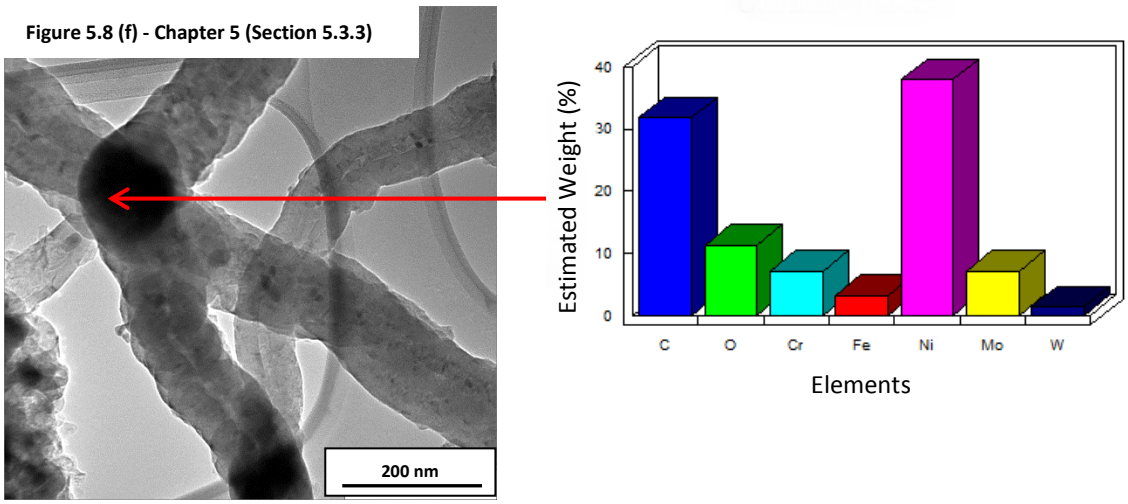

(e) 60 minutes
Average Diameter = 77.70 nm
Frequency (%)
Diameter (nm)
0
5
10
15
20
25
30
40
50
60
70
80
90
100
110
120


(f) 120 minutes
Average Diameter = 103.81 nm
Frequency (%)
Diameter (nm)
0
5
10
15
20
25
30
35
60
70
80
90
100
110
120
130
140
150
160
170


(g) 240 minutes
Average Diameter = 158.11 nm
Frequency (%)
Diameter (nm)
0
5
10
15
20
25
30
35
40
130
140
150
160
170
180
190

Appendix 6

TEM-EDS (energy dispersive X-ray spectroscopy) for the TEM image shown in Figure 5.8(f) proving that a metal particle was in between the two carbon nanofilaments. The EDS data showed that Ni was the main element present.



A6.1. TEM-EDS for metal particle between carbon nanofilaments in *Figure 5.8*.

Appendix 7

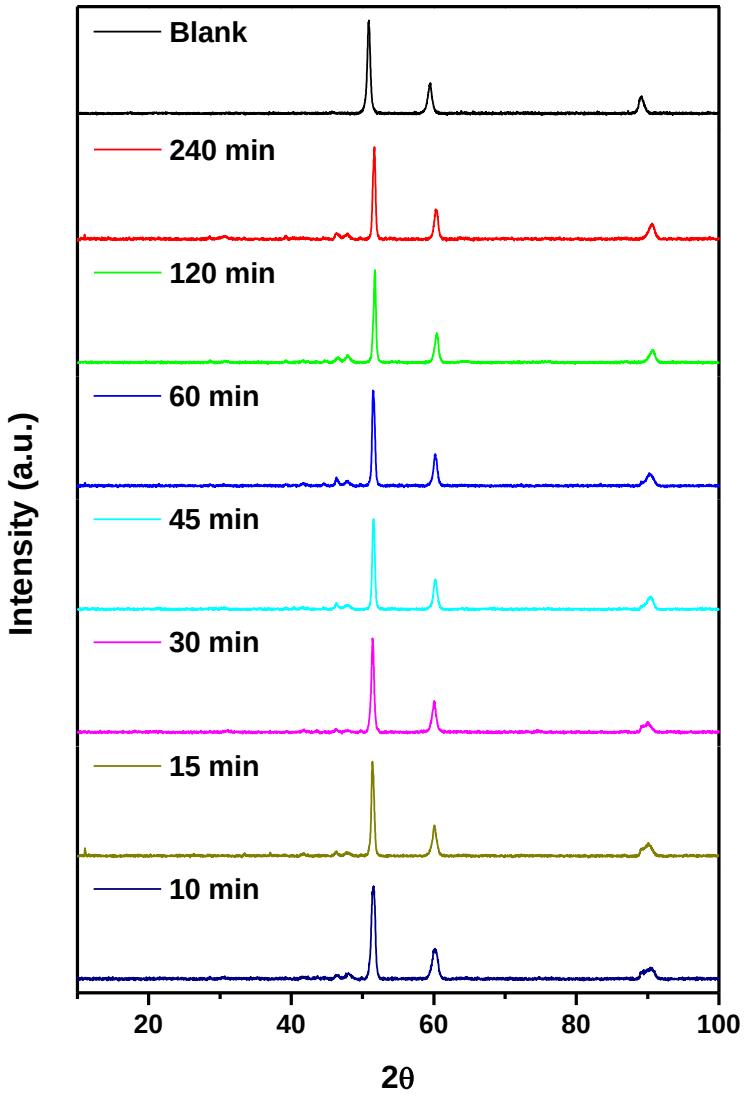
A7.1. E_a at different temperature ranges (700 – 900 °C)

Temperature $_1$ (°C)	Temperature $_2$ (°C)	E_a (kJ/mol)
700	750	67.13
700	800	79.63
700	850	69.71
700	900	63.59
750	800	93.41
750	850	71.20
750	900	62.17
800	850	46.82
800	900	44.26
850	900	41.46

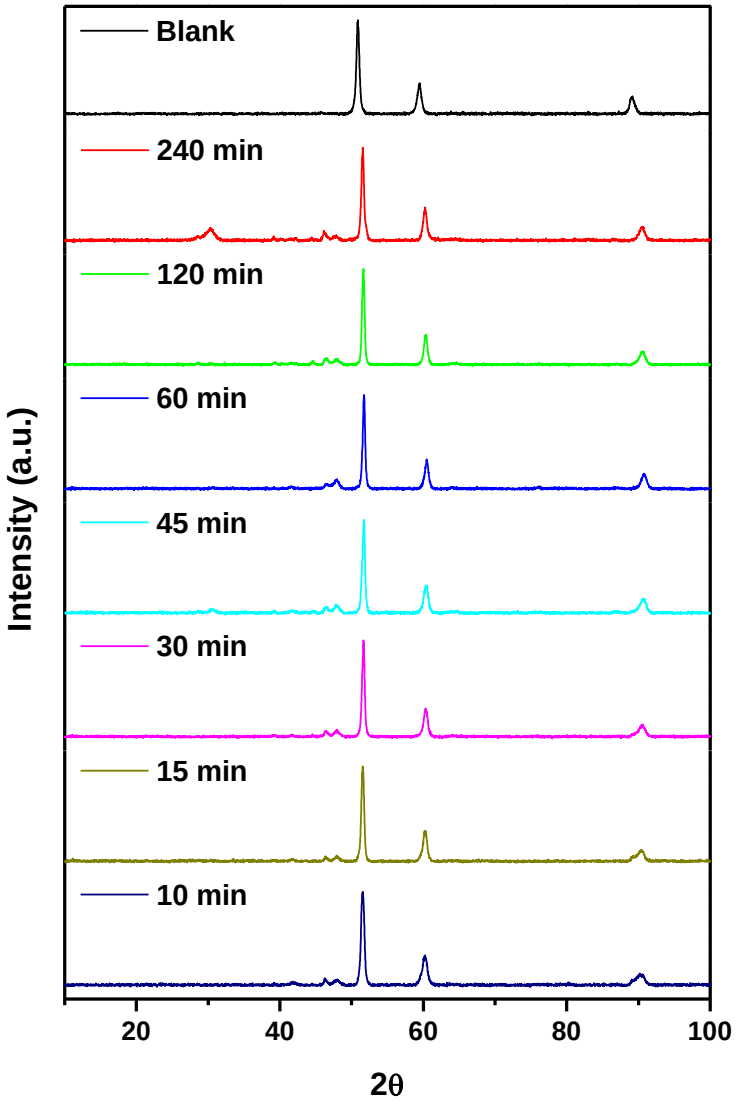
Table A7.1. shows E_a data for reaction temperatures ranging between 700 – 900 °C as compared to 800 – 900 °C (shown in Chapter 5). As mentioned in Chapter 5, the inconsistency of the E_a values below 800 °C was relatively high. Taking the data represented in Table A7.1., the E_a was determined to be 63.94±16.33 kJ/mol. Compared to a standard deviation of 2.68 reported in Chapter 5, a standard deviation of 16.33 shown here was relatively high.

Appendix 8

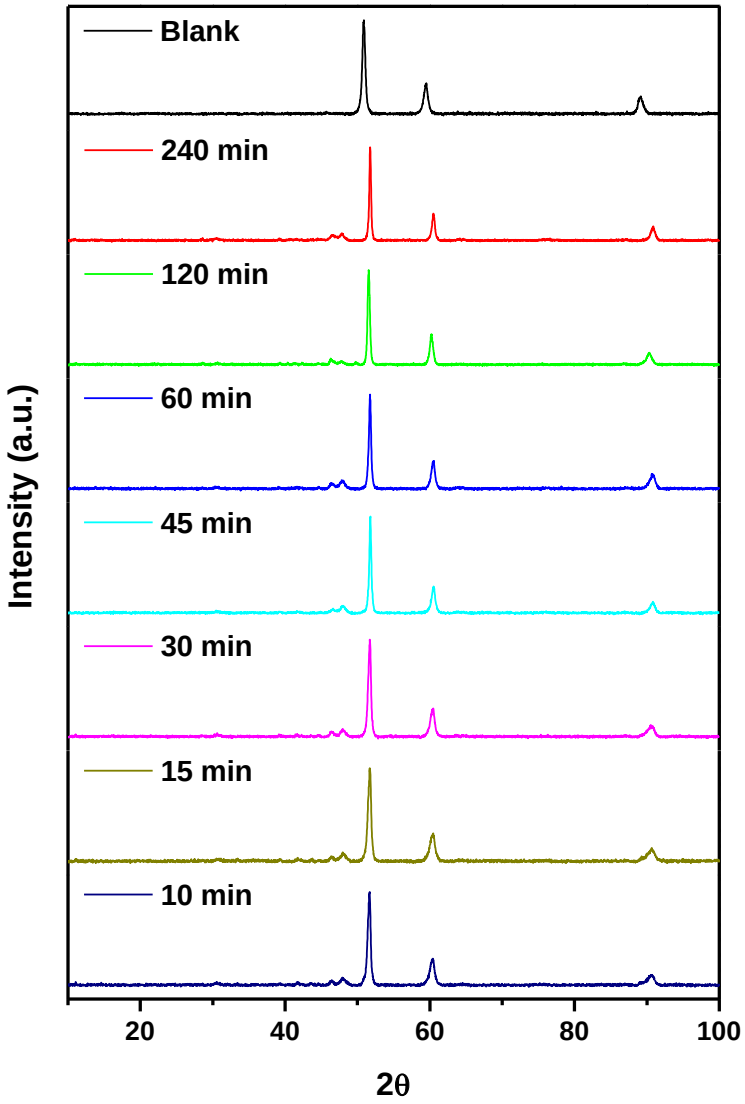
Appendix 8 shows the PXRD patterns for the entire range of reaction times at flow rates of 80, 160 and 240 mL/min including reaction times shown in Chapter 5. The clarity of the PXRD patterns shown in A8.1, 8.2 and 8.3 was compromised due to the high volumes of data compared to Figures 5.13, 5.14 and 5.15 where better resolution was observed.



A8.1. PXRD patterns of Hastelloy C276 exposed to MD conditions at 80 mL/min of reaction times ranging from 10 – 240 minutes.



A8.2. PXRD patterns of Hastelloy C276 exposed to MD conditions at 160 mL/min of reaction times ranging from 10 – 240 minutes.



A8.3. PXRD patterns of Hastelloy C276 exposed to MD conditions at 240 mL/min of reaction times ranging from 10 – 240 minutes.